Doctoral Thesis

Effective Utilization of Functional Groups on Micropore Walls for Designing Materials with Enhanced Performances in Catalysis and Sorption

Yuan Huang

Division of Environmental Materials Science
Graduate School of Environmental Science
Hokkaido University

Table of Contents

Chapter 1

General Introduction

1. Backgrounds

Solid materials have been used as tools in human life for millions of years. The firstly used materials were natural materials such as wood, stones, animal bones etc., some of which are porous materials. Porous materials are solid materials that contain voids, channels, or pores. They can be found almost everywhere surrounding us. Sea sponges, coral reef, eggshells and even snowflakes are naturally occurring porous materials around us. We have been living with these materials for such a long time and being so familiar with them that we might forget or ignore their existence, while they could have greatly changed our life. For example, ice cream is a popular dairy product, especially in summer. Since ice creams are served at low temperatures, aroma cannot be fully perceived by the sense of smell, and one must rely more on taste. The taste experience of ice cream is created not only by adjusting the ingredients, such as milk, but also by incorporating air as an ingredient, i.e., pores that give the smooth texture of ice cream. Similar but not limited to this function, the pores in solid materials play important roles, rendering porous materials for widespread uses and act as one of the largest contributions to modern society. New classes of functional porous materials have been produced with the aid of advances in synthesis to achieve more desired functions.[1] However, it remains challenging to choose the right type of porous material for a specific task, as there are so many kinds of porous materials and there is no one-size-fits-all solution.

2. Classification of porous materials

The characteristics of a porous material vary depending on factors such as the size, shape and arrangement of the pores, as well as the composition of the material itself. Porous materials can be classified according to their characteristics, although each class could be diverse. A general attempt at classification of porous materials is summarized in **Figure 1-1**, with several well-known porous materials shown as examples in each class.

Pore size is frequently used as a primary parameter for classifying porous materials.[2] Typically, according to the nomenclature recommended by the International Union of Pure and Applied Chemistry (IUPAC), it is expedient to classify pores according to their size: micropores [<2 nm, including ultramicropores (<0.7 nm) and supermicropores (0.7-2 nm)], mesopores (2-50 nm) and macropores (>50 nm).[3,4] Accordingly, porous materials containing pores with such sizes are classified into microporous, mesoporous and macroporous materials, respectively. Zeolites serve as a typical example of microporous materials, with most possessing pore sizes ranging from 0.3 to 1.0 nm, although zeolites with extra-large-pore (exceeding 1.0 nm) like VPI-5,[5,6] ITQ-

21,[7] ZEO[8–10] etc., have also been reported. Mesoporous materials, such as mesoporous silica,[11–13] exhibit a wide range of pore sizes, typically falling between 2 and 50 nm. Macroporous materials commonly consist of macroporous carbon[14] and metal oxide[15]. Additionally, it is noteworthy that certain porous materials like activated carbon and metal-organic frameworks (MOFs) can encompass a wide range of pore sizes, including micro-, meso-, and even macropores. Likewise, it is also noteworthy that the pore size of a certain group of porous materials may change with advances in synthesis. For instance, conventional zeolites serve as microporous materials, while recently the introduction of mesopores into zeolites have been extensively explored, and plenty of research on synthesis of mesoporous zeolites have been reported.[16–18]

Based on the long-range order, porous materials can be classified as amorphous and crystalline porous materials.[1] Crystalline porous materials include zeolites,[19,20] MOFs,[21] covalent organic frameworks (COFs),[22,23] and H-bonded organic frameworks (HOFs),[24,25] whereas most porous organic polymers, such as polymers of intrinsic microporosity (PIMs),[26] conjugated microporous polymers (CMPs),[27] and hypercrosslinked porous polymers (HCPs),[28] belong to the amorphous category. Due to the difference in structural arrangement, amorphous and crystalline porous materials exhibit contrasting properties. Crystalline porous materials exhibit precise and narrow pore size distributions, allowing for the prediction and design of their structures due to the ordered arrangement of building units. Conversely, predicting the structural arrangement of amorphous porous materials is challenging. Amorphous porous materials typically feature interconnected pores with a wide range of pore sizes, resulting in a broad pore size distribution, which can enable facile mass transport across the interconnected pores.

Porous materials can also be classified into three categories based on their chemical composition of building blocks: inorganic, inorganic-organic hybrid, and organic porous materials.[29] Zeolites and porous metal oxides are typical examples for inorganic porous materials. Inorganic-organic hybrid porous materials are represented by coordination polymers, including MOFs, which combine both inorganic and organic components in their building blocks. Organic porous materials encompass diverse range of members, including the aforementioned HCPs, PIMs, COFs, HOFs and so on.

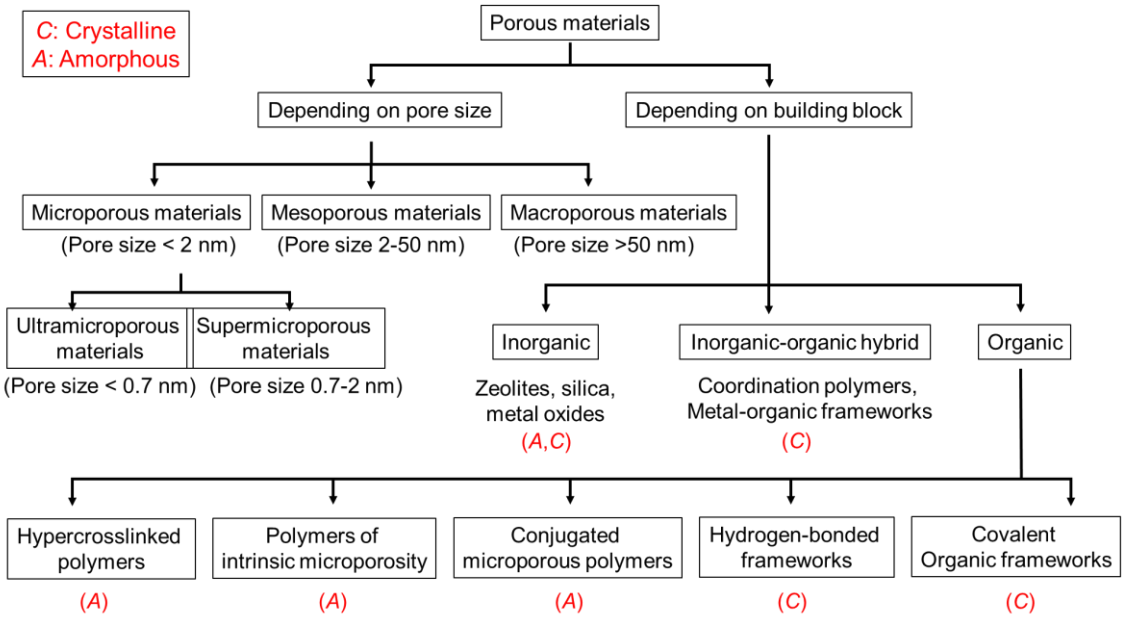

Figure 1-1. General classification of porous materials based on pore sizes, degree of long-range order and building blocks.

3. Applications of porous materials

Porous materials are of great interest in modern scientific and technological filed due to their fascinating properties, including high surface area, large accessible space, and variable chemical composition. These characteristics make them promising materials for a large variety of applications in gas adsorption and separation, catalysis, and biotechnology. Several typical applications of porous materials are depicted in **Figure 1-2**.

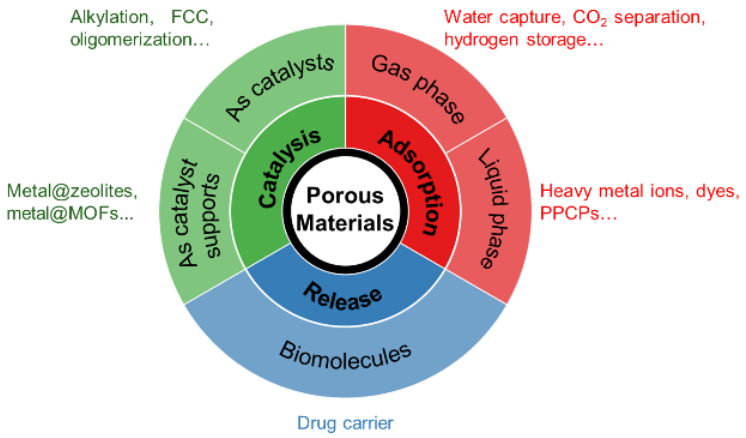

Figure 1-2. Schematical figure showing typical applications of porous materials.

3.1 Adsorption and separation

One primary application for porous materials lies in their utilization as adsorbents in both liquid and gas phases.

3.1.1 Adsorption in liquid phase

Porous materials have been extensively applied as adsorbents for the adsorption of toxic substances from water sources.[30–33] The main adsorption mechanisms employed by porous materials for the removal of contaminants from water include surface adsorption, chelation, ion exchange, and electrostatic interaction. For example, the presence of aluminum in zeolite gives a negative charge to the framework, which is in turn compensated by an extra-framework cationic species. This property allows zeolites to function effectively as adsorbents for the removal of heavy metal ions.[34–36] The adsorptive removal of biologically active molecules like pharmaceuticals and personal care products (PPCPs) from water is another important application of porous materials. Numerous studies on the removal of drug molecules in aqueous media have been conducted using Fe-based MOFs. In most cases, the adsorption of these molecules occurs on the metal centers of the second building units of MOFs. Surface modification on the open metal sites serves as a useful approach for modifying the adsorption behavior in these systems.[37,38]

3.1.2 Adsorption in gas phase

There are also countless examples of employing porous materials as adsorbents for gas adsorption and separation.[39–41] An important characteristic involved in application of porous materials for adsorption and separation is the size effect, also known as molecular sieve effect, which is observed in porous materials with the pore size comparable to the size of target molecules. Typically, a porous material selectively adsorbs small molecules from a mixture containing other molecules that the sizes of them are too large to enter the pores. For example, K^+-A with pore diameter of 0.3 nm can adsorb water molecules while is not able to adsorb molecules larger than 0.3 nm, thus it is often used to remove water from ethanol.[42] The molecular sieve can also distinguish even very small differences in molecular size. The separation of alkenes from alkanes has been a huge task since the conventional separation process of cryogenic distillation is an energy-intensive process, due to the similar sizes and boiling points of alkenes and alkanes. Extensive research has been carried out on porous materials to separate propylene from propane in an energy-saving way.[43–45]

In addition to pore size, gas separation is also influenced by interaction affinity, especially at low temperatures, the affinity of the gas molecule to the surface is much more important than

the size. Higher affinity can be expected by tuning the nature of the adsorbents.[46] CO_2 capture serves as a typical example. Two important CO_2 separation process are CO_2 capture from flue-gas and natural-gas purification. The former one often entails separating CO_2 from post-combustion flue gas, which mainly consists of N_2 and CO_2. In the latter one, CO_2 is an impurity in natural gas, the capture of CO_2 from CH_4 improves CH_4 purity and reduces pipeline corrosion by the acidic CO_2 gas.[47] MOFs have attracted a growing interest in CO_2 capture owing to their modular and highly tunable nature. Introduction of open metal sites is beneficial for achieving higher affinity. Two prominent examples for MOFs where the formation of open metal sites leads to outstanding performance in CO_2 adsorption are MOF-74(Mg)[48] and HKUST-1(Cu)[49].

3.2 Catalysis

Owing to their high surface area, tuned pore sizes, and multivarious chemical compositions, porous materials provide versatile platforms for catalytic applications. In heterogeneous catalysis, they are used as catalysts or as catalyst supports.

3.2.1 As catalysts

Indeed, as the simplest approach, porous materials themselves can serve as heterogeneous catalysts. The characteristics utilized for heterogeneous catalysis typically involve their intrinsically active acid (or/and base) sites and molecular sieve effect.

The catalytic versatility of zeolites makes them one of the most important classes of heterogeneous catalysts in industrial applications, especially for petrochemical cracking and isomerization reactions. In zeolite, framework Al is tetrahedrally coordinated with four -O-Si bonds thus the presence of Al-O-Al motifs are prohibited.[50] The presence of Al gives a negative charge to the framework, which is in turn compensated by an extra-framework cationic species. When this cation is a proton, a hydroxyl group bridging Al and Si forms, which can serve as a Brønsted acid site. Introducing heteroatoms such as Ti, Sn or Zr into the framework can further generate Lewis acid sites. Lewis acidic Al sites can also be generated through several synthetic routes like steaming and high-temperature calcination.

In heterogeneous catalysis over zeolites, the molecular sieve effect reflects on three aspects: (1) Reactant selectivity occurs when only part of the reactant molecules that are small enough to diffuse through the pores to the active sites. (2) Restricted transition-state selectivity occurs when part of reaction does not proceed if the corresponding transition state exceeds the size of cavities. This roughly explains why some reactions do not proceed. (3) Product selectivity occurs when part of the product formed inside the pores are too large to diffuse out as observed products.[51]

An ultra stable Y (USY) zeolite has been applied as the catalyst for fluid catalytic cracking (FCC) to convert the high boiling hydrocarbon fractions of crude oils into valuable fuels.[52] The cracking of alkanes is Brønsted-acid catalyzed, which can proceed over H^+-type USY. The USY zeolite plays another important role in FCC that shows reactant shape selectivity. USY zeolite has pore opening that the branched alkanes can not enter, so the unbranched alkanes are preferentially cracked in the FCC process.[53]

MOFs constructed by the bonding between metal containing units and organic linkers also serves as porous solids with intrinsic catalytic activity. To date, three approaches have been proposed to achieve intrinsic catalytic activity for MOFs: (1) by using the organic linker, (2) by introducing open metal sites, and (3) by the creation of defects.[54,55] The sulfonic acid group (-SO_3H) was grafted onto MIL-101(Cr) by using organic linker of 2-sulfoterephathalate in the presence of HCl, where -SO_3H group acted as strong Brønsted acid site and the functionalized MOF showed high catalytic activity for cellulose hydrolysis.[56] Lewis acid open Cu sites is readily available for HKUST-1(Cu) upon the removal of coordinated water molecules by heating, facilitating Lewis acidic activity in the cyanosilylation of benzaldehyde.[57] The creation of defects in MOFs can be achieved by the removal of either an organic linker, a metal node or a coordinated solvent molecule.[58] The introduction of defects in UiO-66(Zr) has a significant impact on its Lewis and Brønsted acidities. Increase of Lewis acidity was observed with the presence of defects in UiO-66(Zr), since additional coordinative unsaturated Zr ions were created.[59–61]

3.2.2 As catalyst support

Basically, a heterogeneous catalyst consists of active metal species and a support, with the chemical reactions usually occurring over the active sites at the surface of the catalyst. For this reason, porous materials with high surface area are promising catalyst supports for dispersing active metal species.

Porous carbon materials have been widely employed as catalytic supports for a diverse range of catalytic reactions, with catalytically active metal species deposited on the surface of the solid.[62,63] Depositing on porous carbon helps disperse of and reduces the sintering of metal species, where the interaction between support and metal species can also have great impact on the catalytic performance. Pd deposited on carbon serves as one typical heterogeneous catalyst for hydrogenation reaction. Hydrogenation of acetylene to ethylene over a Pd catalyst supported on porous carbon has been discussed in a previous report, where the interaction of porous carbon with Pd greatly enhances the selectivity towards ethylene.[64] In zeolites with well-defined porous structures, metal species have been introduced and encapsulated into the pores. This approach helps to prevent the procedures of Ostwald metal migration, thereby exhibiting improved

sintering resistance compared to conventional supported nanoparticles.[65–67] In addition, as the active metal sites are confined inside the pores, shape-selective catalysis can also be introduced into these catalyst systems. Using MOFs as hosts for metal nanoparticles has similar benefits with zeolites that can help dispersing metal species and prevent the metal sintering, while another important feature is the diversity of MOF compositions. It is relatively feasible to incorporate different functional groups, such as -OH, $-NH_2$, $-SO_3H$, etc., on the linkers of MOFs. These functional groups enhance the metal-support interaction and make MOFs suitable supports for metal nanoparticles.[55]

3.3 Release material

Based on the extensive application of porous materials as adsorbents, it is reasonable to consider that they can also be applied as release materials to subsequently release the adsorbed molecules. A typical example is applying a porous material as a drug carrier.[68,69] Porous materials with large pores and biocompatibility are ideally suited for adsorbing biomolecules. If one introduces the drug into porous materials and subsequently close the pores, it can travel innocuously in the body until a stimulus triggers the opening of the pores, allowing the drug to be released at the desired location. Typical stimuli are pH, light, temperature, ultrasound, etc. In this procedure, the pore size suitable for adsorption of biomolecules and the design of gated materials for 'open' the pores in response to stimuli are of great importance. Mesoporous silica and MOFs have been extensively studied as drug carrier for controlled-release of biomolecules.[69,70]

3.4 Characteristics used for applications

The widespread use of porous materials is attributed to their fascinating characteristics. While particular structures or related properties may be required for a specific application, the involved characteristics can also be multifarious. The typical characteristics of porous materials involved in different applications are depicted in **Figure 1-3**. A primary characteristic of porous materials is their high surface area. This high surface area provides ample opportunities for molecules to interact with the surface, making it crucial in diverse applications such as catalysis and adsorption. Regulated pore sizes are of great importance for gas separation, especially when selectivity is critical due to significant size differences among components. Moreover, the chemical composition of the porous materials can introduce intrinsic active sites capable for adsorption and catalysis.

Most of the applications are directly based on the features of pores and channels, leading to high adsorption capacity and giving active sites, while in addition to these, the characteristics of

pore walls are also of great importance. The regular structures of pore walls, namely pore walls in crystalline porous materials, are one of the important features that need to be highlighted. Comparing to common amorphous porous materials, the crystallographically well-defined pore walls of porous materials like zeolites and MOFs are particularly promising and attractive, as they can offer uniformly distributed and homogeneous active sites with high stability and activity. Further investigation on these ordered crystalline pore walls will provide valuable information for the rational design of materials with enhanced adsorption ability and high catalytic performance. Besides, the utilization of the functional groups on pore walls is crucial as they offer great opportunities to introduce active metal species and can tune the electronic properties of the immobilized active metal species.

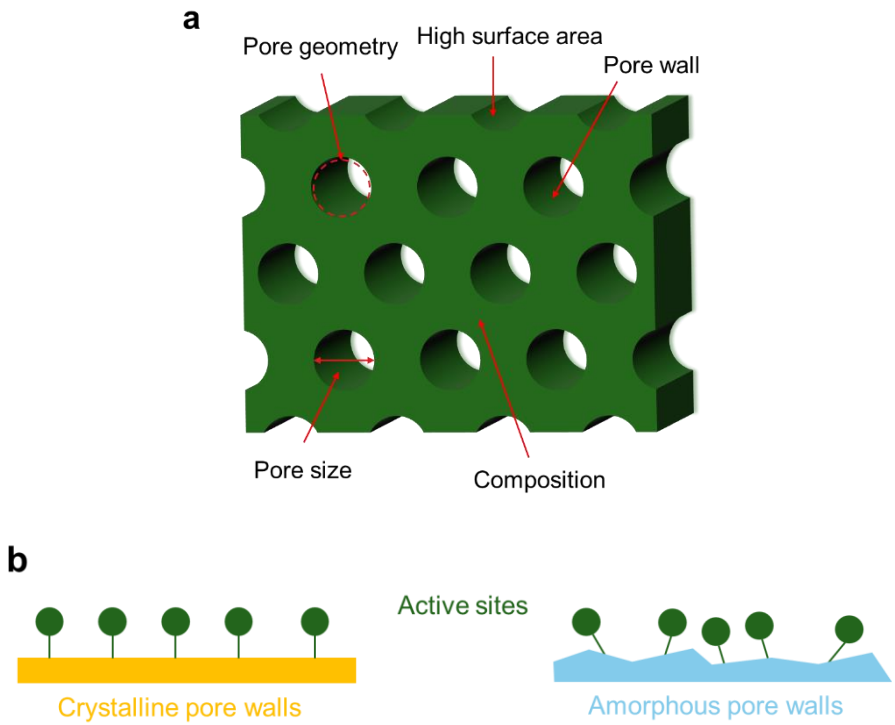

Figure 1-3. (a) Illustration of typical characteristics of porous materials involved in applications and (b) illustration of comparison between crystalline and amorphous pore walls in porous materials.

For instance, in microporous zeolites, the cation exchange sites located on the pore walls serve as functional groups for introducing active metal species. The interaction between zeolite framework and introduced active metal species can lead to enhanced performance in catalysis and adsorption. Similarly, the organic ligands constructing MOFs are available as functional groups

for introducing and tuning the characteristics of active metal species. With effective utilization, these functional groups on the pore walls of zeolites and MOFs can lead to enhanced performance in catalysis and adsorption.

4. The objective and outline of this thesis

Based on the factors mentioned above, the present author anticipated that the pore walls of crystalline porous materials are of great importance to introduce active species into porous materials applicable for catalysis and adsorption. Thus, this thesis focuses on the utilization of motifs on the pore walls of zeolites and MOFs, active metal species are further introduced to investigate the effect of these motifs on application for catalysis and adsorption.

In Chapter 2, a facile method to prepare uniform Pd nanoparticles on Al-based MOF (NH_2-MIL-53) is proposed. The critical role of amino group on the pore walls of NH_2-MIL-53 in introducing Pd and affecting the catalytic performance are discussed.

In Chapter 3, to develop promising ethylene encapsulation materials, adsorption behavior including adsorption capacity and adsorption strength of ethylene over a series of Ag^+-exchanged zeolites are systematically studied.

In Chapter 4, thermodynamic and kinetic release behavior of ethylene over different Ag^+-exchanged zeolites are systematically studied.

In Chapter 5, general conclusions and future scope are summarized.

5. References

(1) Slater, A. G.; Cooper, A. I. Function-Led Design of New Porous Materials. *Science* **2015**, *348* (6238), aaa8075. https://doi.org/10.1126/science.aaa8075.

(2) Zdravkov, B. D.; Čermák, J. J.; Šefara, M.; Janků, J. Pore Classification in the Characterization of Porous Materials: A Perspective. *Cent. Eur. J. Chem.* **2007**, *5* (2), 385–395. https://doi.org/10.2478/s11532-007-0017-9.

(3) Sing, K. S. W.; Everett, D. H.; Haul, R. A. W.; Moscou, L.; Pierotti, R. A.; Rouquerol, J.; Siemieniewska, T. Reporting Physisorption Data for Gas/Solid Systems with Special Reference to the Determination of Surface Area and Porosity. *Pure Appl. Chem.***1985***, 57,* (4), 603-619. https://doi.org/10.1351/pac198557040603.

(4) Thommes, M.; Kaneko, K.; Neimark, A. V.; Olivier, J. P.; Rodriguez-Reinoso, F.; Rouquerol, J.; Sing, K. S. W. Physisorption of Gases, with Special Reference to the Evaluation of Surface Area and Pore Size Distribution (IUPAC Technical Report). *Pure Appl. Chem.* **2015**, *87* (9–10), 1051–1069. https://doi.org/10.1515/pac-2014-1117.

(5) Davis, M. E.; Saldarriaga, C.; Montes, C.; Garces, J.; Crowder, C. VPI-5: The First Molecular Sieve with Pores Larger than 10 Angstroms. *Zeolites* **1988**, *8*, 362-366. https://doi.org/10.1016/S0144-2449(88)80172-6.

(6) Davis, M. E.; Saldarriaga, C.; Montes, C.; Garces, J.; Crowder, C.; Zhilan, H. A Molecular Sieve with Eighteen-Membered Rings. *Nature* **1988**, *331*, 698-699. https://doi.org/10.1038/331698a0.

(7) Corma, A.; Díaz-Cabañas, M. J.; Martínez-Triguero, J.; Rey, F.; Rius, J. A Large-Cavity Zeolite with Wide Pore Windows and Potential as an Oil Refining Catalyst. *Nature* **2002**, *418* (6897), 514–5147. https://doi.org/10.1038/nature00924.

(8) Lin, Q.-F.; Gao, Z. R.; Lin, C.; Zhang, S.; Chen, J.; Li, Z.; Liu, X.; Fan, W.; Li, J.; Chen, X.; Camblor, M. A.; Chen, F.-J. A Stable Aluminosilicate Zeolite with Intersecting Three-Dimensional Extra-Large Pores. *Science* **2021**, 374 (6575), 1605-1608. http://doi.org/10.1126/science.abk3258.

(9) Li, J.; Rei Gao, Z.; Lin, Q.-F.; Liu, C.; Gao, F.; Lin, C.; Zhang, S.; Deng, H.; Mayoral, A.; Fan, W.; Luo, S.; Chen, X.; He, H.; Camblor, M. A.; Chen, F.-J.; Yu, J. A 3D Extra-Large-Pore Zeolite Enabled by 1D-to-3D Topotactic Condensation of a Chain Silicate. *Science* **2023**, *379* (6629), 283-287. https://doi.org/10.1126/science.ade1771.

(10) Gao, Z. R.; Yu, H.; Chen, F. J.; Mayoral, A.; Niu, Z.; Niu, Z.; Li, X.; Deng, H.; Márquez-Álvarez, C.; He, H.; Xu, S.; Zhou, Y.; Xu, J.; Xu, H.; Fan, W.; Balestra, S. R. G.; Ma, C.; Hao, J.; Li, J.; Wu, P.; Yu, J.; Camblor, M. A. Interchain-Expanded Extra-Large-Pore Zeolites. *Nature* **2024**. https://doi.org/10.1038/s41586-024-07194-6.

(11) Kresge, C. T.; Leonowicz, M. E.; Roth, W. J.; Vartuli, J. C.; Beckt, J. S. Ordered Mesoporous

Molecular Sieves Synthesized by a Liquid-Crystal Template Mechanism. *Nature*, **1992**, *359*, 710-712. https://doi.org/10.1038/359710a0.

(12) Trewyn, B. G.; Slowing, I. I.; Giri, S.; Chen, H. T.; Lin, V. S. Y. Synthesis and Functionalization of a Mesoporous Silica Nanoparticle Based on the Sol-Gel Process and Applications in Controlled Release. *Acc. Chem. Res*. **2007**, *40* (9), 846–853. https://doi.org/10.1021/ar600032u.

(13) Wu, S. H.; Lin, H. P. Synthesis of Mesoporous Silica Nanoparticles. *Chem. Soc. Rev.* **2013**, *42* (9), 3862–3875. https://doi.org/10.1039/c3cs35405a.

(14) Nardecchia, S.; Carriazo, D.; Ferrer, M. L.; Gutiérrez, M. C.; Monte, F. Del. Three Dimensional Macroporous Architectures and Aerogels Built of Carbon Nanotubes and/or Graphene: Synthesis and Applications. *Chem. Soc. Rev.* **2013**, *42* (2), 794–830. https://doi.org/10.1039/c2cs35353a.

(15) Imhof, A.; Pine, D. Ordered Macroporous Materials by Emulsion Templating. *Nature* **1997**, *389*, 984-951. https://doi.org/10.1038/40105.

(16) Choi, M.; Cho, H. S.; Srivastava, R.; Venkatesan, C.; Choi, D. H.; Ryoo, R. Amphiphilic Organosilane-Directed Synthesis of Crystalline Zeolite with Tunable Mesoporosity. *Nat. Mater.* **2006**, *5* (9), 718–723. https://doi.org/10.1038/nmat1705.

(17) Egeblad, K.; Christensen, C. H.; Kustova, M.; Christensen, C. H. Templating Mesoporous Zeolites. *Chem. Mat.* **2008**, *20* (3), 946–960. https://doi.org/10.1021/cm702224p.

(18) Möller, K.; Bein, T. Mesoporosity - a New Dimension for Zeolites. *Chem. Soc. Rev.* **2013**, *42* (9), 3689–3707. https://doi.org/10.1039/c3cs35488a.

(19) Breck, D. W.; Eversole, W. G.; Milton, R. M.; Thomas, T. L. Crystalline Zeolites. I. The Properties of a New Synthetic Zeolite, Type A. *J. Am. Chem. Soc*. **1956**, *78* (23), 5963-5972. https://doi.org/10.1021/ja01604a001.

(20) Barrer, R. M. Zeolites and Their Synthesis. *Zeolites* **1981**, *1* (3), 130-140. https://doi.org/10.1016/S0144-2449(81)80001-2.

(21) Furukawa, H.; Cordova, K. E.; O'Keeffe, M.; Yaghi, O. M. The Chemistry and Applications of Metal-Organic Frameworks. *Science*. **2013**, *341* (6149). https://doi.org/10.1126/science.1230444.

(22) Anderson, P. W.; Brinkman, W. F.; Huse, D. A. Physics: Thermodynamics of an Incommensurate Quantum Crystal. *Science* **2005**, *310* (5751), 1164–1166. https://doi.org/10.1126/science.1118625.

(23) Beaudoin, D.; Maris, T.; Wuest, J. D. Constructing Monocrystalline Covalent Organic Networks by Polymerization. *Nat. Chem.* **2013**, *5* (10), 830–834. https://doi.org/10.1038/nchem.1730.

(24) He, Y.; Xiang, S.; Chen, B. A Microporous Hydrogen-Bonded Organic Framework for Highly Selective C_2H_2/C_2H_4 Separation at Ambient Temperature. *J. Am. Chem. Soc.* **2011**, *133* (37), 14570–14573. https://doi.org/10.1021/ja2066016.

(25) Lü, J.; Cao, R. Porous Organic Molecular Frameworks with Extrinsic Porosity: A Platform for Carbon Storage and Separation. *Angew. Chem. Int. Ed.* **2016**, *128* (33), 9624–9630.

https://doi.org/10.1002/ange.201602116.

(26) Budd, P. M.; Ghanem, B. S.; Makhseed, S.; McKeown, N. B.; Msayib, K. J.; Tattershall, C. E. Polymers of Intrinsic Microporosity (PIMs): Robust, Solution-Processable, Organic Nanoporous Materials. *Chem. Commun.* **2004**, *4* (2), 230–231. https://doi.org/10.1039/b311764b.

(27) Jiang, J. X.; Su, F.; Trewin, A.; Wood, C. D.; Campbell, N. L.; Niu, H.; Dickinson, C.; Ganin, A. Y.; Rosseinsky, M. J.; Khimyak, Y. Z.; Cooper, A. I. Conjugated Microporous Poly(Aryleneethynylene) Networks. *Angew. Chem. Int. Ed.* **2007**, *46* (45), 8574–8578. https://doi.org/10.1002/anie.200701595.

(28) Tan, L.; Tan, B. Hypercrosslinked Porous Polymer Materials: Design, Synthesis, and Applications. *Chem. Soc. Rev*. **2017**, *46*, 3322–3356. https://doi.org/10.1039/c6cs00851h.

(29) Giri, A.; Khakre, Y.; Shreeraj, G.; Dutta, T. K.; Kundu, S.; Patra, A. The Order-Disorder Conundrum: A Trade-off between Crystalline and Amorphous Porous Organic Polymers for Task-Specific Applications. *J. Mater. Chem. A* **2022**, *10*, 17077–17121. https://doi.org/10.1039/d2ta01546c.

(30) Khan, N. A.; Hasan, Z.; Jhung, S. H. Adsorptive Removal of Hazardous Materials Using Metal-Organic Frameworks (MOFs): A Review. *J. Hazard. Mater*. **2013**, *244*-245, 444–456. https://doi.org/10.1016/j.jhazmat.2012.11.011.

(31) Alsbaiee, A.; Smith, B. J.; Xiao, L.; Ling, Y.; Helbling, D. E.; Dichtel, W. R. Rapid Removal of Organic Micropollutants from Water by a Porous β-Cyclodextrin Polymer. *Nature* **2016**, *529* (7585), 190–194. https://doi.org/10.1038/nature16185.

(32) Roshanfekr Rad, L.; Anbia, M. Zeolite-Based Composites for the Adsorption of Toxic Matters from Water: A Review. *J. Environ. Chem. Eng.* **2021**, *9* (5). https://doi.org/10.1016/j.jece.2021.106088.

(33) Song, Y.; Phipps, J.; Zhu, C.; Ma, S. Porous Materials for Water Purification. *Angew. Chem. Int. Ed.* **2023**, *62*, e202216724. https://doi.org/10.1002/anie.202216724.

(34) Wang, S.; Peng, Y. Natural Zeolites as Effective Adsorbents in Water and Wastewater Treatment. *Chem. Eng. J*. **2010**, *156* (1), 11–24. https://doi.org/10.1016/j.cej.2009.10.029.

(35) Delkash, M.; Ebrazi Bakhshayesh, B.; Kazemian, H. Using Zeolitic Adsorbents to Cleanup Special Wastewater Streams: A Review. *Microporous Mesoporous Mater*. **2015**, *214*, 224–241. https://doi.org/10.1016/j.micromeso.2015.04.039.

(36) Hong, M.; Yu, L.; Wang, Y.; Zhang, J.; Chen, Z.; Dong, L.; Zan, Q.; Li, R. Heavy Metal Adsorption with Zeolites: The Role of Hierarchical Pore Architecture. *Chem. Eng. J.* **2019**, *359*, 363–372. https://doi.org/10.1016/j.cej.2018.11.087.

(37) Cychosz, K. A.; Matzger, A. J. Water Stability of Microporous Coordination Polymers and the Adsorption of Pharmaceuticals from Water. *Langmuir* **2010**, *26* (22), 17198–17202. https://doi.org/10.1021/la103234u.

(38) Jun, J. W.; Tong, M.; Jung, B. K.; Hasan, Z.; Zhong, C.; Jhung, S. H. Effect of Central Metal Ions of Analogous Metal-Organic Frameworks on Adsorption of Organoarsenic Compounds from Water:

Plausible Mechanism of Adsorption and Water Purification. *Chem. Eur. J.* **2015**, *21* (1), 347–354. https://doi.org/10.1002/chem.201404658.

(39) Gadipelli, S.; Guo, Z. X. Graphene-Based Materials: Synthesis and Gas Sorption, Storage and Separation. *Prog. Mater. Sci*. **2015**, *69*, 1–60. https://doi.org/10.1016/j.pmatsci.2014.10.004.

(40) Adil, K.; Belmabkhout, Y.; Pillai, R. S.; Cadiau, A.; Bhatt, P. M.; Assen, A. H.; Maurin, G.; Eddaoudi, M. Gas/Vapour Separation Using Ultra-Microporous Metal-Organic Frameworks: Insights into the Structure/Separation Relationship. *Chem. Soc. Rev*. **2017**, *46*, 3402–3430. https://doi.org/10.1039/c7cs00153c.

(41) Lin, R. B.; Xiang, S.; Xing, H.; Zhou, W.; Chen, B. Exploration of Porous Metal–Organic Frameworks for Gas Separation and Purification. *Coord. Chem. Rev*. **2019**, *378*, 87–103. https://doi.org/10.1016/j.ccr.2017.09.027.

(42) Okamoto, K. I.; Kita, H.; Horii, K.; Tanaka, K.; Kondo, M. Zeolite NaA Membrane: Preparation, Single-Gas Permeation, and Pervaporation and Vapor Permeation of Water/Organic Liquid Mixtures. *Ind. Eng. Chem. Res.* **2001**, *40* (1), 163–175. https://doi.org/10.1021/ie0006007.

(43) Padin, J.; Rege, S. U.; Yang, R. T.; Cheng, L. S. Molecular Sieve Sorbents for Kinetic Separation of Propane/Propylene. *Chem. Eng. Sci*. **2000**, *55* (20), 4525-4535. https://doi.org/10.1016/S0009-2509(00)00099-3.

(44) Li, L.; Lin, R. B.; Wang, X.; Zhou, W.; Jia, L.; Li, J.; Chen, B. Kinetic Separation of Propylene over Propane in a Microporous Metal-Organic Framework. *Chem. Eng. J.* **2018**, *354*, 977–982. https://doi.org/10.1016/j.cej.2018.08.108.

(45) Kuah, W. C.; Effendy, S.; Farooq, S. Industrial Scale Propylene/Propane Separation Using Pressure Vacuum Swing Adsorption. *Ind. Eng. Chem. Res.* **2018**, *57* (18), 6451–6463. https://doi.org/10.1021/acs.iecr.8b00289.

(46) Yang, R. T. *ADSORBENTS: FUNDAMENTALS AND APPLICATIONS*. 1st ed.; John Wiley & Sons, Inc. 2003. DOI:10.1002/047144409X.

(47) Ding, M.; Flaig, R. W.; Jiang, H. L.; Yaghi, O. M. Carbon Capture and Conversion Using Metal-Organic Frameworks and MOF-Based Materials. *Chem. Soc. Rev*. **2019**, *48*, 2783–2828. https://doi.org/10.1039/c8cs00829a.

(48) Bao, Z.; Yu, L.; Ren, Q.; Lu, X.; Deng, S. Adsorption of CO_2 and CH_4 on a Magnesium-Based Metal Organic Framework. *J. Colloid. Interface. Sci.* **2011**, *353* (2), 549–556. https://doi.org/10.1016/j.jcis.2010.09.065.

(49) Millward, A. R. and Yaghi, O. M. Metal-Organic Frameworks with Exceptionally High Capacity for Storage of Carbon Dioxide at Room Temperature. *J. Am. Chem. Soc.* **2005**, *127* (51), 17998-17999. https://doi.org/10.1021/ja0570032.

(50) Loewenstein, W. The Distribution of Aluminum in the Tetrahedra of Silicates and Aluminates. *Am.*

Min. **1954**, *39* (1–2), 92–96.

(51) Csicsery, S. M. Shape-Selective Catalysis in Zeolites. *Zeolites* **1984**, *4* (3), 202-213. https://doi.org/10.1016/0144-2449(84)90024-1

(52) Biswas, J.; Maxwell, I. E. Recent Process- and Catalyst-Related Developments in Fluid Catalytic Cracking. *Appl. Catal*. **1990**, *63* (1), 197-258. https://doi.org/10.1016/S0166-9834(00)81716-9.

(53) Dwyer, F. G.; Degnan, T. F. Chapter 13 Shape Selectivity in Catalytic Cracking. *Studies in Surface Science and Catalysis*; Magee, J. S., Mitchell, M. M., Eds.; Elsevier, 1993; Vol. 76, pp 499–530. https://doi.org/https://doi.org/10.1016/S0167-2991(08)63836-7.

(54) Jiao, L.; Wang, Y.; Jiang, H. L.; Xu, Q. Metal–Organic Frameworks as Platforms for Catalytic Applications. *Adv. Mater.* **2018**, *30*, 1703663. https://doi.org/10.1002/adma.201703663.

(55) Bavykina, A.; Kolobov, N.; Khan, I. S.; Bau, J. A.; Ramirez, A.; Gascon, J. Metal-Organic Frameworks in Heterogeneous Catalysis: Recent Progress, New Trends, and Future Perspectives. *Chem. Rev*. **2020**, *120* (16), 8468–8535. https://doi.org/10.1021/acs.chemrev.9b00685.

(56) Akiyama, G.; Matsuda, R.; Sato, H.; Takata, M.; Kitagawa, S. Cellulose Hydrolysis by a New Porous Coordination Polymer Decorated with Sulfonic Acid Functional Groups. *Adv. Mater.* **2011**, *23* (29), 3294–3297. https://doi.org/10.1002/adma.201101356.

(57) Schlichte, K.; Kratzke, T.; Kaskel, S. Improved Synthesis, Thermal Stability and Catalytic Properties of the Metal-Organic Framework Compound $Cu_3(BTC)_2$. *Microporous Mesoporous Mater.* **2004**, *73* (1–2), 81–88. https://doi.org/10.1016/j.micromeso.2003.12.027.

(58) Dissegna, S.; Epp, K.; Heinz, W. R.; Kieslich, G.; Fischer, R. A. Defective Metal-Organic Frameworks. *Adv. Mater.* **2018**, *30*, 1704501. https://doi.org/10.1002/adma.201704501.

(59) Wu, H.; Chua, Y. S.; Krungleviciute, V.; Tyagi, M.; Chen, P.; Yildirim, T.; Zhou, W. Unusual and Highly Tunable Missing-Linker Defects in Zirconium Metal-Organic Framework UiO-66 and Their Important Effects on Gas Adsorption. *J. Am. Chem. Soc.* **2013**, *135* (28), 10525–10532. https://doi.org/10.1021/ja404514r.

(60) Ling, S.; Slater, B. Dynamic Acidity in Defective UiO-66. *Chem. Sci.* **2016**, *7* (7), 4706–4712. https://doi.org/10.1039/c5sc04953a.

(61) Chakarova, K.; Strauss, I.; Mihaylov, M.; Drenchev, N.; Hadjiivanov, K. Evolution of Acid and Basic Sites in UiO-66 and UiO-66-NH_2 Metal-Organic Frameworks: FTIR Study by Probe Molecules. *Microporous Mesoporous Mater.* **2019**, *281*, 110–122. https://doi.org/10.1016/j.micromeso.2019.03.006.

(62) Su, D. S.; Perathoner, S.; Centi, G. Nanocarbons for the Development of Advanced Catalysts. *Chem. Rev*. **2013**, *113* (8), 5782–5816. https://doi.org/10.1021/cr300367d.

(63) Pérez-Mayoral, E.; Calvino-Casilda, V.; Soriano, E. Metal-Supported Carbon-Based Materials: Opportunities and Challenges in the Synthesis of Valuable Products. *Catal. Sci. Tech*. **2016**, *6*, 1265–

1291. https://doi.org/10.1039/c5cy01437a.

(64) Benavidez, A. D.; Burton, P. D.; Nogales, J. L.; Jenkins, A. R.; Ivanov, S. A.; Miller, J. T.; Karim, A. M.; Datye, A. K. Improved Selectivity of Carbon-Supported Palladium Catalysts for the Hydrogenation of Acetylene in Excess Ethylene. *Appl. Catal. A Gen.* **2014**, *482*, 108–115. https://doi.org/10.1016/j.apcata.2014.05.027.

(65) Zhang, J.; Wang, L.; Zhang, B.; Zhao, H.; Kolb, U.; Zhu, Y.; Liu, L.; Han, Y.; Wang, G.; Wang, C.; Su, D. S.; Gates, B. C.; Xiao, F.-S. Sinter-Resistant Metal Nanoparticle Catalysts Achieved by Immobilization within Zeolite Crystals via Seed-Directed Growth. *Nat. Catal.* **2018**, *1* (7), 540–546. https://doi.org/10.1038/s41929-018-0098-1.

(66) Wang, H.; Wang, L.; Xiao, F. S. Metal@zeolite Hybrid Materials for Catalysis. *ACS Cent. Sci.* **2020**, *6* (10), 1685–1697. https://doi.org/10.1021/acscentsci.0c01130.

(67) Zhang, Q.; Gao, S.; Yu, J. Metal Sites in Zeolites: Synthesis, Characterization, and Catalysis. *Chem. Rev*. **2023**, *123* (9), 6039–6106. https://doi.org/10.1021/acs.chemrev.2c00315.

(68) Aznar, E.; Oroval, M.; Pascual, L.; Murguía, J. R.; Martínez-Máñez, R.; Sancenón, F. Gated Materials for On-Command Release of Guest Molecules. *Chem. Rev*. **2016**, *116* (2), 561–718. https://doi.org/10.1021/acs.chemrev.5b00456.

(69) Zhu, J.; Niu, Y.; Li, Y.; Gong, Y.; Shi, H.; Huo, Q.; Liu, Y.; Xu, Q. Stimuli-Responsive Delivery Vehicles Based on Mesoporous Silica Nanoparticles: Recent Advances and Challenges. *J. Mater. Chem. B*. **2017**, *5*, 1339–1352. https://doi.org/10.1039/C6TB03066A.

(70) Yang, J.; Yang, Y. W. Metal–Organic Frameworks for Biomedical Applications. *Small* 2020, 16, 1906846. https://doi.org/10.1002/smll.201906846.

Chapter 2

NH_2-MIL-53 supported Pd nanoparticles with uniform distribution for catalytic reduction of nitrite in water

1. Introduction

Metal-organic frameworks (MOFs) are a class of porous materials and constructed by the bonding between inorganic metal nodes and organic linkers to form periodic and high-dimensional crystalline networks.[1,2] By this, MOFs have special character of well-defined pore structures and high surface areas, which give them high accessibility to reactant molecules. Thus, these materials have attracted great attention to the application in heterogeneous catalysis. The presence of coordinatively unsaturated metal sites in the structure can help adsorption and activation of reactant molecules, and some specific functional organic groups (e. g. amide, pyridyl) on organic linkers can also be used as active sites, getting pristine MOFs to act as a solid catalyst.[3–6] Besides the direct use of MOFs, applying MOFs as a support material for embedding and fixing catalytically active metal nanoparticles (MNPs) is another promising way to develop high performance catalysts. The three-dimensionally ordered structure and high porosity can facilitate the uniform dispersion of MNPs, meanwhile can suppress the migration and aggregation of MNPs to avoid catalyst deactivation.[7–11] Furthermore, the functional groups on organic linkers in MOF can facilitate in controlling the electronic state of the dispersed metal species by charge transfer from the functional groups to metal species and *vice versa*.[12,13]

In the last decade, several approaches to prepare MNPs in MOFs (MNPs@MOF) have been reported, which include solvent-free gas-phase loading, incipient wetness impregnation, solid grinding and one-pot strategy. The synthesized MNPs@MOF were then applied as a catalyst for various organic conversion reactions, where the effects of functional groups in MOF or/and the pore structure were discussed.[14–17] For instance, two functional groups, which are $-SO_3H$ and $-NH_2$, were attached to UiO-66 to form UiO-66-S and UiO-66-N, respectively, and Pt nanoparticles (NPs) were further embedded into them.[18] It was found that those functional groups played a critical role in selective conversion of methylcyclopentane, where Pt@UiO-66-S promoted the formation of C_6-cyclic products, while Pt@UiO-66-N facilitated that of acyclic isomer.[18]

Apart from the utilization of MOF as solid catalysts in organic media, the application of MOF-based catalysts in aqueous one is also noteworthy from the viewpoint of environmentally benign organic synthesis, because water is considered as a non-toxic and environmentally benign solvent. Moreover, the application of MOFs in water is essential as water treatment is still a huge task currently. However, a general concern is raised that MOFs do not have sufficient stability in water. In fact, most MOFs are highly sensitive to water, while high-valence metal ions like Al^{3+}, Fe^{3+}, Cr^{3+} and Zr^{4+} have been reported to give water stable MOFs, such as well-known UiO-66, PCN, MIL-53 and MIL-101.[19,20]

In this study, Al-based NH_2-MIL-53, which is an analogue of MIL-53, was chosen as a catalyst support to discuss the effect of amino group in the linker on the introduction of Pd NPs to the MOF and on catalytic performance in water. MIL-53 was first reported by Férey et al. in 2004, and is an aluminum dicarboxylate Al(OH)(BDC) (BDC=1,4-benzenedicarboxylate) isostructural to Cr-based MIL-53. The framework of Al-based MIL-53 is built up of infinite chains of corner-sharing $AlO_4(OH)_2$ octahedra interconnected with dicarboxylate groups on BDC, resulting in a crystalline structure containing one-dimensional diamond-shape channels with pores of free diameter close to 0.85 nm (**Figure 2-1**).[21] NH_2-MIL-53 exhibits similar crystal structure to MIL-53 and can be synthesized under mild conditions by using NH_2-BDC instead of BDC.[22]

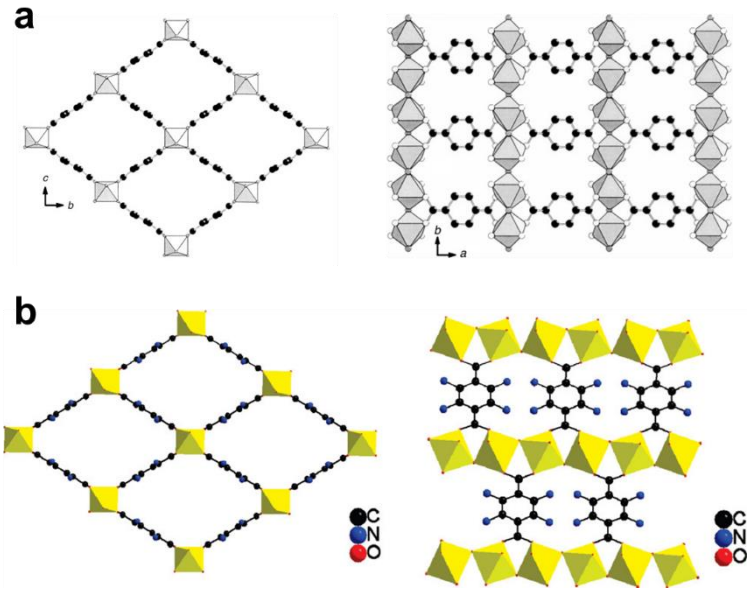

Figure 2-1. (a) View of crystal structure of MIL-53 along (left) and perpendicular to (right) the pore system (from ref. 21). Grey octahedra: $AlO_4(OH)_2$; black circles: carbon; grey circles: oxygen. (b) View of crystal structure of NH_2-MIL-53 along (left) and perpendicular to (right) the pore system (from ref. 22). Yellow octahedra: $AlO_4(OH)_2$. N positions are shown by the possible positions and only occupied by one-fourth.

Here, the present author wishes to propose an easy way to introduce Pd NPs into NH_2-MIL-53, which is just mixing NH_2-MIL-53 with an aqueous solution of $PdCl_2$ under ambient conditions (called equilibrium adsorption method here), followed by the reduction with $NaBH_4$. The obtained Pd@NH_2-MIL-53 was applied as a catalyst for reduction of nitrite (NO_2^-) with H_2 in water. A monometallic Pd system rather than a bimetallic system was selected in this study as it is easier

to discuss the support effect on the catalytic performance. Nitrate (NO_3^-) is a pollutant commonly found in natural water and reduction of NO_3^- over Pd-based bimetallic catalyst like Pd-Cu, Pd-Sn and Pd-In gives NO_2^- as an intermediate product.[23–28] Since the reduction of NO_2^- proceeds over Pd sites in the Pd-based bimetallic catalysts[29–31], this reaction determines the selectivity between N_2 and NH_3 as end products in the NO_3^- reduction (**Scheme 2-1**). Thus, studying the NO_2^- reduction has important implications in demonstrating the usefulness of Pd@NH_2-MIL-53 as an environmental catalyst for water purification.

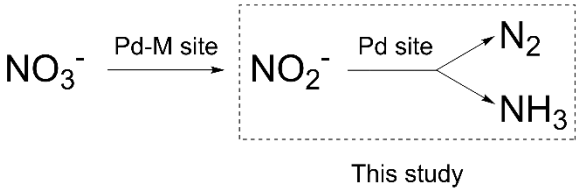

Scheme 2-1. Reaction pathway for NO_3^- reduction over a Pd-based bimetallic catalyst.

2. Experimental

2.1 Materials

All chemicals used in this study were commercially available and used as received without further treatment. Palladium (II) chloride ($PdCl_2$, 99.0%), hydrochloric acid (HCl, 35.0~37.0%), sodium nitrite ($NaNO_2$, 98.5%), aluminum(III) nitrate nonahydrate [$Al(NO_3)_3 \cdot 9H_2O$, >98.0%], sodium hydroxide (NaOH, 97.0%), N,N-dimethylformamide (DMF, >99.5%), ethanol (>99.5%), acetone (>99.5%), sodium borohydride ($NaBH_4$, 95.0%) and terephthalic acid (H_2BDC) were purchased from FUJIFILM Wako Pure Chemical Corporation. 2-Aminoterephthalic acid (NH_2-H_2BDC, 99%) was purchased from Sigma-Aldrich Co. Ultra-pure water (Milli-Q) was used for all the experiments.

2.2 Synthesis of MOFs

NH_2-MIL-53 was synthesized according to the method in a reference[32]with small modifications. The organic linker, NH_2-H_2BDC, (4.14 mmol) was dissolved in 6 mL of aqueous NaOH solution (1.5 mol L^{-1}) and the solution was stirred for 30 min at room temperature, forming dark yellow solution (**Solution 1**). Another solution (**Solution 2**) was prepared by dissolving $Al(NO_3)_3 \cdot 9H_2O$ (4.14 mmol) in 4 mL of Milli-Q water. Then, **Solution 2** was added dropwise at room temperature into **Solution 1** under vigorous stirring. After being stirred at room temperature

for 24 h, the resulting yellow solid was separated by centrifugation at 10000 rpm and washed with Milli-Q water and ethanol. The collected solid was then dried at 100 °C overnight, subsequently immersed in 30 mL of DMF at 150 °C for 5 h to exchange free NH_2-H_2BDC remaining in the pore with DMF. Then the powder was collected by filtration, washed with ethanol and acetone, and was dried at 100 °C overnight. The solid after drying was heated at 250 °C for 3 h to evaporate and remove DMF.

MIL-53 was synthesized with the similar manner to that for NH_2-MIL-53, but H_2BDC was used as an organic linker instead of NH_2-H_2BDC.

2.3 Introduction of Pd to MOFs

2.3.1 Equilibrium adsorption method

Pd was introduced to NH_2-MIL-53 by the equilibrium adsorption method as follows. NH_2-MIL-53 was dispersed in an aqueous $PdCl_2$ solution (10 mmol L^{-1}), whose pH was adjusted to 4 by adding NaOH under stirring. After overnight stirring, the mixture was filtrated and the solid on the filter was washed with Milli-Q (50 mL × 3 times), followed by drying at 100 °C overnight. After that, the obtained solid was treated in an aqueous $NaBH_4$ solution (0.1 mol L^{-1}) at 25 °C for 30 min to reduce Pd species, forming Pd NPs. Then, the solid was collected by filtration, washed with Milli-Q (50 mL × 3 times) and dried at 100 °C overnight.

Pd@NH_2-MIL-53 with different Pd loadings (denoted as Pd@NH_2-MIL-53_x, x represents the actual Pd content, wt.%) were also prepared by changing the concentration of $PdCl_2$ in the solution, while the volume of the solution remained constant.

Introduction of Pd into MIL-53 by the equilibrium adsorption method was also conducted in the same way as that for Pd@NH_2-MIL-53, and the obtained catalyst was denoted as Pd@MIL-53.

2.3.2 Impregnation method

Introduction of Pd to MOFs (NH_2-MIL-53 and MIL-53) were also conducted by a conventional impregnation method. MOF was dispersed in an aqueous $PdCl_2$ solution (10 mmol L^{-1}) and then, the suspension was evaporated at 50 °C with a rotary evaporator to remove the solvent. The resulting solid was dried at 100 °C overnight and treated with $NaBH_4$ in the same manner as for Pd@NH_2-MIL-53. These catalysts prepared by the impregnation method are denoted as Pd/NH_2-MIL-53 and Pd/MIL-53.

2.4 Characterization

Powder X-ray diffraction (PXRD) patterns were collected on an X-ray diffractometer (D2 Phaser, Bruker) using Cu Kα radiation at a 0.02° step in the 2θ range of 5° to 50°. The specific surface area was estimated from a N_2 adsorption isotherm taken at -196 °C (BELSORP mini, BEL Japan, Inc). Before measurement, the sample was treated in N_2 flow at 130 °C for 2 h. The specific surface area was calculated by applying Brunauer-Emmett-Teller (BET) equation to an adsorption branch in the P/P_0 range of 0 to 0.05. Thermogravimetric and differential thermal analysis (TG-DTA) was performed on TG 8120 (Thermo plus TG8120, Rigaku) from room temperature to 600 °C in air flow at a heating rate of 5 °C min^{-1}. Morphology of the samples was observed by a field emission scanning electron microscopy (FE-SEM, S4800, HITACH). Particle size distribution and mean particle size of Pd particles in the samples were estimated from transmission electron microscope images taken on a transmission electron microscope (TEM, JEM 2100F, JEOL) with electron acceleration voltage of 200 kV.

Fourier transform infrared (FT-IR) spectra of CO adsorbed on the samples were recorded on an IR spectrometer (FT/IR-6100, JASCO Co.) equipped with an MCT detector. Prior to the measurement, ca. 40 mg of the sample was pressed into a self-supporting disk, and it was placed in a quartz IR cell equipped with CaF_2 windows connected to a gas flow system. The sample disk was heated in H_2 flow (10 mL min^{-1}) at 100 °C for 30 min and then cooled to 25 °C in N_2 flow (30 mL min^{-1}). After the temperature reached to 25 °C, 5% CO in N_2 was fed into the cell for 10 min. After that, the gas was switched to N_2 to remove weakly adsorbed CO and IR spectrum was recorded at 25 °C.

The content of Pd in the samples was quantified using an inductively coupled plasma-atomic emission spectrometer (ICPE-9000, Shimazu Co.). The samples were calcined at 800 °C for 3 h to combust all the organic moieties and the obtained solid was treated with an aqueous $NaBH_4$ solution to reduce oxidized Pd species to Pd^0. Then, all the solid was dissolved in aqua regia, and the solution was diluted with water to afford the measurement.

Chemical elemental analyses of C, H and N for the samples were carried out with a CHN analyzer (CE440, Exeter Analytical, Inc) at Global Facility Center, Hokkaido University. For Cl analysis, the sample was dissolved in a concentrated aqueous NaOH solution, and the solution was analyzed by ion chromatography (IC) in the same way as the analysis of NO_2^- in reaction solution, which will be explained in detail later.

2.5 Evaluation of catalytic performance

Reduction of NO_2^- with H_2 in water was carried out in a round-bottom flask connected with a gas flow system. Normally, catalyst (ca. 20 mg), 100 mL of aqueous $NaNO_2$ solution (10 mmol L^{-1}) and 50 mL of Milli-Q water were put in the flask, where the concentration of NO_2^- was 6.67 mmol L^{-1}. After bubbling with N_2 (30 mL min^{-1}) for 30 min to remove dissolved oxygen from the solution, mixed gas composed of H_2 (50 mL min^{-1}) and CO_2 (50 mL min^{-1}) was flown to start the reaction. The reaction was conducted at room temperature (25 °C) for 4 h with magnetic stirring (500 rpm). To trap formed NH_3, two traps with diluted H_2SO_4 were set at the outlet of the reactor.

A small portion of the reaction solution (1 mL) was taken at regular time interval and centrifuged to separate catalyst from the solution. The concentration of NO_2^- in supernatant was measured using an ion chromatograph (IC-8100, Tosoh) equipped with a TSK gel Super IC-AZ column. The concentrations of ammonium ion (NH_4^+) in the reaction and trap solution were determined using another ion chromatograph (IC-2001 Tosoh,) equipped with a TSK gel Super IC-CR column.

Reaction rate constant was calculated from the data at a conversion of NO_2^- less than 20%, assuming pseudo-first-order reaction for NO_2^- concentration (**equation 1**),

$$-\frac{d[NO_2^-]}{dt} = k_{obs} \times [NO_2^-] \quad (1)$$

where $[NO_2^-]$ and k_{obs} are concentration of NO_2^- at reaction time t and pseudo-first-order rate constant, respectively.

Specific activity per surface Pd site (k_s, mmol h^{-1} $mmol_{Pd}^{-1}$), which is so-called turnover frequency, for nitrite reduction was calculated by dividing the pseudo-first-order rate constant (k_{obs}) and the initial nitrite amount ($n_{nitrite}$, mmol) by the number of the Pd sites exposed on the surface ($n_{surface\ Pd}$, mmol) as **equation 2**,

$$k_s = \frac{k_{obs} \times n_{nitrite}}{n_{surface\ Pd}} = \frac{k_{obs} \times n_{nitrite}}{n_{Pd} \times D} \quad (2)$$

where D is dispersion of Pd (i.e., ratio of the number of Pd atoms exposed on the surface to the total number of Pd atoms in the catalyst) and is calculated from the average Pd particle size estimated from TEM images, assuming the shape of Pd particles to be spherical,[33–35] n_{Pd} is the total Pd amount (mmol) in the catalyst.

Selectivity to NH_4^+ ($S_{NH_4^+}$) was calculated according to **equation 3**,

$$S_{NH_4^+} = \frac{[NH_4^+]_t}{[NO_2^-]_0 - [NO_2^-]_t} \times 100 \quad (3)$$

Selectivity to N_2 was calculated by assuming that only N_2 and NH_4^+ were the end-products in the reaction (**equation 4**),

$$S_{N_2} = 100 - S_{NH_4^+} \quad (4)$$

3. Results and discussion

3.1 Catalyst characterization

First, the influence of amino group in the organic linker on the introduction of Pd NPs by the equilibrium adsorption method was investigated. The amounts of Pd introduced in the samples, namely actual Pd loadings, were determined by ICP-AES, and the results are listed in **Table 2-1**.

Table 2-1. Added and actual Pd loadings for the samples.

Sample	Pd loading (wt.%)	
	Added	Actual*
Pd@NH_2-MIL-53_0.5	0.5	0.5
Pd@NH_2-MIL-53_0.8	1.0	0.8
Pd@NH_2-MIL-53_2.1	3.0	2.1
Pd@NH_2-MIL-53_2.6	5.0	2.6
Pd@NH_2-MIL-53_3.5	8.0	3.5
Pd/NH_2-MIL-53	3.0	3.2
Pd@MIL-53	3.0	~ 0**
Pd/MIL-53	3.0	5.0

*Determined by ICP-AES. **Not detected.

For Pd@MIL-53 which does not have amino group in the organic linker, no Pd was introduced by the equilibrium adsorption method. In contrast, Pd was successfully incorporated into NH_2-MIL-53 by the method as demonstrated in **Table 2-1**. For example, 2.1 wt.% Pd was loaded onto NH_2-MIL-53 when Pd equivalent to 3.0 wt.% was added (Pd@NH_2-MIL-53_2.1). A reasonable explanation why MIL-53 failed while NH_2-MIL-53 succeeded to incorporate Pd by the equilibrium adsorption method is that amino group in the organic linker acted as binding site for Pd species. To know how Pd species was introduced into NH_2-MIL-53, relationship between actual Pd loading and the amount of amino group was investigated. The amount of N determined by chemical elemental analysis was regarded as that of amino group present in NH_2-MIL-53, which was 3.18 mmol g^{-1}. **Figure 2-2** shows the relationship between expected and actual Pd/N molar ratios for Pd@NH_2-MIL-53 with different Pd loadings, where the expected ratios were calculated from the amount of added Pd.

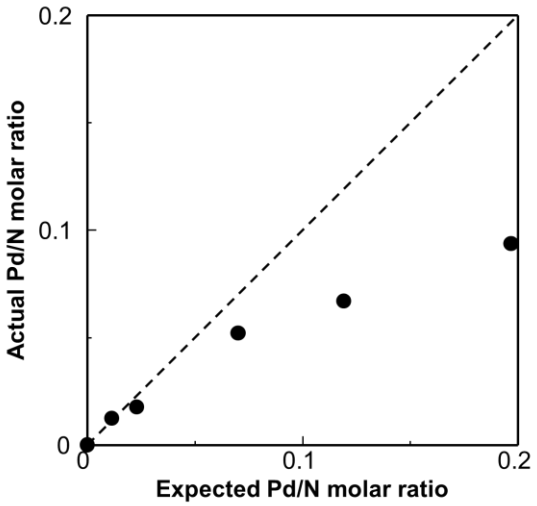

Figure 2-2. Relationship between actual and expected Pd/N molar ratios for Pd@NH_2-MIL-53.

As **Figure 2-2** shows, the actual Pd/N molar ratio was increased with increase in the expected one but was always lower than the latter even in the low expected Pd/N ratio. This implied that the interaction between amino group in the organic linker and Pd species was not so strong that only a part of amino groups was occupied by the Pd species under the conditions in the adsorption equilibrium method. Hereafter, the actual Pd loading is called just Pd loading.

To know what Pd species being introduced in NH_2-MIL-53, the amounts of Cl in the samples after the introduction of Pd but before the reduction with $NaBH_4$ were determined by ion chromatography. In **Figure 2-3**, actual Cl/Pd ratios are plotted as a function of the Pd loadings.

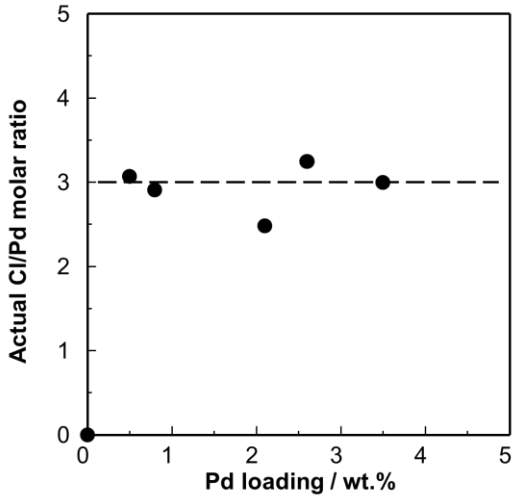

Figure 2-3. Relationship between Pd loading and actual Cl/Pd ratio.

As **Figure 2-3** demonstrates, the Cl/Pd molar ratios were always approximately 3 regardless of the Pd loadings. In the separate experiment, NH_2-MIL-53 was treated in dilute hydrochloric acid without $PdCl_2$, whose pH was also adjusted to 4 by adding NaOH, and it was found that no Cl was taken in NH_2-MIL-53. Therefore, it was obvious that all Cl present in Pd@NH_2-MIL-53 before the $NaBH_4$ reduction were attached to the Pd species, meaning that three Cl were coordinated to one Pd atom. It is known that Pd species exists in an aqueous solution containing Cl^- as anionic chloropalladium(II) complexes including $(PdCl_4)^{2-}$, $(PdCl_3)^-$ and $[PdCl_3(H_2O)]^-$, or cationic ones like $(PdCl)^+$ and hydrated Pd^{2+}, or nonionic $PdCl_2$, whose abundance ratio is changed depending on the concentrations of Pd^{2+} and Cl^-, and pH.[36] The fact that the actual Cl/Pd ratio was 3 indicated that $(PdCl_3)^-$ was a predominant species in Pd@NH_2-MIL-53 before the reduction with $NaBH_4$. Since the aqueous $PdCl_2$ solution used in this study was acidic (pH 4), almost all amino groups in NH_2-MIL-53 must be protonated, if p*K*a of common amino groups (around 9) are considered. Therefore, $(PdCl_3)^-$ was electrostatically interacted with protonated amino group forming $-NH_3^+$---$(PdCl_3)^-$ ion pair. After the reduction with $NaBH_4$, Cl were totally removed from the samples, indicating that amino group was fully recovered in Pd@NH_2-MIL-53.

The crystalline structures of pristine MOFs (MIL-53 and NH_2-MIL-53) and those after the introduction of Pd were investigated by PXRD. The PXRD pattern (**Figure 2-4**) of MIL-53 was basically identical to that in a previous paper[32] and NH_2-MIL-53 gave a PXRD pattern almost identical to that of MIL-53, indicating that amino group in the organic linker had little impact on the framework structure of the MOF. For Pd/NH_2-MIL-53 and Pd/MIL-53 where Pd was introduced by an impregnation method, the intensities of the peak at $2\theta = 8.7°$, which was assigned to (101) plane of the MOFs, were very weak comparing with those for the pristine MOFs, indicating the framework structure were severely decomposed. The $PdCl_2$ solution used in this study was prepared by adding hydrochloric acid to dissolve $PdCl_2$, to which NaOH was added in order to adjust pH 4. This solution gradually became concentrated as the solvent (water) was evaporated during the operation of the impregnation, and thus acidity of the solution became so high. The MOFs (MIL-53 and NH_2-MIL-53) are unstable in highly acidic solution[37] because the organic linker must exist as a carboxylate anion. Thus, the framework structure was severely damaged during the Pd introduction by the impregnation method.

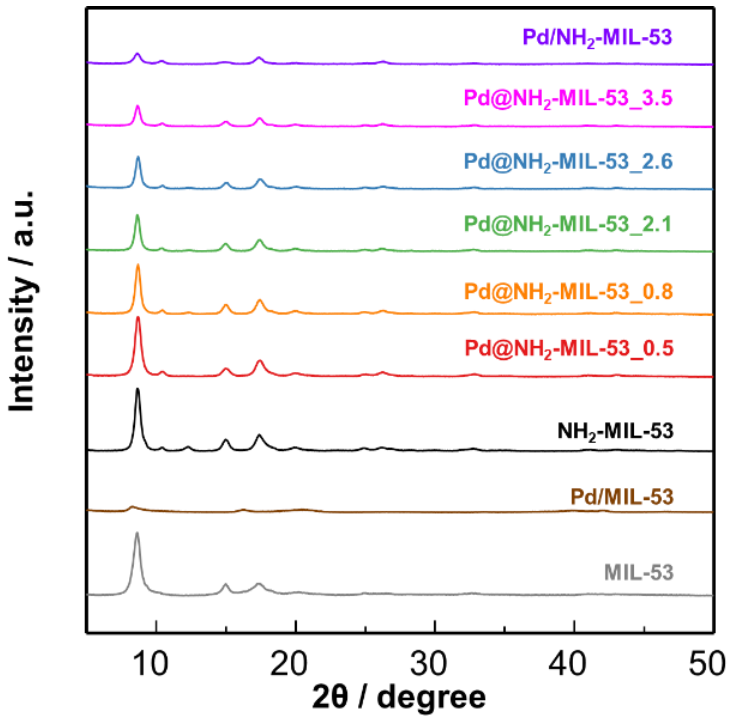

Figure 2-4. PXRD patterns of pristine MOFs and Pd-introduced ones.

In contrast, Pd@NH_2-MIL-53 prepared by the equilibrium adsorption method had still high crystallinity, while the intensities of the peaks became weak with increase in the Pd loadings. Such decrease of the diffraction peak intensities can be attributed to a certain loss of crystallinity or due to the presence of heavy metal like Pd inside the pore which scatters incident X-ray.[38] However, as shown in **Figure 2-5**, since there was no difference in the peak intensities between before and after the reduction with $NaBH_4$, it is highly unlikely that X-ray scattering by Pd was the reason for decrease of that diffraction peak intensities. As will be mentioned later, since the surface area of NH_2-MIL-53 was decreased with the Pd introduction, partial decomposition of the framework structure of NH_2-MIL-53 during the Pd introduction in the adsorption equilibrium method was more plausible. While the Pd solution was not concentrated in the adsorption equilibrium method unlike the case in the impregnation method, the solution was weakly acidic (pH 4) and thus the framework structure of NH_2-MIL-53 might be partly decomposed in that solution. It should be noted that characteristic diffraction peaks corresponding to Pd^0 particles were not observed for Pd@NH_2-MIL-53, suggesting that well-dispersed Pd NPs were formed even for the samples with high Pd loadings like Pd@NH_2-MIL-53_3.5.

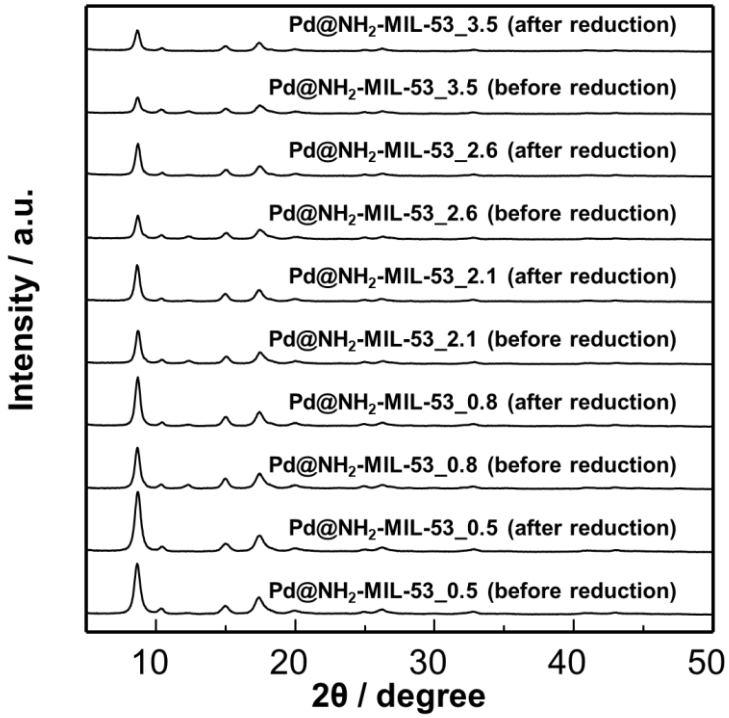

Figure 2-5. PXRD patterns of Pd@NH_2-MIL-53 before and after reduction with $NaBH_4$.

The morphology of the pristine NH_2-MIL-53 and those after the introduction of Pd NPs with different preparation methods were investigated by SEM. As shown in **Figures 2-6a** and **b**, the pristine NH_2-MIL-53 composed of small spherical particles with particle size in the range of 10–20 nm. After the introduction of Pd by the impregnation method, morphological collapse, which was that the surface of the crystal agglomerates turned rougher and the agglomerates looked to be dissolved, was observed for Pd/NH_2-MIL-53 (**Figure 2-6c**). In contrast, such morphological change was not significant for Pd@NH_2-MIL-53 prepared by the equilibrium adsorption method (**Figure 2-6d**). Besides, no significant morphological change was observed when the Pd loading was increased (**Figure 2-6e**).

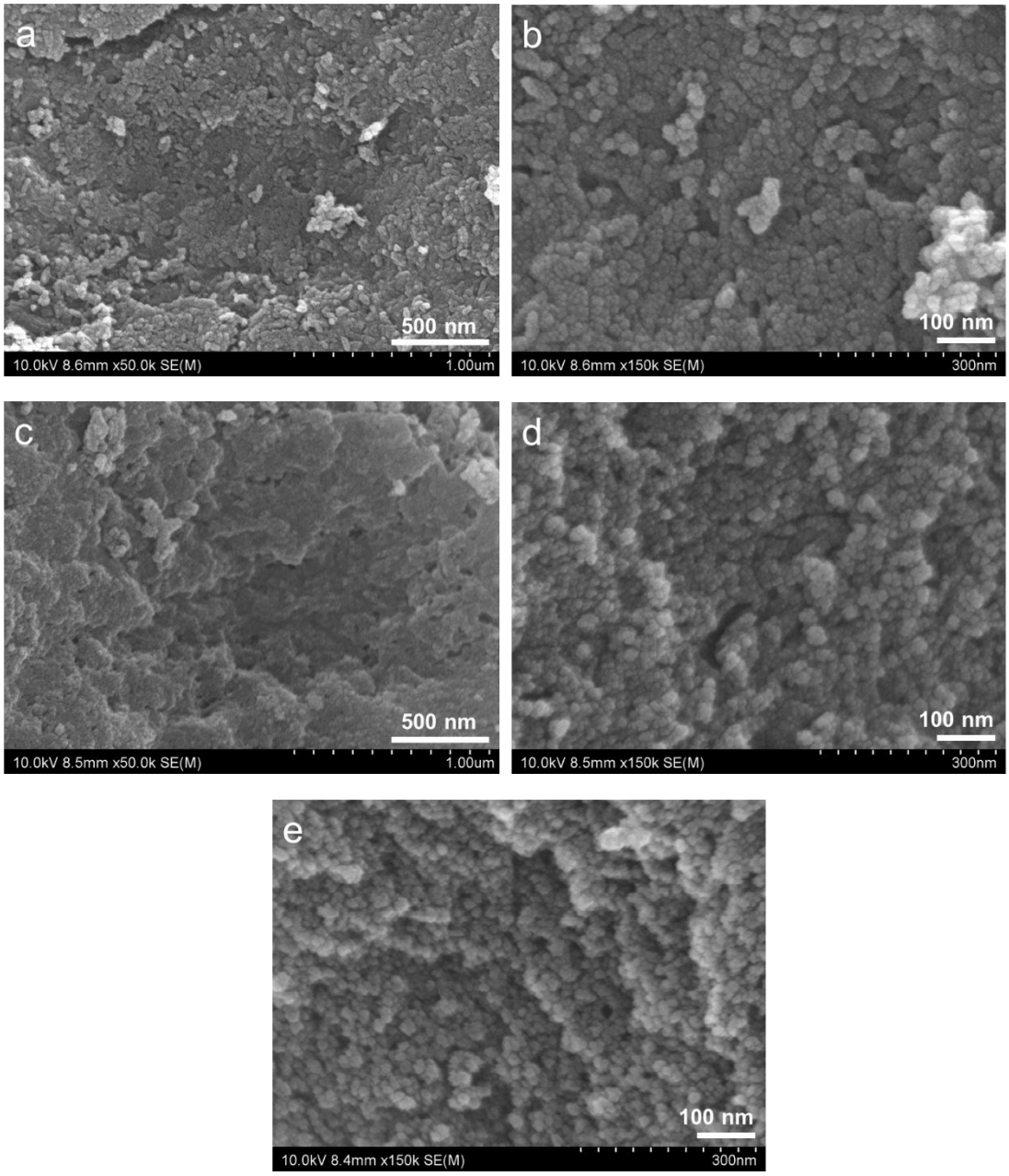

Figure 2-6. SEM images of (a) and (b)pristine NH_2-MIL-53 with low and high magnifications, respectively, (c)Pd/NH_2-MIL-53, (d)Pd@NH_2-MIL-53_0.8, and (e)Pd@NH_2-MIL-53_2.1.

N_2 adsorption isotherms of NH_2-MIL-53, Pd/NH_2-MIL-53 and Pd@NH_2-MIL-53 as well as MIL-53 and Pd/MIL-53 at 77 K are provided in **Figure 2-7**. The specific surface areas of the samples estimated from the N_2 adsorption isotherms are listed in **Table 2-2**. A sharp increase of the adsorption amount was observed at very low P/P_0 for pristine MIL-53 and NH_2-MIL-53, indicating the presence of well-developed micropores in the MOFs.[39–41] The specific surface areas

of the pristine MIL-53 and NH_2-MIL-53 were 1042 and 401 $m^2\ g^{-1}$, respectively, where the former was in good agreement with the value in the published paper.[32] Despite of high crystallinity of NH_2-MIL-53 confirmed by PXRD (**Figure 2-4**), it had rather low specific surface area comparing with MIL-53. This might be due to the presence of carbon residue inside the pores, which was formed during the thermal treatment to remove DMF, blocking the pores. The presence of such carbon residue was confirmed from the results of chemical elemental analysis (**Table 2-3**).

After the Pd introduction by the impregnation method, the surface areas were significantly decreased for both MIL-53 and NH_2-MIL-53, which was due to the collapse of the framework structure (**Table 2-2**). In contrast, it should be noted that the decrease of the adsorption amount at very low P/P_0 and of the surface areas was not so significant for Pd@NH_2-MIL-53.

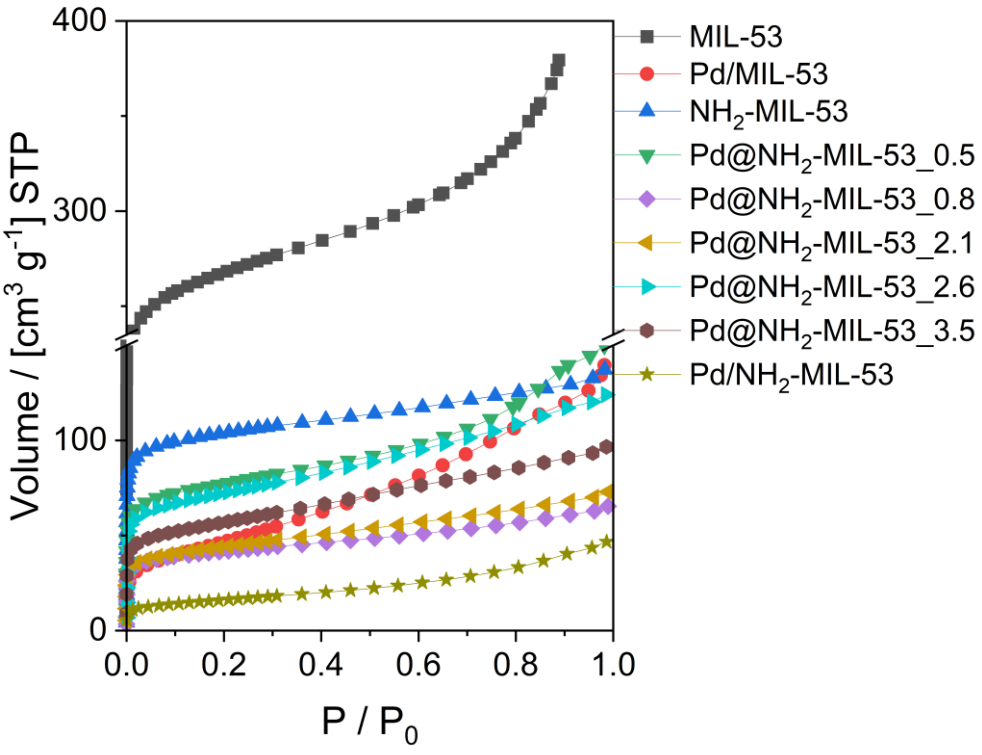

Figure 2-7. N_2 adsorption isotherms of MOFs and MOF-based catalysts.

Table 2-2. Surface areas for pristine MOFs and Pd-loaded ones.

Sample	Surface area ($m^2\ g^{-1}$)
MIL-53	1042
NH_2-MIL-53	401
Pd/MIL-53	164
Pd/NH_2-MIL-53	56
Pd@NH_2-MIL-53_0.5	289
Pd@NH_2-MIL-53_0.8	154
Pd@NH_2-MIL-53_2.1	161
Pd@NH_2-MIL-53_2.6	263
Pd@NH_2-MIL-53_3.5	205

Table 2-3. Compositions of NH_2-MIL-53 at each step of the synthesis determined by elemental analysis.

Sample	Observed value (wt.%)			Atomic ratio
	C	H	N	N/C
As-synthesized NH_2-MIL-53	41.7	2.82	6.41	0.132
NH_2-MIL-53(after DMF exchange)	39.46	3.24	7.07	0.154
NH_2-MIL-53(after DMF and heat treatment)	32.22	2.58	4.45	0.118

Based on these results, it was concluded that the equilibrium adsorption method provided a good way capable to introduce Pd NPs to NH_2-MIL-53 with keeping the framework structure of the MOF.

Figure 2-8 shows TEM images of Pd@NH_2-MIL-53 with different Pd loadings. It was clearly observed that the Pd nanoparticles were uniformly dispersed on Pd@NH_2-MIL-53, and bulky aggregate was not found even with high Pd loadings. The sizes of the Pd NPs were distributed in the range from 0.6 to 4 nm with ca. 2 nm on average, regardless of the Pd loadings (**Table 2-4**). In contrast, Pd/MIL-53 and Pd/NH_2-MIL-53 prepared by the impregnation method displayed larger particle size in the range of 0.8–14 nm (**Figure 2-9**), where some Pd particles were aggregated, forming large particles. These results demonstrated that applying NH_2-MIL-53 as a support material and using the equilibrium adsorption method can give uniform Pd NPs even for high Pd loadings.

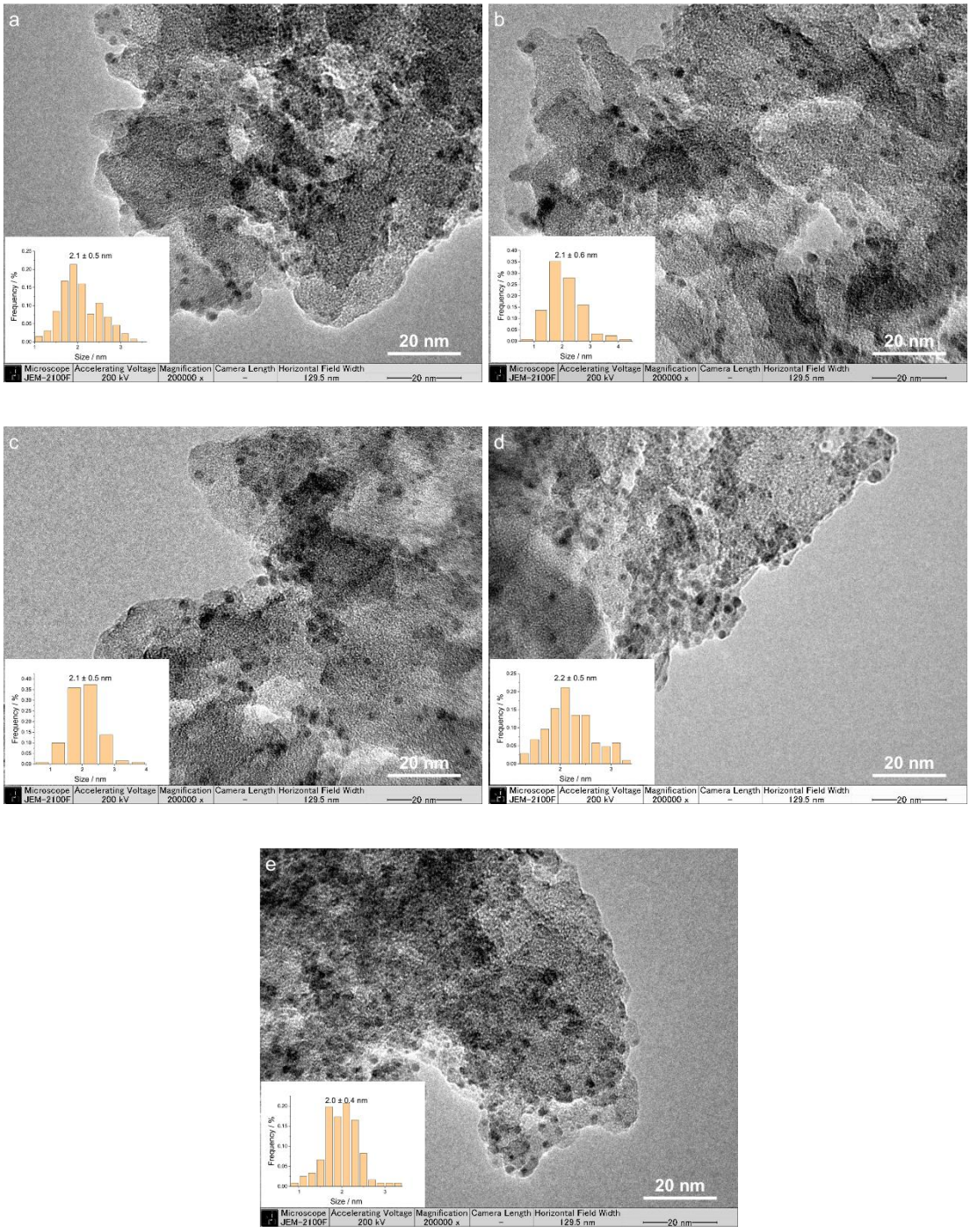

Figure 2-8. TEM images of (a)Pd@NH_2-MIL-53_0.5, (b)Pd@NH_2-MIL-53_0.8, (c)Pd@NH_2-MIL-53_2.1, (d)Pd@NH_2-MIL-53_2.6, and (e)Pd@NH_2-MIL-53_3.5.

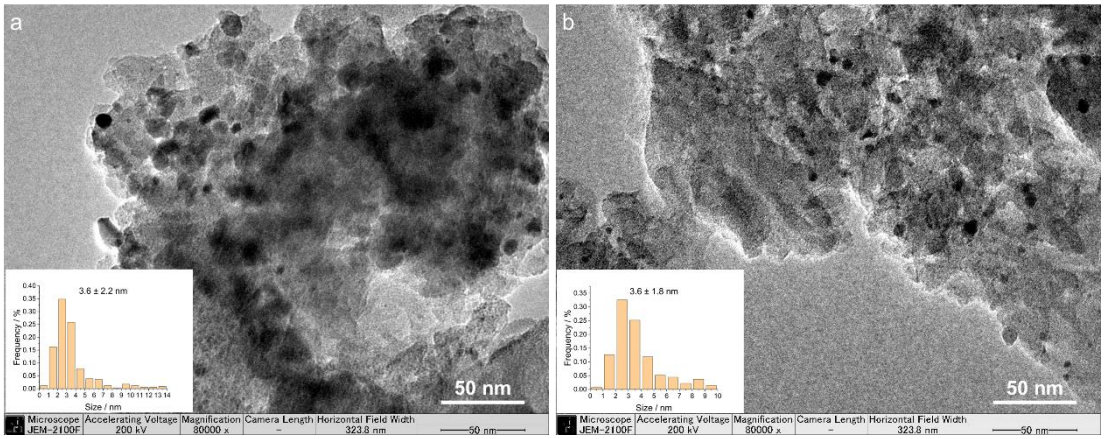

Figure 2-9. TEM images for and particle size distributions of Pd NPs in (a)Pd/MIL-53 and (b)Pd/NH_2-MIL-53.

To investigate the difference in electronic state and structure of the surface of Pd NPs, IR spectra of CO adsorbed on the Pd-introduced MOFs were taken. **Figure 2-10** shows the IR spectra of CO for Pd@NH_2-MIL-53 with different Pd loadings, where the spectra were taken after CO adsorption and subsequent N_2 purge at 25 °C. Despite even after such treatment, two weak bands at around 2170 and 2120 cm^{-1} attributed to gas phase CO was still present. While the IR spectrum of CO for Pd@NH_2-MIL-53_0.5 was weak and a little noisy because of small number of the Pd sites, a broad band dividable to two peaks centered at 2090 and 2070 cm^{-1}, and another broad one at around 1935 cm^{-1} were observed (**Figure 2-11**). In a previous paper by Szanyi and Kwak,[42] linear a-top CO adsorbed on Pd(111) and Pd(100) gave absorption bands at 2095–2099 and 2082 cm^{-1}, respectively, and the bands assignable to bridge-bounded CO on Pd(100) and Pd(111) were observed at 1970~1990 and 1939~1948 cm^{-1}, respectively. Similarly, Murata et al. assigned the band at approximately 2075 cm^{-1} to linear CO adsorbed on a corner site of Pd NPs and on Pd(111), and they also pointed out not to be able to distinguish between the two only from the band position.[43] In case of Pd@NH_2-MIL-53_0.5, all absorption bands appeared at the positions similar to those report by Szanyi and Kwak,[42] while slightly shifted towards low wavenumbers. Such shift was caused by the change in electronic state of Pd sites, which is presumably due to strong interaction between the amino group and Pd NPs in Pd@NH_2-MIL-53_0.5. Anyway, according to the assignment by Szanyi and Kwak,[42] in this study, the absorption bands of 2090, 2070 and ca. 1932 cm^{-1} for Pd@NH_2-MIL-53_0.5 were assigned to linear a-top CO on Pd(111) and Pd(100), and bridge-bound CO on Pd(111), respectively.

Pd@NH_2-MIL-53_0.5 and Pd@NH_2-MIL-53_0.8 showed similar IR spectra, indicating that the crystal facets and electronic state of Pd NPs in the two catalysts were basically identical. With

increase in the Pd loading to 2.1 wt.%, the absorption band at 2090 cm^{-1} became weak, being only a shoulder, and instead the band at 2070 cm^{-1} did dominant. In addition, intensity of the band centered at 1932 cm^{-1} was decreased, and that at 1904 cm^{-1}, which was assignable to the three-fold hollow bound CO on Pd(111),[42–47] appeared. It should be noted that further increase in the Pd loadings, namely 2.6 and 3.5 wt.% Pd loadings, such characteristics was more noticeable and the absorption band at 2090 cm^{-1} almost disappeared. The change in the IR spectra associated with the increase in the Pd loadings suggested that Pd(100) facets became dominate for high Pd loading catalysts. The reason why exposure of Pd(100) facet was preferred in Pd@NH_2-MIL-53 with high Pd loadings may relate to kinetics for the formation of Pd NPs and thermodynamic stability of each facet of Pd NPs. Since Pd atoms are more densely packed on Pd(111) than on Pd(100), the former facet is thermodynamically more stable than the latter one. Thus, the thermodynamically stable Pd NPs enclosed by Pd(111) facets preferentially formed over those by Pd(100) ones for Pd@NH_2-MIL-53 with low Pd loadings, implying slow particle growth. In contrast, in Pd@NH_2-MIL-53 with high Pd loadings, a large amount of the Pd precursors, $(PdCl_3)^-$, was present in the MOF and reduced by $NaBH_4$ to generate many Pd^0 atoms at once, leading to high concentration of Pd^0 atoms on NH_2-MIL-53. Such situation might facilitate the rapid formation of Pd NPs, resulting in thermodynamically less stable Pd NPs exposing Pd(100) facet.

Some parameters such as reaction time, capping agents and precursor concentration must affect the nucleation and growth process in colloids formation.[48,49] It is well-known that halide ions act as capping agents for Pd nanocrystals and the morphology of nanocrystals are changed depending on their presence or absence and concetration.[49,50] For example, bromine ion (Br^-) selectively adsorb onto the (100) facets of Pd particle during its growth, and thus Pd nanocubes enclosed by (100) facets were formed in the presence of Br^-.[49,51,52] It is also demonstrated that Pd nanocubes formation is promoted in the presence of chloride ion,[53,54] where dominant Pd(100) facets are favored with higher Cl^- concentration.[54] In this study, chloride ion (Cl^-) was generated in the solution upon the reduction of the Pd precursor by $NaBH_4$ and might act as capping agent for Pd NPs. Since the ratio of Cl^- to Pd was almost constant regardless of the Pd loadings as mentioned before, the capping effect of Cl^- to Pd NPs was probably about the same regardless of the Pd loadings. Thus, it is likely that Pd NPs with almost the same size were formed in Pd@NH_2-MIL-53 with different Pd loadings.

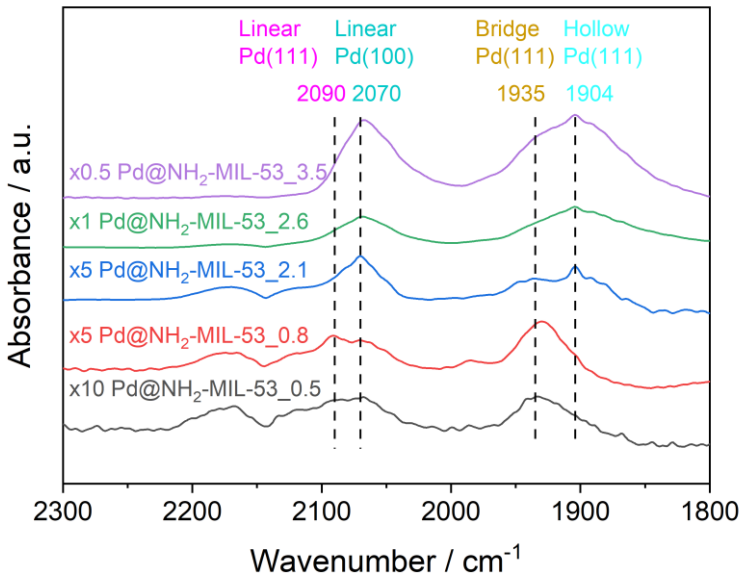

Figure 2-10. IR spectra of CO adsorbed on Pd@NH_2-MIL-53 with different Pd loadings taken at 25 °C.

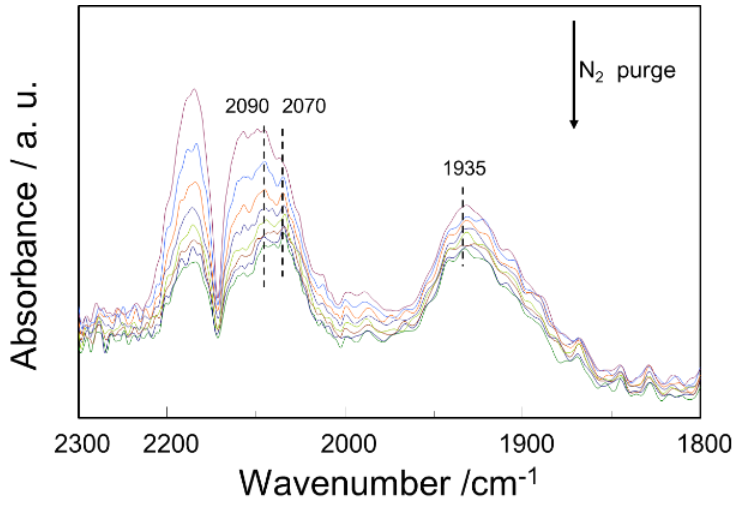

Figure 2-11. Series of IR spectra obtained during N_2 purge to remove gas phase and weakly adsorbed CO for Pd@NH_2-MIL-53_0.5. The spectra were taken at 25 °C.

We also measured IR spectra of CO adsorbed on Pd/NH_2-MIL-53 and Pd/MIL-53 (**Figure 2-12**). The IR spectrum of CO adsorbed on Pd/NH_2-MIL-53 was similar to that on Pd@NH_2-MIL-53_2.6 where two main bands corresponding to linear a-top CO on Pd(100) at 2070 cm^{-1} and three-fold hollow bound CO on Pd(111) at 1904 cm^{-1} were observed. Differently, Pd/MIL-53

exhibited absorption bands of linear a-top CO and bridge-bound CO on Pd(111) at 2077 and 1941 cm^{-1}, respectively, which located at a little higher wavenumbers compared to those for Pd@NH_2-MIL-53. Such difference in the band positions between Pd/MIL-53 and Pd@NH_2-MIL-53 also suggested the difference in the electronic state of Pd NPs,[55,56] and that the electronic state of Pd NPs in Pd@NH_2-MIL-53 was more negative than that in Pd/MIL-53, which might be caused by the interaction between amino group and Pd NPs in Pd@NH_2-MIL-53, leading to the electron transfer from amino group to Pd NPs.

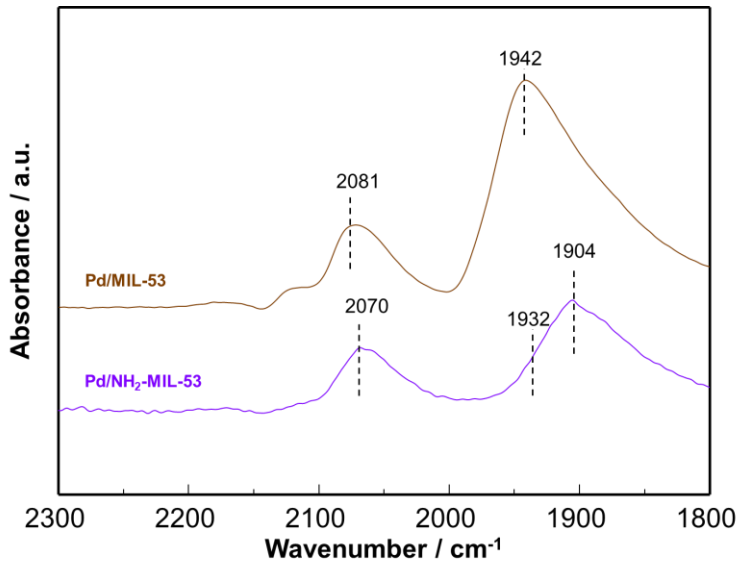

Figure 2-12. IR spectra of CO adsorbed on Pd/NH_2-MIL-53 and Pd/MIL-53 taken at 25 °C.

3.2 Catalytic performance

The catalytic performances of Pd@MOFs were evaluated with the reduction of NO_2^- in water. **Figure 2-13** shows time dependence of NO_2^- conversion over Pd@NH_2-MIL-53 with different Pd loadings. The catalytic activity was significantly changed depending on the Pd loadings and Pd@NH_2-MIL-53 with high Pd loadings were highly active, which was firstly due to the large number of Pd sites exposed on the surface. In fact, almost 100 % NO_2^- conversion was achieved at 4 h for Pd@NH_2-MIL-53_2.1, _2.6, and _3.5. In contrast to the catalytic activity, all Pd@NH_2-MIL-53 exhibited similar selectivity and almost no NH_4^+ was formed whole the reaction time regardless of the Pd loadings. That is, only the difference in the activity between the catalysts with different Pd loadings should be considered.

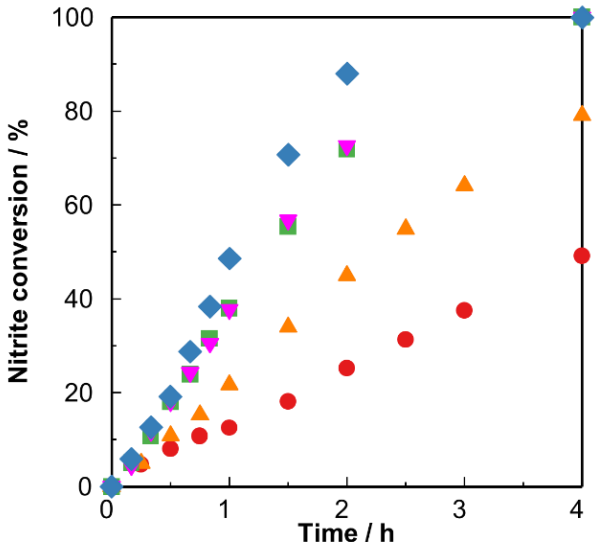

Figure 2-13. Time dependences of NO_2^- conversion for reduction of NO_2^- in water over Pd@NH_2-MIL-53 with different Pd loadings. (●)Pd@NH_2-MIL-53_0.5, (▲)Pd@NH_2-MIL-53_0.8, (■)Pd@NH_2-MIL-53_2.1, (▼)Pd@NH_2-MIL-53_2.6, and (♦)Pd@NH_2-MIL-53_3.5. Reaction conditions: catalyst weight, 20 mg; $[NO_2^-]_0$, 6.67 mmol L^{-1}; H_2 flow rate, 50 mL min^{-1}; and temperature, 25 °C.

To quantitively evaluate the catalytic performances, the catalytic reaction data below 20% conversion were analyzed using a pseudo-first-order reaction rate equation (**Figure 2-14**), giving rate constants (k_{obs}) and those are listed in **Table 2-4**. This table also includes specific activity per surface Pd sites (k_s) as well as average sizes and dispersions of Pd NPs. To estimate k_s, it was assumed that the shape of Pd NPs was spheric,[33–35] and used the average size of Pd NPs (d) and

the actual Pd loading obtained by TEM and ICP-AES, respectively. It is noted that k_s were changed depending on the Pd loadings, though the average sizes of Pd NPs were almost the same for all Pd@NH_2-MIL-53. The catalysts with low Pd loadings like Pd@NH_2-MIL-53_0.5 and _0.8 had large k_s, which were about 2.5 times as large as those for Pd@NH_2-MIL-53 with high Pd loadings. These results suggested that the structure and electronic state of the surface of Pd NPs also dominated the catalytic activity in addition to the number of Pd sites exposed on the surface.

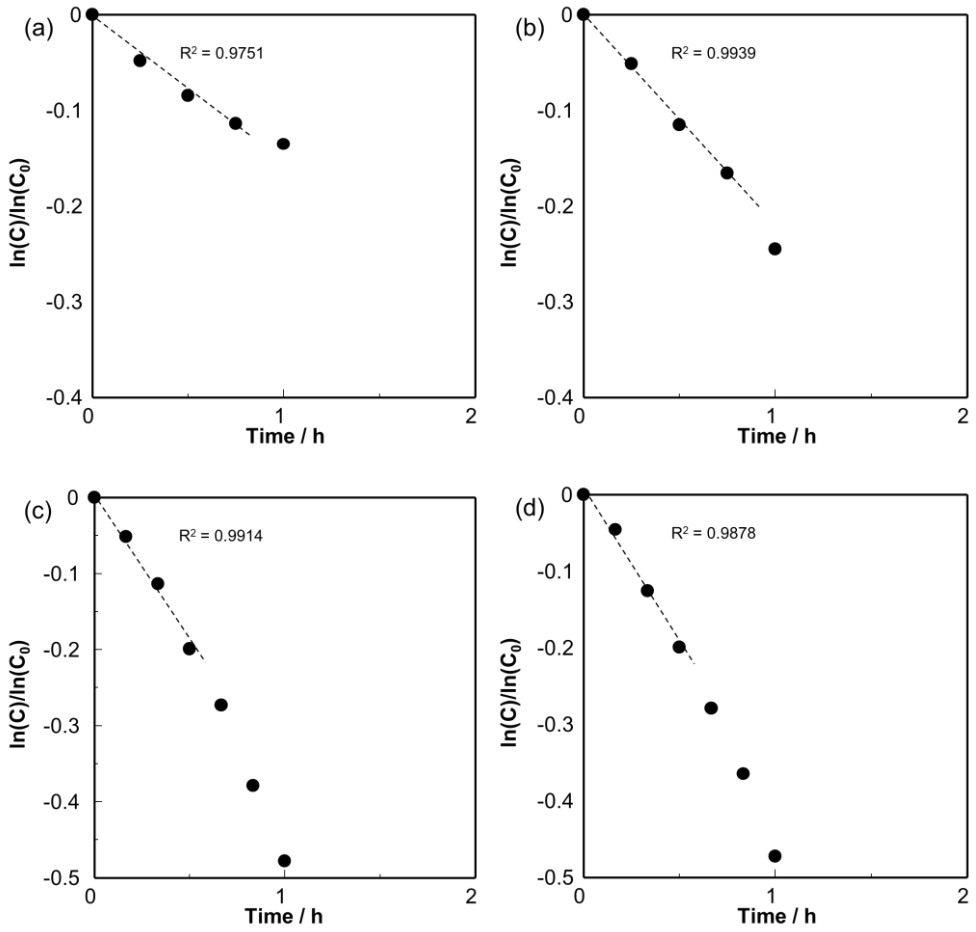

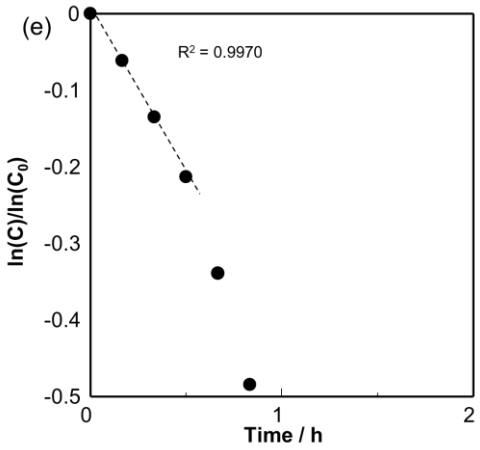

Figure 2-14. Plots of natural logarithm of nitrite concentration *versus* time for nitrite reduction. (a)Pd@NH_2-MIL-53_0.5, (b)Pd@NH_2-MIL-53_0.8, (c)Pd@NH_2-MIL-53_2.1, (d)Pd@NH_2-MIL-53_2.6 and (e)Pd@NH_2-MIL-53_3.5.

Table 2-4. Particle size and dispersion of Pd NPs in Pd@NH_2-MIL-53, and the catalytic performances (k_{obs} and k_s) for the reduction of NO_2^- in water.

Catalyst	d (nm)	D (%)	k_{obs} (h^{-1})	k_s ($mol_{nitrite}\ mol_{surface\ Pd}^{-1}\ h^{-1}$)
Pd@NH_2-MIL-53_0.5	2.1	53	0.13	2.9×10^2
Pd@NH_2-MIL-53_0.8	2.1	53	0.24	3.0×10^2
Pd@NH_2-MIL-53_2.1	2.1	53	0.42	1.7×10^2
Pd@NH_2-MIL-53_2.6	2.2	51	0.41	1.3×10^2
Pd@NH_2-MIL-53_3.5	1.9	59	0.50	1.2×10^2
Pd/MIL-53	3.6	31	0.49	1.7×10^2
Pd/NH_2-MIL-53	3.6	31	0.33	1.8×10^2

The Pd 3d XPS spectra of typical Pd@NH_2-MIL-53 with low and high Pd loadings are shown in **Figure 2-15**. Both samples showed a Pd $3d_{5/2}$ peak at ca. 335.5 eV with a shoulder peak at ca. 337.5 eV, which correspond to metallic Pd^0 and Pd^{2+}, respectively.[55,57,58] The presence of oxidized species was due to the exposure of the samples to air when setting the samples to the XPS measurement. There was no significant difference in the XPS spectra between Pd@NH_2-MIL-53 with low and high Pd loadings, demonstrating that the electronic state of the surface of Pd NPs were basically identical regardless of the Pd loadings. Therefore, it is more plausible that the difference in the structure of Pd NPs dominated the specific catalytic activity of Pd NPs on Pd@NH_2-MIL-53.

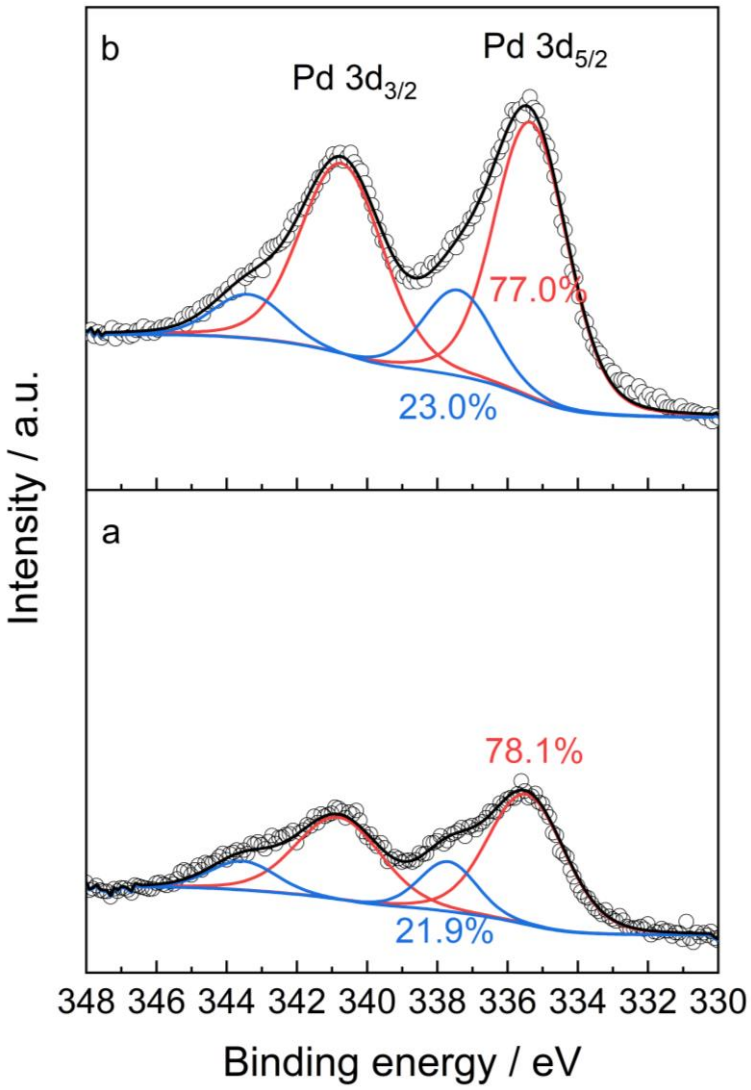

Figure 2-15. Pd 3d XPS spectra of (a)Pd@NH_2-MIL-53_0.5 and (b) Pd@NH_2-MIL-53_3.5.

To gain insight into the reason why the difference in the Pd loadings made that in the specific catalytic activity per Pd sites (k_s), the absorption bands of CO adsorbed on Pd@NH_2-MIL-53 were deconvoluted using a Gaussian function and the absorption band areas of 1904, 1932, 2070, and 2090 cm^{-1} were calculated to estimate the fraction of each band area for Pd@NH_2-MIL-53 (**Table 2-5**) to investigate the correlation between those and k_s. After several trials, it was found that k_s were well correlated with the fraction of the band areas due to CO on Pd(111) facets (i.e. the sum of fractions of the band areas at 2090 and 1932 cm^{-1}) as shown in **Figure 2-16**. This correlation suggested that the Pd(111) facets on Pd@NH_2-MIL-53 gave highly active Pd sites for the reduction of NO_2^-. From the y-intercept and slope of the straight line in **Figure 2-16**, it was estimated that the specific activity of the active sites on Pd(111) facet was about 6 times higher

than that on the others, if absorption coefficients were the same. The reason for it is still not well understood, but low adsorption energy of a reaction intermediate may lead to the high specific activity of the Pd sites on Pd(111) facet. In previous studies, it was suggested that the adsorption of NO_2^- on Pd particles was energetically favored and adsorbed NO_2^- was easily converted to NO, while formed NO was quite stable on the surface.[59–61] Moreover, it was suggested by DFT calculation that the rate constant for the reduction of NO_2^- was much larger than that of NO, and the adsorption of NO was much stronger than that of NO_2^- or H_2, suggesting that the adsorbed NO was stable and thus the reduction of NO was a rate-limiting step in the reduction of NO_2^-, leading to the accumulation of NO on the surface. While there was no significant difference in the adsorption energy for NO_2^- on different Pd facets, the adsorption of NO was much stronger on Pd(100) facet than on other ones including Pd(111) one.[61] Thus, it is deduced that the strong adsorption of intermediate NO on Pd(100) hindered the further reduction of NO, while the weaker adsorption of NO on Pd(111) rendered the higher reaction activity exhibited on Pd(111).

Table 2-5. The fractions of the IR band area of different adsorbed CO species on Pd catalysts.

Catalyst	Linear a-top CO on Pd(111) (ca. 2090 cm^{-1})	Linear a-top CO on Pd(100) (ca. 2070 cm^{-1})	Bridge bound CO on Pd(111) (ca. 1932 cm^{-1})	Hollow CO on Pd(111) (ca. 1904 cm^{-1})
Pd@NH_2-MIL-53_0.5	0.18	0.29	0.41	0.06
Pd@NH_2-MIL-53_0.8	0.13	0.25	0.50	0.00
Pd@NH_2-MIL-53_2.1	0.14	0.22	0.11	0.40
Pd@NH_2-MIL-53_2.6	0.00	0.37	0.16	0.47
Pd@NH_2-MIL-53_3.5	0.00	0.32	0.16	0.46
Pd/MIL-53	0.00	0.24	0.11	0.57
Pd/NH_2-MIL-53	0.00	0.13	0.49	0.32

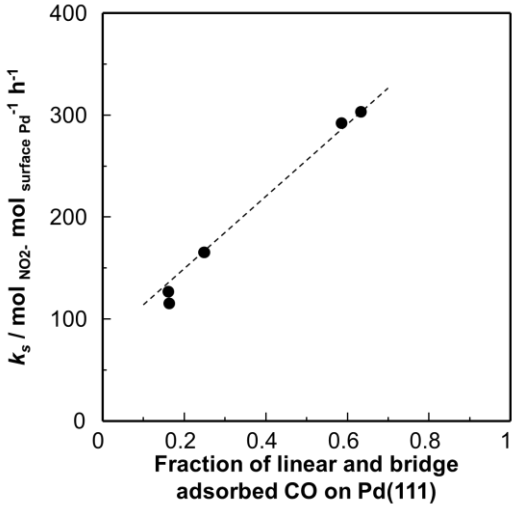

Figure 2-16. Plot of k_s against the fraction of the band areas due to linear and bridge adsorbed CO on Pd(111).

Pd/NH_2-MIL-53 showed similar specific activity (k_s) to Pd@NH_2-MIL-53_2.1 but did lower than those of the low Pd loadings Pd@NH_2-MIL-53 (0.5 and 0.8 wt. % Pd). This was resulted from the lower fraction of Pd(111) facets for Pd/NH_2-MIL-53. Despite of the higher fraction of Pd(111) facets for Pd/MIL-53 compared with Pd/NH_2-MIL-53, it showed only similar specific activity (k_s) to Pd/NH_2-MIL-53. The reason for this might be that the electron density of Pd NPs in Pd/NH_2-MIL-53 was higher than that in Pd/MIL-53, as suggested by the band shift shown in IR spectra of adsorbed CO. The higher electron density of Pd NPs in Pd/NH_2-MIL-53 promoted the NO_2^- reduction much more, thus Pd/NH_2-MIL-53 exhibited similar k_s to Pd/MIL-53, despite the fraction of Pd(111) facets in Pd/ NH_2-MIL-53 was lower than that of Pd/MIL-53.

4. Conclusions

MIL-53 and NH_2-MIL-53 were applied as a support for introducing Pd particles and the catalytic performance of the resulting catalysts were evaluated with NO_2^- reduction in water. The amino group in NH_2-MIL-53 played a critical role in introducing Pd, and Pd nanoparticles were successfully introduced into NH_2-MIL-53 but it was failed for MIL-53 by the equilibrium adsorption method. $(PdCl_3)^-$, which was a precursor for the Pd nanoparticle, in the acidic $PdCl_2$ solution was electrostatically interacted with the protonated amino group in NH_2-MIL-53 to give $-NH_3^+$---$(PdCl_3)^-$ ion pair, resulting in the successful introduction of Pd. The combination of using NH_2-MIL-53 and the equilibrium adsorption method is a good way to facilitate uniform dispersion of Pd nanoparticles with high Pd loadings. Pd@NH_2-MIL-53 with different Pd loadings prepared

by this method exhibited different Pd surface structures, where a linear relation between specific activity per surface Pd site and the fraction of Pd(111) facet was observed. These Pd(111) facets on Pd@NH_2-MIL-53 exhibited high activity for NO_2^- reduction in water.

5. References

(1) Zhou, H. C.; Long, J. R.; Yaghi, O. M. Introduction to Metal-Organic Frameworks. *Chem. Rev.* **2012**, *112* (2), 673–674. https://doi.org/10.1021/cr300014x.

(2) Zhou, H. C.; Kitagawa, S. Metal-Organic Frameworks (MOFs). *Chem. Soc. Rev.* **2014**, *43*, 5415–5418. https://doi.org/10.1039/C4CS90059F.

(3) Fujita, M.; Jung Kwon, Y.; Washizu, S.; Ogura, K. Preparation, Clathration Ability, and Catalysis of a Two-Dimensional Square Network Material Composed of Cadmium(II) and 4,4'-Bipyridine. *J. Am. Chem. Soc*. **1994**, *116* (3), 1151-1152. https://doi.org/10.1021/ja00082a055.

(4) Hasegawa, S.; Horike, S.; Matsuda, R.; Furukawa, S.; Mochizuki, K.; Kinoshita, Y.; Kitagawa, S. Three-Dimensional Porous Coordination Polymer Functionalized with Amide Groups Based on Tridentate Ligand: Selective Sorption and Catalysis. *J. Am. Chem. Soc*. **2007**, *129* (9), 2607–2614. https://doi.org/10.1021/ja067374y.

(5) Dhakshinamoorthy, A.; Alvaro, M.; Garcia, H. Commercial Metal-Organic Frameworks as Heterogeneous Catalysts. *Chem. Commun.* **2012**, *48* (92), 11275–11288. https://doi.org/10.1039/C2CC34329K.

(6) Hu, Z.; Zhao, D. Metal-Organic Frameworks with Lewis Acidity: Synthesis, Characterization, and Catalytic Applications. *Cryst. Eng. Comm*. **2017**, *19* (29), 4066–4081. https://doi.org/10.1039/C6CE02660E.

(7) Liu, L.; Song, Y.; Chong, H.; Yang, S.; Xiang, J.; Jin, K.; Kang, X.; Zhang, J.; Yu, H.; Zhu, M. Size-Confined Growth of Atom-Precise Nanoclusters in Metal-Organic Frameworks and Their Catalytic Applications. *Nanoscale*, **2016**, *8* (3), 1407–1412. https://doi.org/10.1039/C5NR06930K.

(8) An, B.; Zhang, J.; Cheng, K.; Ji, P.; Wang, C.; Lin, W. Confinement of Ultrasmall Cu/ZnO_x Nanoparticles in Metal–Organic Frameworks for Selective Methanol Synthesis from Catalytic Hydrogenation of CO_2. *J. Am. Chem. Soc*. **2017**, *139* (10), 3834–3840. https://doi.org/10.1021/jacs.7b00058.

(9) Ji, S.; Chen, Y.; Zhao, S.; Chen, W.; Shi, L.; Wang, Y.; Dong, J.; Li, Z.; Li, F.; Chen, C.; Peng, Q.; Li, J.; Wang, D.; Li, Y. Atomically Dispersed Ruthenium Species Inside Metal–Organic Frameworks: Combining the High Activity of Atomic Sites and the Molecular Sieving Effect of MOFs. *Angew. Chem. Int. Ed.* **2019**, *58*, 4271-4275. https://doi.org/10.1002/anie.201814182.

(10) Kollmannsberger, K. L.; Kronthaler, L.; Jinschek, J. R.; Fischer, R. A. Defined Metal Atom Aggregates Precisely Incorporated into Metal-Organic Frameworks. *Chem. Soc. Rev*. **2022**, *51* (24), 9933–9959. https://doi.org/10.1039/D1CS00992C.

(11) Ma, X.; Pu, C.; Zhang, Y.; Chang, G.; Tian, G.; Wu, S.; Liu, J.; Hu, Z.; Wang, L.; Yin, Y.; Janiak, C.; Yang, X. Confined Pd Clusters with Dynamic Structure for Highly Efficient Cascade-Type Catalysis.

Chem. Eng. J. **2022**, *429*, 132128. https://doi.org/10.1016/j.cej.2021.132128.

(12) Li, X.; Goh, T. W.; Li, L.; Xiao, C.; Guo, Z.; Zeng, X. C.; Huang, W. Controlling Catalytic Properties of Pd Nanoclusters through Their Chemical Environment at the Atomic Level Using Isoreticular Metal-Organic Frameworks. *ACS Catal.* **2016**, *6* (6), 3461–3468. https://doi.org/10.1021/acscatal.6b00397.

(13) Chen, Y. Z.; Wang, Z. U.; Wang, H.; Lu, J.; Yu, S. H.; Jiang, H. L. Singlet Oxygen-Engaged Selective Photo-Oxidation over Pt Nanocrystals/Porphyrinic MOF: The Roles of Photothermal Effect and Pt Electronic State. *J. Am. Chem. Soc.* **2017**, *139* (5), 2035–2044. https://doi.org/10.1021/jacs.6b12074.

(14) Meilikhov, M.; Yusenko, K.; Esken, D.; Turner, S.; Van Tendeloo, G.; Fischer, R. A. Metals@MOFs-Loading MOFs with Metal Nanoparticles for Hybrid Functions. *Eur. J. Inorg. Chem.* **2010**, *24*, 3701–3714. https://doi.org/10.1002/ejic.201000473.

(15) Moon, H. R.; Lim, D. W.; Suh, M. P. Fabrication of Metal Nanoparticles in Metal-Organic Frameworks. *Chem. Soc. Rev.* **2013**, *42*, 1807–1824. https://doi.org/10.1039/c2cs35320b.

(16) Yang, Q.; Xu, Q.; Jiang, H. L. Metal-Organic Frameworks Meet Metal Nanoparticles: Synergistic Effect for Enhanced Catalysis. *Chem. Soc. Rev*. **2017**, *46*, 4774–4808. https://doi.org/10.1039/c6cs00724d.

(17) Wang, Q.; Astruc, D. State of the Art and Prospects in Metal-Organic Framework (MOF)-Based and MOF-Derived Nanocatalysis. *Chem. Rev.* **2020**, *120* (2), 1438–1511. https://doi.org/10.1021/acs.chemrev.9b00223.

(18) Choi, K. M.; Na, K.; Somorjai, G. A.; Yaghi, O. M. Chemical Environment Control and Enhanced Catalytic Performance of Platinum Nanoparticles Embedded in Nanocrystalline Metal-Organic Frameworks. *J. Am. Chem. Soc.* **2015**, *137* (24), 7810–7816. https://doi.org/10.1021/jacs.5b03540.

(19) Dhakshinamoorthy, A.; Asiri, A. M.; Garcia, H. Catalysis by Metal-Organic Frameworks in Water. *Chem. Commun.* **2014**, *50* (85), 12800–12814. https://doi.org/10.1039/c4cc04387a.

(20) Wang, C.; Liu, X.; Keser Demir, N.; Chen, J. P.; Li, K. Applications of Water Stable Metal-Organic Frameworks. *Chem. Soc. Rev.* **2016**, *45*, 5107–5134. https://doi.org/10.1039/c6cs00362a.

(21) Loiseau, T.; Serre, C.; Huguenard, C.; Fink, G.; Taulelle, F.; Henry, M.; Bataille, T.; Férey, G. A Rationale for the Large Breathing of the Porous Aluminum Terephthalate (MIL-53) Upon Hydration. *Chem. Eur. J.* **2004**, *10* (6), 1373–1382. https://doi.org/10.1002/chem.200305413.

(22) Ahnfeldt, T.; Gunzelmann, D.; Loiseau, T.; Hirsemann, D.; Senker, J.; Férey, G.; Stock, N. Synthesis and Modification of a Functionalized 3D Open-Framework Structure with MIL-53 Topology. *Inorg. Chem*. **2009**, *48* (7), 3057-3064. https://doi.org/10.1021/ic8023265.

(23) Prüsse, U.; Hähnlein, M.; Daum, J.; Vorlop, K.-D. Improving the Catalytic Nitrate Reduction. *Catal. Today* **2000**, *55* (1-2), 79-90. https://doi.org/10.1016/S0920-5861(99)00228-X.

(24) Zhang, R.; Shuai, D.; Guy, K. A.; Shapley, J. R.; Strathmann, T. J.; Werth, C. J. Elucidation of Nitrate

Reduction Mechanisms on a Pd-In Bimetallic Catalyst Using Isotope Labeled Nitrogen Species. *ChemCatChem* **2013**, *5* (1), 313–321. https://doi.org/10.1002/cctc.201200457.

(25) Hirayama, J.; Kamiya, Y. Tin-Palladium Supported on Alumina as a Highly Active and Selective Catalyst for Hydrogenation of Nitrate in Actual Groundwater Polluted with Nitrate. *Catal. Sci. Technol.* **2018**, *8* (19), 4985–4993. https://doi.org/10.1039/c8cy00730f.

(26) Deganello, F.; Liotta, L. F.; Macaluso, A.; Venezia, A. M.; Deganello, G. Catalytic Reduction of Nitrates and Nitrites in Water Solution on Pumice-Supported Pd-Cu Catalysts. *Appl. Catal. B* **2000**, *24*, 265-273. https://doi.org/10.1016/S0926-3373(99)00109-5.

(27) Chollier-Brym, M. J.; Gavagnin, R.; Strukul, G.; Marella, M.; Tomaselli, M.; Ruiz, P. New Insight in the Solid State Characteristics, in the Possible Intermediates and on the Reactivity of Pd-Cu and Pd-Sn Catalysts, Used in Denitratation of Drinking Water. *Catal. Today* **2002**, *75* (1-4), 49-55. https://doi.org/10.1016/S0920-5861(02)00043-3.

(28) Yoshinaga, Y.; Akita, T.; Mikami, I.; Okuhara, T. Hydrogenation of Nitrate in Water to Nitrogen over Pd-Cu Supported on Active Carbon. *J. Catal.* **2002**, *207* (1), 37–45. https://doi.org/10.1006/jcat.2002.3529.

(29) Pintar, A.; Batista, J.; Muševič, I. Palladium-Copper and Palladium-Tin Catalysts in the Liquid Phase Nitrate Hydrogenation in a Batch-Recycle Reactor. *Appl. Catal. B* **2004**, *52* (1), 49–60. https://doi.org/10.1016/j.apcatb.2004.02.019.

(30) Marchesini, F. A.; Gutierrez, L. B.; Querini, C. A.; Miró, E. E. Pt,In and Pd,In Catalysts for the Hydrogenation of Nitrates and Nitrites in Water. FTIR Characterization and Reaction Studies. *Chem. Eng. J.* **2010**, *159* (1–3), 203–211. https://doi.org/10.1016/j.cej.2010.02.056.

(31) Martínez, J.; Ortiz, A.; Ortiz, I. State-of-the-Art and Perspectives of the Catalytic and Electrocatalytic Reduction of Aqueous Nitrates. *Appl. Catal. B* **2017**, *207*, 42–59. https://doi.org/10.1016/j.apcatb.2017.02.016.

(32) Sánchez-Sánchez, M.; Getachew, N.; Díaz, K.; Díaz-García, M.; Chebude, Y.; Díaz, I. Synthesis of Metal-Organic Frameworks in Water at Room Temperature: Salts as Linker Sources. *Green Chem.* **2015**, *17* (3), 1500–1509. https://doi.org/10.1039/c4gc01861c.

(33) Lear, T.; Marshall, R.; Lopez-Sanchez, J. A.; Jackson, S. D.; Klapötke, T. M.; Bäumer, M.; Rupprechter, G.; Freund, H. J.; Lennon, D. The Application of Infrared Spectroscopy to Probe the Surface Morphology of Alumina-Supported Palladium Catalysts. *J. Chem. Phys.* **2005**, *123* (17). https://doi.org/10.1063/1.2101487.

(34) Li, J.; Chen, W.; Zhao, H.; Zheng, X.; Wu, L.; Pan, H.; Zhu, J.; Chen, Y.; Lu, J. Size-Dependent Catalytic Activity over Carbon-Supported Palladium Nanoparticles in Dehydrogenation of Formic Acid. *J. Catal.* **2017**, *352*, 371–381. https://doi.org/10.1016/j.jcat.2017.06.007.

(35) Zhang, Z.; Lu, J.; Zhang, B.; Shi, W.; Guo, Y.; Cui, F. Insight into the Size Effect of Pd Nanoparticles on the Catalytic Reduction of Nitrite in Water over Pd/C Catalysts. *Environ. Sci. Nano* **2020**, *7* (7), 2117–2129. https://doi.org/10.1039/d0en00417k.

(36) Ruiz, M.; Sastre, A. M.; Guibal, E. Palladium Sorption on Glutaraldehyde-Crosslinked Chitosan. *React. Funct. Polym*. **2000**, 45(3), 155-173. https://doi.org/10.1016/S1381-5148(00)00019-5.

(37) Kang, I. J.; Khan, N. A.; Haque, E.; Jhung, S. H. Chemical and Thermal Stability of Isotypic Metal-Organic Frameworks: Effect of Metal Ions. *Chem. Eur. J.* **2011**, *17* (23), 6437–6442. https://doi.org/10.1002/chem.201100316.

(38) Mahugo, R.; Mayoral, A.; Sánchez-Sánchez, M.; Diaz, I. Observation of Ag Nanoparticles in/on Ag@MIL-100(Fe) Prepared Through Different Procedures. *Front. Chem.* **2019**, *7*. https://doi.org/10.3389/fchem.2019.00686.

(39) Alaerts, L.; Maes, M.; Giebeler, L.; Jacobs, P. A.; Martens, J. A.; Denayer, J. F. M.; Kirschhock, C. E. A.; De Vos, D. E. Selective Adsorption and Separation of Ortho-Substituted Alkylaromatics with the Microporous Aluminum Terephthalate MIL-53. *J. Am. Chem. Soc.* **2008**, *130* (43), 14170–14178. https://doi.org/10.1021/ja802761z.

(40) Cheng, X.; Zhang, A.; Hou, K.; Liu, M.; Wang, Y.; Song, C.; Zhang, G.; Guo, X. Size- and Morphology-Controlled NH_2-MIL-53(Al) Prepared in DMF-Water Mixed Solvents. *Dalton Trans.* **2013**, *42* (37), 13698–13705. https://doi.org/10.1039/c3dt51322j.

(41) Wamba, H. N.; Singh, N.; Dalakoti, S.; Divekar, S.; Arya, A.; Tagne Kuate, A. C.; Ngoune, J.; Dasgupta, S. Al-Based Isoreticular Metal-Organic Frameworks with MIL-53 Topology as Effective Adsorbents in Methane Purification. *ChemistrySelect* **2023**, *8* (4). https://doi.org/10.1002/slct.202204476.

(42) Szanyi, J.; Kwak, J. H. Dissecting the Steps of CO2 Reduction: 2. The Interaction of CO and CO_2 with Pd/γ-Al_2O_3: An in Situ FTIR Study. *Phys. Chem. Chem. Phys.* **2014**, *16* (29), 15126–15138. https://doi.org/10.1039/c4cp00617h.

(43) Murata, K.; Eleeda, E.; Ohyama, J.; Yamamoto, Y.; Arai, S.; Satsuma, A. Identification of Active Sites in CO Oxidation over a Pd/Al_2O_3 Catalyst. *Phys. Chem. Chem. Phys.* **2019**, *21* (33), 18128–18137. https://doi.org/10.1039/c9cp03943k.

(44) Zhang, Z.; Shi, W.; Wang, W.; Xu, Y.; Bao, X.; Zhang, R.; Zhang, B.; Guo, Y.; Cui, F. Interfacial Electronic Effects of Palladium Nanocatalysts on the By-Product Ammonia Selectivity during Nitrite Catalytic Reduction. *Environ. Sci. Nano* **2018**, *5* (2), 338–349. https://doi.org/10.1039/c7en00909g.

(45) Rupprechter, G.; Unterhalt, H.; Morkel, M.; Galletto, P.; Hu, L.; Freund, H. J. Sum frequency generation vibrational spectroscopy at solid-gas interfaces: CO adsorption on Pd model catalysts at ambient pressure. *Surf. Sci*. **2002**, *502-503*, 109-122. https://doi.org/10.1016/S0039-6028(01)01907-0.

(46) Tessier, D.; Rakai, A.; Bozon-Verduraz, F. Spectroscopic Study of the Interaction of Carbon Monoxide with Cationic and Metallic Palladium in Palladium-Alumina Catalysts. *J. Chem. Soc. Faraday Trans*. **1992**, *88* (5), 741-749. https://doi.org/10.1039/FT9928800741.

(47) Skotak, M.; Karpiński, Z.; Juszczyk, W.; Pielaszek, J.; Kępiński, L.; Kazachkin, D. V.; Kovalchuk, V. I.; D'Itri, J. L. Characterization and Catalytic Activity of Differently Pretreated Pd/Al_2O_3 Catalysts: the Role of Acid Sites and of Palladium–Alumina Interactions. *J. Catal*. **2004**, *227* (1), 11–25. https://doi.org/10.1016/j.jcat.2004.06.007.

(48) Tao, A.R.; Habas, S.; Yang, P. Shape Control of Colloidal Metal Nanocrystals. *Small*, **2008**, *4*, 310–325. https://doi.org/10.1002/smll.200701295.

(49) Zhang, H.; Jin, M.; Xiong, Y.; Lim, B.; Xia, Y. Shape-Controlled Synthesis of Pd Nanocrystals and Their Catalytic Applications. *Acc Chem Res*, **2013**, *46* (8), 1783–1794. https://doi.org/10.1021/ar300209w.

(50) Xiong, Y.; Chen, J.; Wiley, B.; Xia, Y.; Aloni, S.; Yin, Y. Understanding the Role of Oxidative Etching in the Polyol Synthesis of Pd Nanoparticles with Uniform Shape and Size. *J. Am. Chem. Soc*. **2005**, *127* (20), 7332–7333. https://doi.org/10.1021/ja0513741.

(51) Xiong, Y.; Cai, H.; Wiley, B. J.; Wang, J.; Kim, M. J.; Xia, Y. Synthesis and Mechanistic Study of Palladium Nanobars and Nanorods. *J. Am. Chem. Soc*. **2007**, *129* (12), 3665–3675. https://doi.org/10.1021/ja0688023.

(52) Lim, B.; Kobayashi, H.; Camargo, P. H. C.; Allard, L. F.; Liu, J. Xia, Y. New Insights into the Growth Mechanism and Surface Structure of Palladium Nanocrystals. *Nano Res*. **2010**, *3*, 180–188. https://doi.org/10.1007/s12274-010-1021-5.

(53) Nalajala, N.; Chakraborty, A.; Bera, B.; Neergat, M. Chloride (Cl^-) Ion-Mediated Shape Control of Palladium Nanoparticles. *Nanotechnology* **2016**, *27* (6), 065603. https://doi.org/10.1088/0957-4484/27/6/065603.

(54) Sun, K.; Sun, X.; Zou, X.; Pang, W.; Hao, X.; Xu, Y.; Su, H. Origin for the Chloride and Citrate Ions Tuned Morphology of Pd Particles. *Appl. Surf. Sci*. **2023**, *638*, 158082. https://doi.org/10.1016/j.apsusc.2023.158082.

(55) Zhang, Z.; Shi, W.; Wang, W.; Xu, Y.; Bao, X.; Zhang, R.; Zhang, B.; Guo, Y.; Cui, F. Interfacial Electronic Effects of Palladium Nanocatalysts on the By-Product Ammonia Selectivity during Nitrite Catalytic Reduction. *Environ. Sci. Nano*. **2018**, *5* (2), 338–349. https://doi.org/10.1039/C7EN00909G.

(56) Zhao, Y.; Baeza, J. A.; Rao, N.K.; Calvo, L.; Gilarranz, M. A.; Li, Y. D.; Lefferts, L. Unsupported PVA- and PVP-Stabilized Pd Nanoparticles as Catalyst for Nitrite Hydrogenation in Aqueous Phase. *J. Catal*. **2014**, *318*, 162–169. https://doi.org/10.1016/j.jcat.2014.07.011.

(57) Li, H.; Zhu, Z.; Zhang, F.; Xie, S.; Li, H.; Li, P.; Zhou, X. Palladium Nanoparticles Confined in the Cages of MIL-101: An Efficient Catalyst for the One-Pot Indole Synthesis in Water. *ACS Catal* **2011**, *1* (11), 1604–1612. https://doi.org/10.1021/cs200351p.

(58) Zhang, D.; Guan, Y.; Hensen, E. J. M.; Xue, T.; Wang, Y. Tuning the Hydrogenation Activity of Pd NPs on Al-MIL-53 by Linker Modification. *Catal Sci Technol* **2014**, *4* (3), 795–802. https://doi.org/10.1039/c3cy00910f.

(59) Ebbesen, S. D.; Mojet, B. L.; Lefferts, L. In Situ ATR-IR Study of Nitrite Hydrogenation over Pd/Al2O3. *J Catal* **2008**, *256* (1), 15–23. https://doi.org/10.1016/j.jcat.2008.02.013.

(60) Shin, H.; Jung, S.; Bae, S.; Lee, W.; Kim, H. Nitrite Reduction Mechanism on a Pd Surface. *Environ Sci Technol* **2014**, *48* (21), 12768–12774. https://doi.org/10.1021/es503772x.

(61) Shuai, D.; McCalman, D. C.; Choe, J. K.; Shapley, J. R.; Schneider, W. F.; Werth, C. J. Structure Sensitivity Study of Waterborne Contaminant Hydrogenation Using Shape- and Size-Controlled Pd Nanoparticles. *ACS Catal* **2013**, *3* (3), 453–463. https://doi.org/10.1021/cs300616d.

Chapter 3

Investigation of ethylene adsorption behavior on Ag^{+}-exchanged zeolites

1. Introduction

Ethylene gas (C_2H_4) is a natural plant growth hormone that plays a crucial role in the ripening process of fruits, vegetables, and flowers. The ripening process includes changes such as color development, adventitious roots induction and promotion of fruit flowering, etc.[1,2] Apart from the endogenous C_2H_4 produced from the harvested products, external sources of C_2H_4 (e.g., engine exhausts) also occurs in the cold chain, which can induce accelerated softening and ripening, thus C_2H_4 must be properly removed from the space to prevent overripening or spoilage during the storage and transportation of fruits and vegetables. Given these effects, research on removing C_2H_4 from space (e.g., adsorptive removal or catalytic combustion of C_2H_4 at low temperature) have been widely conducted and some technologies have already been launched for application to extend the shelf-life of packaged procedure.[3,4]

From a different point of view, if fruits and vegetables are harvested at the immature stage, a proper artificial ripening by C_2H_4 during the storage and transportation can achieve precise control of ripening process, providing fresh fruits and vegetables without spoilage to consumers. Besides, field application of C_2H_4 can boost seed germination, bulb sprouting and flowering for growing plants in greenhouse.[5,6] In contrast to the great effort in developing C_2H_4 scavengers, the development of technology for proper C_2H_4 application, i.e., the development of technology for sustained release of C_2H_4, is far less conducted. Postharvest applications of C_2H_4 are predominantly from liquid C_2H_4 releaser or cylinders of compressed C_2H_4. A well-known liquid C_2H_4 releaser is Ethephon (2-chloroethylphosphonic acid). However, the use of Ethephon needs careful handling to reduce exposure to human and environment. And only proper application rates and period to plants are allowed (e.g., the use of Ethephon on fruiting apple trees has been called cancelled in Canada), thus the operator needs to be familiar with the instructions. Compared to the commercial use of pressurized cylinders, the encapsulation of C_2H_4 into a solid matrix is more fascinating in consideration of safety during the storage and transportation. Besides, the utilization of solid materials may favor the slow release of C_2H_4 to control the ripening process of fruits and vegetables. This is particularly advantageous for managing the ripening process of fruits and vegetables during transportation or storage, allowing better preservation of freshness and quality until they reach consumers.

Although generally the development of C_2H_4 release material is limited, several research have been conducted to encapsulate C_2H_4 for postharvest application by using α-cyclodextrin (α-CD), which is a natural starch derivative resulted from enzymatic degradation of starch by cyclodextrin glycosyltransferase.[7–10] The encapsulation of C_2H_4 into α-CD usually follows a liquid encapsulation method, which includes the steps that (1) dissolving α-CD in water, (2)

introducing C_2H_4 into the solution for complexation, (3) collecting the precipitant after complexation to equilibrium and (4) drying. Indeed, this liquid encapsulation method has significant drawbacks for practical application. For instance, the complexation process usually requires a long time up to 120 h and at elevated pressures up to 1.5 MPa,[7–10] while the recovery of crystalline complex powder is only less than 45% despite such a time-consuming process.[7,11] Besides, a final drying process is required after collection from liquid phase, which is critical for the retention of encapsulated C_2H_4 that part of encapsulated C_2H_4 may release during the drying process. Considering the drawbacks of complex preparation processes and operational challenges associated with α-CD application for ethylene encapsulation, there is a significant interest in and necessity for developing a solid material that is easier to prepare and use than the α-CD.

As mentioned in Chapter 1, zeolites serve as typical porous materials for application as an adsorbent. The presence of aluminum in zeolite gives a negative charge to the framework, which is in turn compensated by an extra-framework cationic species. These ion-exchange sites on the pore walls of zeolites serve as function groups, where the cationic species can be further exchanged with other metal cations, facilitating the facile preparation of metal cation-exchanged zeolites. Ag^+-exchanged zeolites are capable for C_2H_4 adsorption owing to the π-complex interaction effect between Ag^+ and C_2H_4,[12–17] where the filled π orbital of C_2H_4 overlaps with the vacant 5s orbital of Ag^+, and the filled 4d orbital of Ag^+ overlaps with the vacant π* orbital of C_2H_4 (**Figure 3-1**).[17] Along with the high surface area of zeolites, a significant encapsulation amount of C_2H_4 can be expected by applying Ag^+-exchanged zeolites as a matrix. Besides, the π-complex interaction between Ag^+ and C_2H_4 with a strong binding character could favor the sustained release behavior (**Figure 3-2**). Further investigation on the interaction between Ag^+ and zeolite framework will provide valuable information for tuning the C_2H_4 adsorption strength on Ag^+.

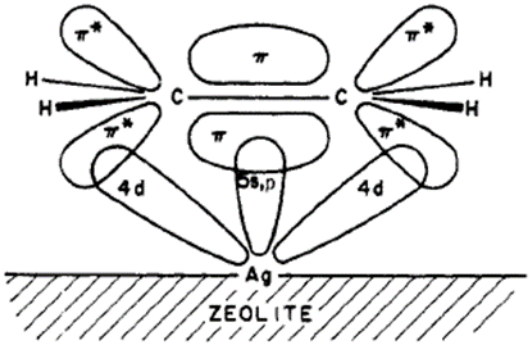

Figure 3-1. Schematic illustration of π-complex interaction effect between Ag^+ and C_2H_4. (ref. 17)

In short, materials with high adsorption capacity of C_2H_4 are demanded to induce desired biological effects in a more efficient and cost-effective manner. Additionally, a strong adsorption strength between the adsorbent and C_2H_4 is favorable for achieving sustained release behavior. Although several research of C_2H_4 adsorption over Ag^+-exchanged zeolites have been reported, most of them focused on the adsorptive removal of trace C_2H_4 from the space or the separation of C_2H_4 from a mixture.[12,15,18–21] The study on applying Ag^+-exchanged zeolite as a C_2H_4 release agent has not been carried out yet. Here, the present author wishes to have insight into the development of C_2H_4 release materials with high C_2H_4 adsorption capacity and strong adsorption strength through systematical investigation of C_2H_4 adsorption behavior over a series of Ag^+-exchanged zeolites with different topologies. In this chapter, adsorption behavior including adsorption capacity and adsorption strength of C_2H_4 over a series of Ag^+-exchanged zeolites were systematically studied to efficiently lead them to C_2H_4 release materials.

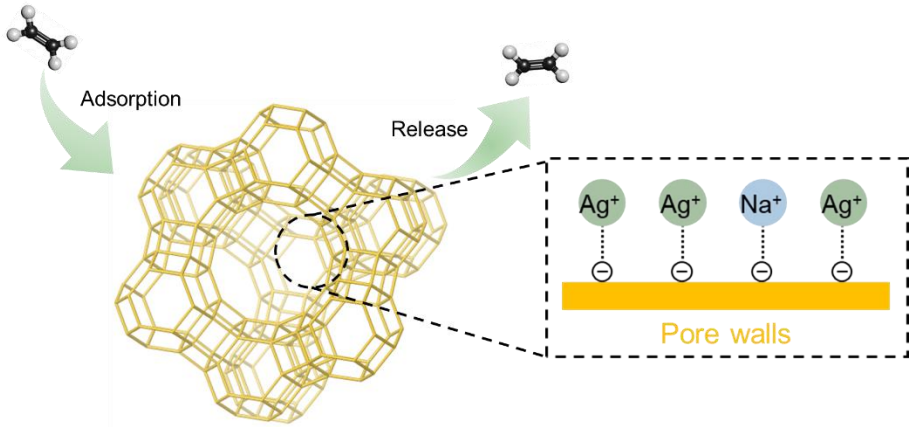

Figure 3-2. Schematic illustration of applying Ag^+-zeolites as C_2H_4 release materials.

2. Experiment

2.1 Materials

All chemicals used in this study were commercially available and used without further treatment. Na-Y-5.6 (JRC-Z-5.6), H-Y-4.8 (JRC-Z-HY-4.8), NH_4-ZSM-5-23 (HSZ-820NHA), H-Beta-25 [JRC-Z-B25(1)], Na-MOR-20 [JRC-Z-M-20(1)] and H-MOR-20 [JRC-Z-HM-20(3)] were supplied from Catalysis Society of Japan. Na-A-2 (Zeolum A-4) and Na-X-2.5 (Zeolum F-9) were provided by Tosoh Corp. H-USY-80 (CBV780) was provided by Zeolyst International. All these parent zeolites are denoted as A-B-C, where A, B and C stand for cation, zeolite type and ratio of SiO_2/Al_2O_3, respectively. For example, NH_4-ZSM-5-23 represents ZSM-5 type zeolite in NH_4^+ form with $SiO_2/Al_2O_3 = 23$. Activated carbon (AC) was provided by Kurary Co., Ltd. A commercial ripener (C_2H_4 release agent) was purchased from Japan Fruit Growers Cooperative Association. Sodium nitrate ($NaNO_3$, 98.0%) and hydrofluoric acid (HF, 46.0% ~ 48.0%) were purchased from FUJIFILM Wako Pure Chemical Corp. Silver nitrate ($AgNO_3$, 99.9%) was purchased from KANTO CHEMICAL CO., INC. Ultra-pure water (Milli-Q) was used for all the experiments.

2.2 Preparation of Ag^+-exchanged zeolites

For zeolites in Na^+ form, they were directly used for introduction of Ag^+ through ion exchange reaction. Typically, 3 g of zeolite was treated in a $AgNO_3$ solution (2.28 g/50 mL) at 50 °C under vigorous stirring for 2 h. Different loadings of Ag^+ were achieved by changing the concentration of $AgNO_3$ in the solution or the times of ion exchange introduction. Thereafter, the solid was separated from the mixture by filtration and washed with 50 mL of Milli-Q for three times. Then, the obtained solid sample was dried overnight at 100 °C.

Zeolites in NH_4^+ form (typically NH_4-ZSM-5) were calcined in air at 550 °C for 4 h to obtain zeolites in the H^+ form. Subsequently, for the zeolites in H^+ form, they were then treated with $NaNO_3$ solution to change to the Na^+ form. Typically, 3 g of zeolite was contacted with a $NaNO_3$ solution at 80 °C under vigorous stirring for 2 h. Thereafter, the solid was separated from the mixture by filtration and washed with 50 mL of Milli-Q for three times. After the process was repeated for 2 times and dried overnight at 100 °C, the obtained sample was afforded for further ion exchanged process with $AgNO_3$ the same as that described above.

The obtained Ag^+ ion-exchanged zeolites are denoted as Ag_x-zeolites, where x stands for the ion-exchange rate of Ag^+. For the zeolites with known ratio of SiO_2/Al_2O_3 before Ag ion-exchange reaction, the chemical composition of the zeolites can be defined as $Na_aAl_aSi_bO_c \cdot mH_2O$, where $2b/a$ equals to the ratio of SiO_2/Al_2O_3. Correspondingly, the chemical composition of the Ag^+-

zeolites is defined as $Ag_dNa_{(a-d)}Al_aSi_bO_c \cdot nH_2O$. Assuming that all Na^+ in zeolites can be exchanged with Ag^+, the ion-exchange rate of Ag^+ (x) equals to d/a can be calculated based on the actual loading of Ag^+.

2.3 Preparation of $AgNO_3$/AC

$AgNO_3$/AC was prepared by an impregnation method, where the same amount of support and $AgNO_3$ solution as those with 2.2 were used. After impregnation, the sample was dried overnight at 100 °C.

2.4 Characterization

Powder X-ray diffraction (PXRD) patterns were collected on an X-ray diffractometer (D2 Phaser, Bruker) using Cu Kα radiation at a scan speed of 0.02° per step in the 2θ range of 5° to 50°.

Thermogravimetric and differential thermal analyses (TG-DTA) were performed on TG 8120 (Rigaku Thermoplus) from room temperature to 400 °C in air flow at a heating rate of 10 °C min^{-1}.

The Ag contents of the Ag^+-exchanged zeolites were quantified by using an inductively coupled plasma-atomic emission spectrometer (ICP-AES, ICPE-9000). The solid samples were dissolved in hydrofluoric acid and the diluted solutions were afforded to ICP-AES measurement.

The surface area and pore volume were estimated from a N_2 adsorption-desorption isotherm taken at -196 °C (BELSORP mini, BEL Japan, Inc). Before the measurement, the sample was treated under vacuum at 200 °C for 4 h to remove the weakly adsorbed water. The specific surface area was calculated by applying Brunauer-Emmett-Teller (BET) equation to an adsorption isotherm in the P/P_0 range of 0 to 0.05.

Diffuse reflectance UV-vis spectra were measured by using an UV-vis spectrometer (JASCO V-770) with a standard diffuse reflectance accessory. $BaSO_4$ was used to collect the background spectra at room temperature. The spectra of samples were collected at ambient atmospheres. Influence of the pretreatment at 200 °C on Ag species was investigated by performing diffuse reflectance UV-vis measurement using an UV-vis spectrometer (JASCO V-750) equipped with an *in-situ* sample cell, which was connected to a gas flow system. The light beam was led into the integrating sphere coated by $BaSO_4$ and the background spectrum was collected using $BaSO_4$ pellet. The spectra of the samples were collected under O_2/He flow and heated to 200 °C. The absorption intensity was calculated and converted to pseudo-absorbance using Kubelka-Munk equation: $KM = k/s = (1-R)^2/2R$, where k, s and R represent absorption coefficient of the sample, scattering coefficient and diffuse reflectance, respectively.

Ex-situ Ag K-edge X-ray absorption spectra collected in transmission mode were obtained at the beamline NW10A of the Photon Factory in KEK, using the Si (311) channel-cut monochromator (supported by A. Yamamoto, Kyoto Univ.). Ag^+-zeolites pretreated under N_2 flow at 200 °C were molded into pellets and stored in sealed packs until measurements. Ag foil and $AgNO_3$ were used as references.

Fourier transform infrared (FTIR) spectra of C_2H_4 adsorbed on Ag^+-zeolites were recorded on JASCO FT/IR-4600 with TGS detector at 25 °C. The parent zeolites and Ag^+-zeolites were molded into pellet and pretreated under vacuum at 200 °C for 1 h. After being cooled to 25 °C, C_2H_4 at different pressure was introduced into the sample cell for adsorption. Afterwards, the sample cell was evacuated again using vacuum pump to remove C_2H_4 in gas phase, and the spectrum was recorded.

2.5 Ethylene adsorption measurement

Ethylene adsorption measurement was carried out to quantify adsorption capacity of C_2H_4 for each sample. Before the measurement, the sample was treated under vacuum at 200 °C for 4 h. The C_2H_4 adsorption isotherms were taken at 25 °C with a BELSORP Mini instrument (BEL Japan Inc.). The measurement was performed two times consecutively, where after the first run, the sample was degassed for 2 h to remove the weakly adsorbed C_2H_4 and then the second run was performed. Difference in the saturated adsorption amounts between the first and second adsorption measurements was assumed to be the amount of chemisorbed C_2H_4.

3. Results and discussion

3.1 Characterization of zeolites and Ag^+-zeolites

ICP-AES measurements were first carried out to quantify the introduced amount of Ag^+ in each Ag^+-zeolite, and the results are summarized in **Table 3-1**. Basically, a higher Ag^+ content was obtained by the same ion-exchange process for the zeolite with lower SiO_2/Al_2O_3 ratio (e.g., Ag^+ content of 3.10 mmol g^{-1} for X with $SiO_2/Al_2O_3 = 2.5$ and Ag^+ content of 0.57 mmol g^{-1} for Beta with $SiO_2/Al_2O_3 = 25$). This result is consistent with the general principle that zeolites with lower SiO_2/Al_2O_3 ratios possess the larger number of ion-exchange sites, namely higher ion-exchange capacities.

Table 3-1. Introduced amounts of Ag^+ in Ag-zeolites by ion-exchange reaction.

Ag^+-zeolite	**Ag^+ content (mmol g^{-1})** *
Ag_{68}-A	2.99
Ag_{36}-A	1.84
Ag_{17}-A	0.96
Ag_{9}-A	0.51
Ag_{82}-X	3.10
Ag_{36}-X	1.59
Ag_{20}-X	0.92
Ag_{9}-X	0.45
Ag_{85}-Y	2.09
Ag_{62}-Y	1.76
Ag_{38}Y	1.15
Ag_{19}-Y	0.61
Ag_{99}-MOR	1.16
Ag_{66}-ZSM-5	0.72
Ag_{57}-Beta	0.57

* Determined by ICP-AES.

The framework structures of different types of zeolites used in this study are shown in **Figure 3-3**. A type zeolite (**Figure 3-3a**) has LTA topology constructed with sodalite cages connected through 4-membered rings, forming a cubic 3-dimensional (3D) network. ZSM-5 zeolite (**Figure 3-3b**) has MFI topology, which is composed of several pentasil units consisting of 5-membered rings. The pentasil units are interconnected to form straight and zigzag channels. The intersection of these channels forms orthorhombic 3D network. MOR zeolite (**Figure 3-3c**) has orthorhombic 1D channels consisting of parallel 12-membered rings and 8-membered rings connected by narrower 8-membered ring side pockets. Beta zeolite (**Figure 3-3d** shows Beta-A) is an intergrowth hybrid possessing a 3D 12-membered ring pore system. X and Y zeolites share the same FAU topology (**Figure 3-3e**) consisting of sodalite cages, which are connected through hexagonal prisms. They have a cubic 3D network.

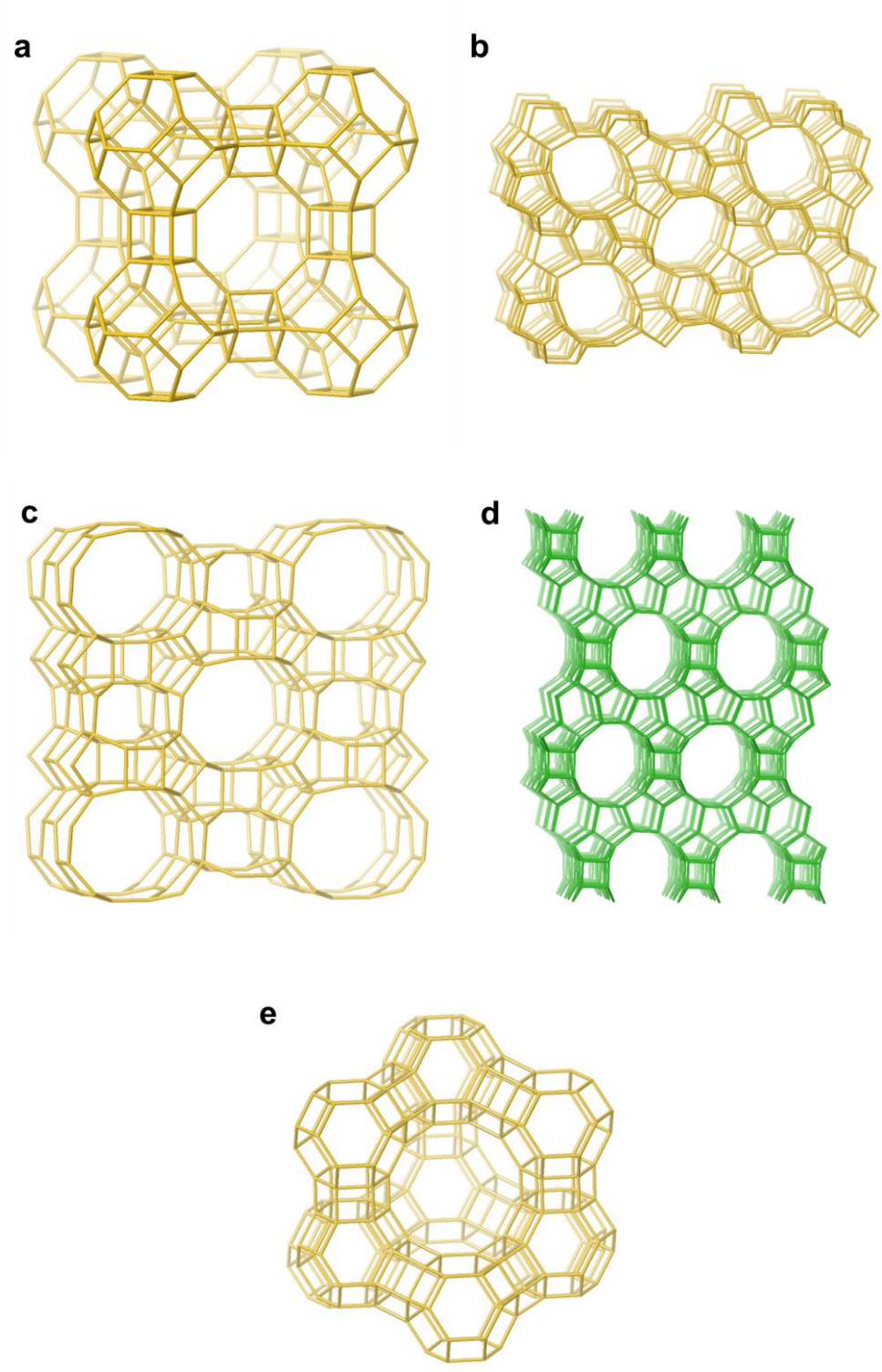

Figure 3-3. Framework structures of (a) LTA (A), (b) MFI (ZSM-5), (c) MOR (MOR), (d) *BEA (Beta-A), (e) FAU (X and Y) zeolites. Framework structures are generated using the 3D drawing function of the IZA web site.

Figure 3-4 shows the PXRD patterns of both parent zeolites and Ag^+-exchanged zeolites. The PXRD patterns of all parent zeolites exhibited the corresponding topologies of the zeolite frameworks, demonstrated by the consistency between the PXRD patterns of parent zeolites and the corresponding simulated ones. An exception was H^+-Beta, as Beta zeolite is an intergrowth of two or more related polymorphs, including polymorphs A, B, C, etc.[22–24] The H^+-Beta used in this study was an intergrowth of polymorphs A and B, indicated by the absence of the strong reflection peak that would typically appear at around $2\theta = 9.7°$ for polymorphs C, D and E. The Ag^+-exchanged Y, MOR, ZSM-5 and Beta zeolites exhibited similar characteristics diffraction peaks to the parent zeolites, suggesting that the introduction of Ag^+ did not change the framework structures of these zeolites. However, drastic decreases in the intensity of diffraction peaks were observed for MOR and ZSM-5 zeolites with the introduction of Ag^+. Similarly, slight decrease in the intensity of diffraction peaks was also observed for A, X, Y and Beta zeolites. Such decrease in the diffraction peak intensities might be attributed to certain decrease of crystallinity or redistribution of the charge compensation cations due to the exchange Na^+ to Ag^+.[25,26] For A and X type zeolites, most of the characteristic diffraction peaks maintained unchanged after the Ag ion-exchange reaction, while increase in the intensities of the diffraction peaks, which corresponds to the (400) plane of zeolite framework, was observed for Ag^+-A ($2\theta = 14.4°$) and Ag^+-X ($2\theta = 14.2°$). The same phenomenon was also observed in previous studies.[26,27] It should be noted that no diffraction peak corresponding to crystalline metallic Ag or Ag_2O was observed in the Ag-zeolites, indicating that the introduced Ag^+ were well dispersed on or over the zeolite frameworks.

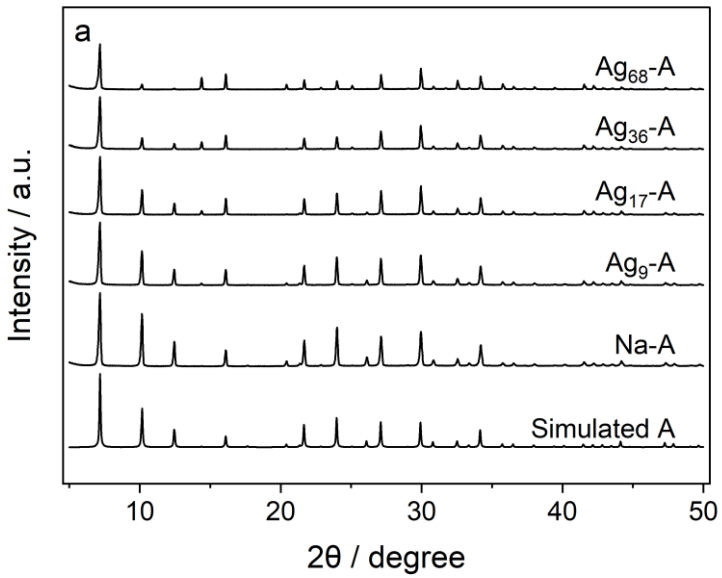
a
Ag68-A
Ag36-A
Ag17-A
Ag9-A
Na-A
Simulated A
Intensity / a.u.
10
20
30
40
50
2θ / degree

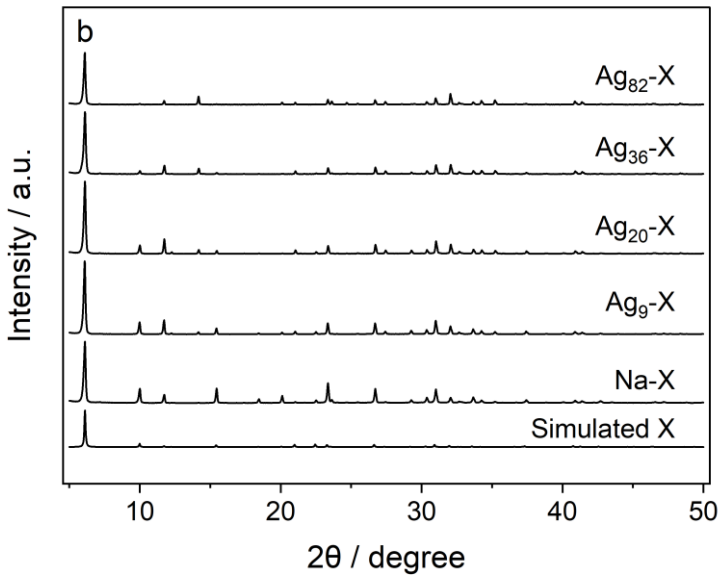
b
Ag82-X
Ag36-X
Ag20-X
Ag9-X
Na-X
Simulated X
Intensity / a.u.
10
20
30
40
50
2θ / degree

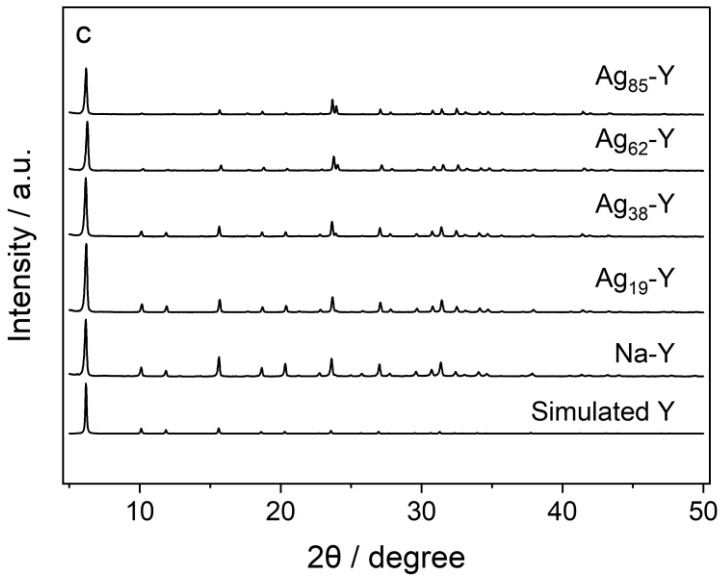
c
Ag85-Y
Ag62-Y
Ag38-Y
Ag19-Y
Na-Y
Simulated Y
Intensity / a.u.
10
20
30
40
50
2θ / degree

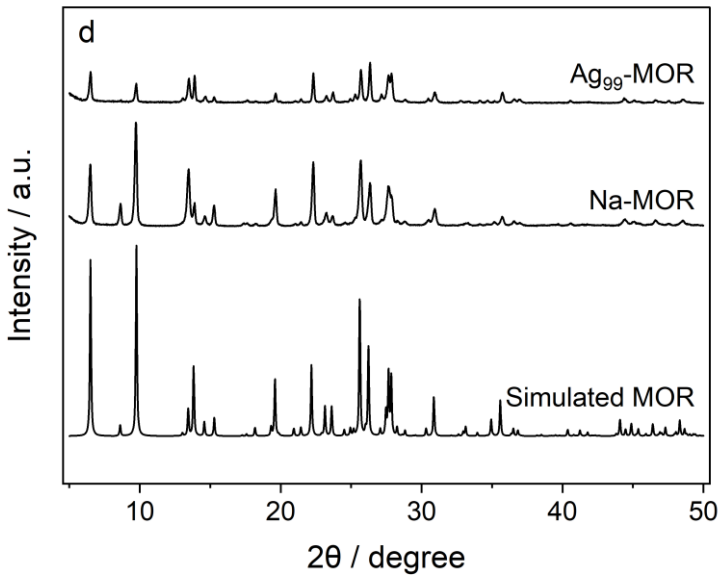
d
Ag99-MOR
Na-MOR
Simulated MOR
Intensity / a.u.
10
20
30
40
50
2θ / degree

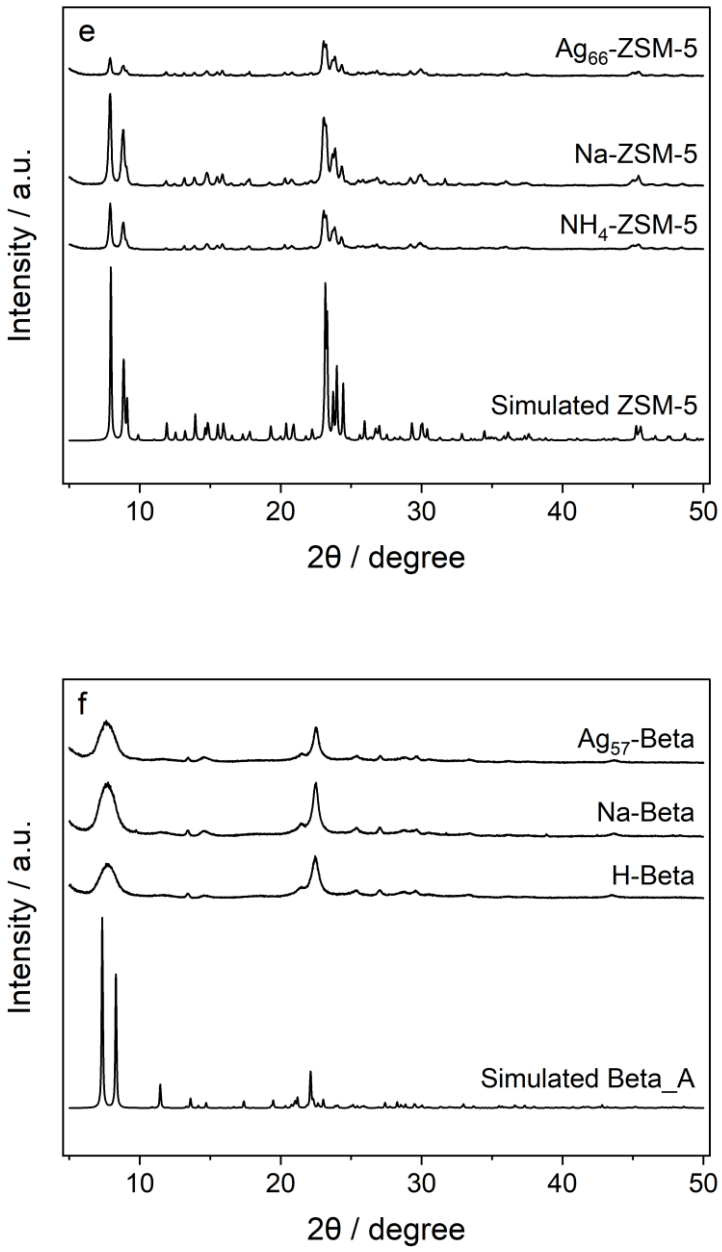

Figure 3-4. PXRD patterns of parent zeolites and Ag^+-zeolites. For ZSM-5 and Beta zeolites, the PXRD patterns of those after Na ion-exchange reaction are included. Simulated patterns are adapted from IZA web site.

Figure 3-5 shows the N_2 adsorption-desorption isotherms of the parent and Ag^+-exchanged zeolites, from which the specific surface areas and micropore volumes were calculated, and the results are summarized in **Table 3-2**. Both Ag^+-A and the parent A-type zeolites exhibited only very small adsorption amount of N_2 at -196 °C. This result can be attributed to the fact that the kinetic diameter of N_2 (0.364 nm) is close to the pore window of parent Na^+-A zeolite (ca. 0.4 nm), resulting in the kinetic hindrance of the adsorption of N_2 at the temperature. The other zeolites used in this study all displayed a type I adsorption isotherm, wherein a drastic increase of N_2 adsorption at very low P/P_0 due to micropore filling was observed,[28] indicating that the well-developed microporosity of the zeolites was not influenced by the introduction of Ag^+. Only a slight decrease of N_2 adsorption amount and micropore volume were observed after Ag^+ ion-exchange, which could be due to the occupation of Ag^+ inside the micropores.

Table 3-2. BET surface areas and micropore volumes of parent and Ag ion-exchanged zeolites.

Sample	S_{BET} ($m^2\ g^{-1}$) [a]	Micropore volume ($cm^3\ g^{-1}$) [b]
Na-X	708	0.255
Ag_{36}-X	673	0.245
Na-Y	865	0.312
Ag_{62}-Y	677	0.237
Na-MOR	469	0.153
Ag_{99}-MOR	406	0.131
Na-ZSM-5	352	0.104
Ag_{66}-ZSM-5	334	0.103
NH_4-Beta	590	0.152
Ag_{57}-Beta	532	0.144

[a] The specific surface area was calculated based on the BET method. [b] The micropore volume was calculated by the *t*-plot method.

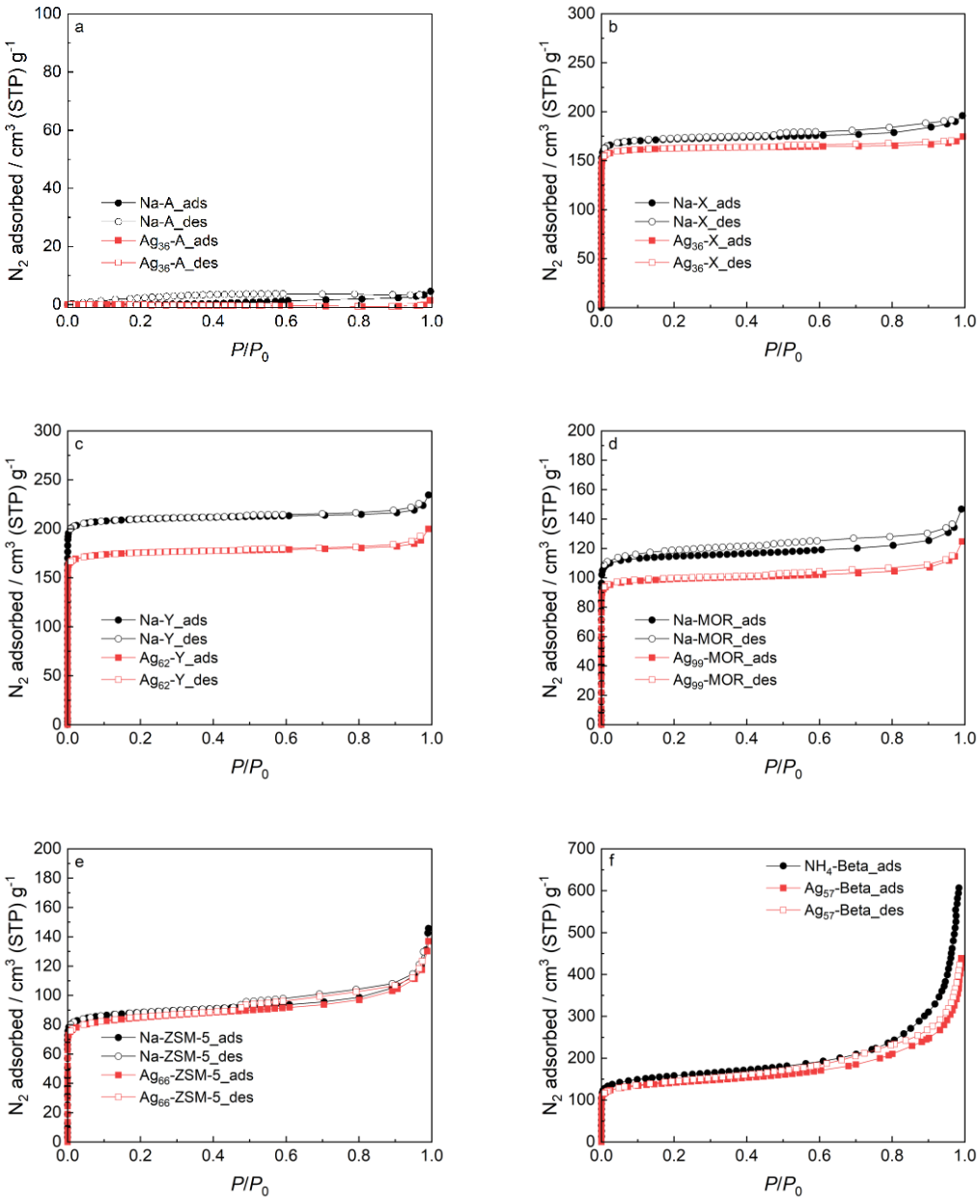

Figure 3-5. N_2 adsorption-desorption isotherms for Ag^+-zeolites and corresponding parent zeolites taken at -196 °C.

TG-DTA measurements were carried out to investigate the thermal behavior of zeolites with and without Ag^+. **Figure 3-6** shows the TG profiles of parent zeolites and Ag^+-zeolites. The weight decreased by one step below 200 °C for all samples, which was due to the release of adsorbed water. The zeolites with lower Si/Al ratios had slightly higher water contents than those with higher Si/Al ratios because of relatively high hydrophilicity.[29] No significant decrease of thermal stability was observed with the introduction of Ag^+. Accordingly, all the zeolites were heated to 200 °C as pretreatment to remove adsorbed water.

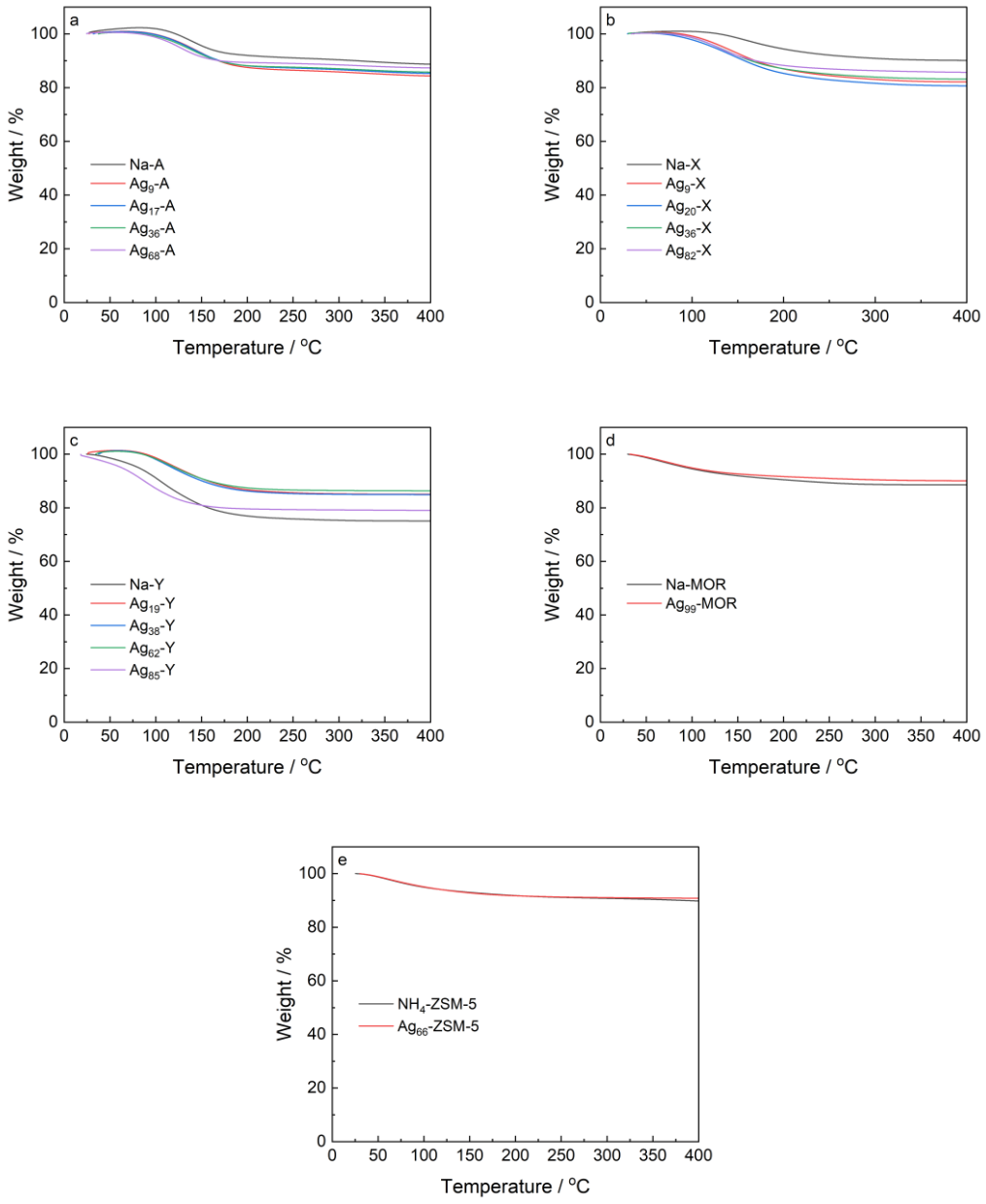

Figure 3-6. TG profiles of parent zeolites and Ag^+-zeolites.

3.2 Ethylene adsorption isotherms

Ethylene adsorption isotherms were measured to quantify the ethylene encapsulation capacity for each sample. As described in the experimental section, the adsorption measurement was performed twice consecutively, with *in situ* vacuum treatment between two measurements to remove physically (weakly) adsorbed C_2H_4. It is anticipated that if chemical adsorption occurred, some adsorption sites would be occupied by the adsorbed C_2H_4 and would not be able to adsorb C_2H_4 further, resulting in a difference in adsorption amount between the two adsorption measurements. The amount of chemically adsorbed C_2H_4 can be estimated from the difference in the saturated adsorption amounts between two adsorption isotherms.

The C_2H_4 adsorption over parent Na^+-Y and Ag^+-Y were first investigated. **Figure 3-7** shows the adsorption isotherms of C_2H_4 for Na^+-Y and Ag^+-Y. As **Figure 3-7a** shows, Na^+-Y exhibited large adsorption amounts of C_2H_4 at 1 bar, while no chemical adsorption was observed, as indicated by no difference between the adsorption amounts of the two consecutive adsorption measurements. In contrast, with the introduction of Ag^+, as shown in **Figure 3-7b**, chemical adsorption of C_2H_4 occurred as the difference between the adsorption amounts of the two consecutive adsorption measurements was observed.

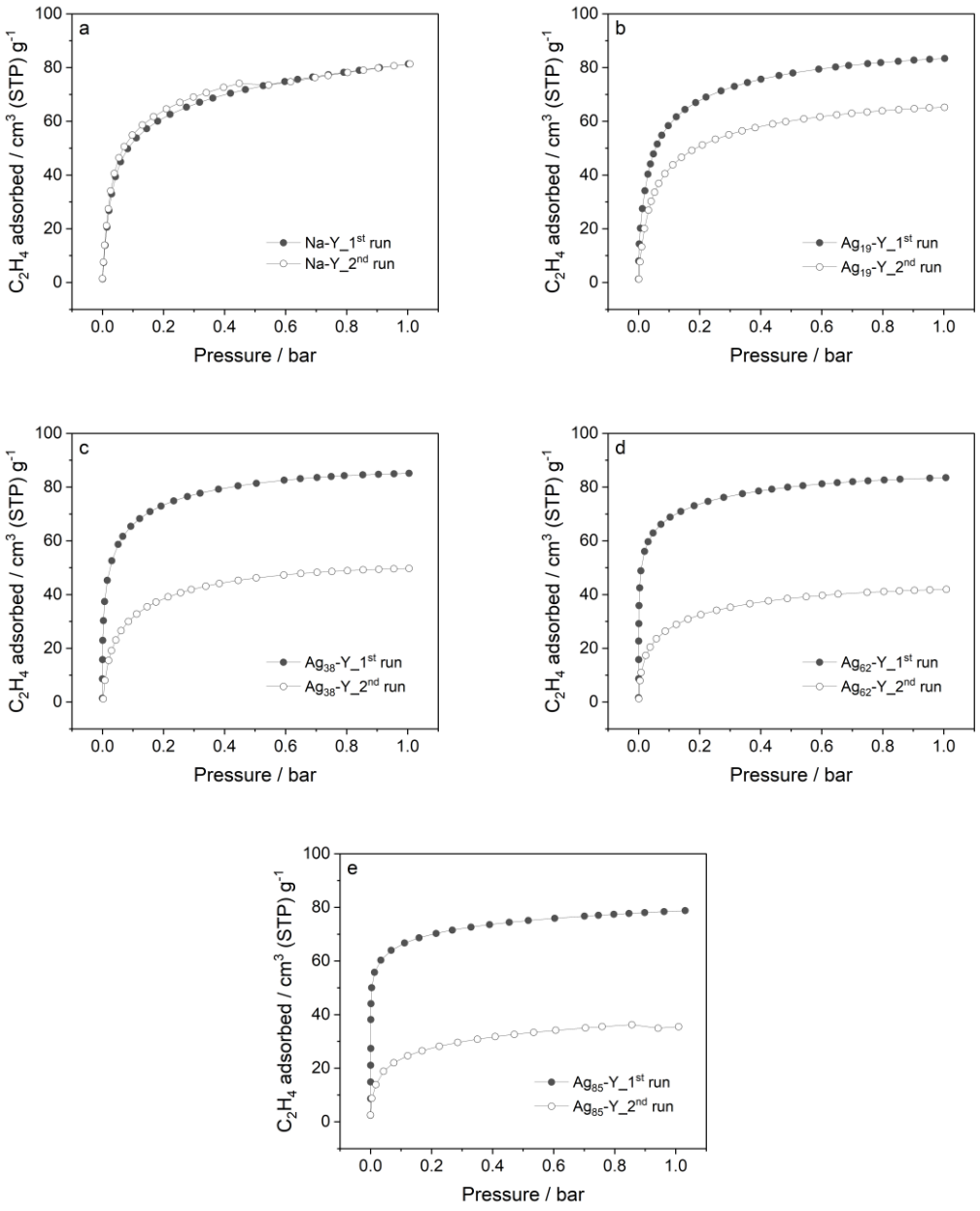

Figure 3-7. Adsorption isotherms of C_2H_4 for Na^+-Y and Ag^+-Y with different Ag^+ amounts. The isotherms were taken at 25 °C.

For comparison, the C_2H_4 adsorption over $AgNO_3$/AC, SiO_2-Al_2O_3, H^+-form Y as well as a commercial ripener were also investigated. **Figure 3-8** shows the adsorption isotherms of C_2H_4 for them. As the figures show, although $AgNO_3$/AC and H^+-Y-4.8 exhibited rather high C_2H_4 adsorption amounts at 1 bar, no or only little amount of chemically adsorbed C_2H_4 was observed. SiO_2-Al_2O_3, H^+-USY-80 and the commercial ripener showed less C_2H_4 adsorption amounts than

$AgNO_3$/AC, H^+-Y-4.8, Na^+-Y and Ag^+-Y. They also exhibited no significant amount of chemically adsorbed C_2H_4.

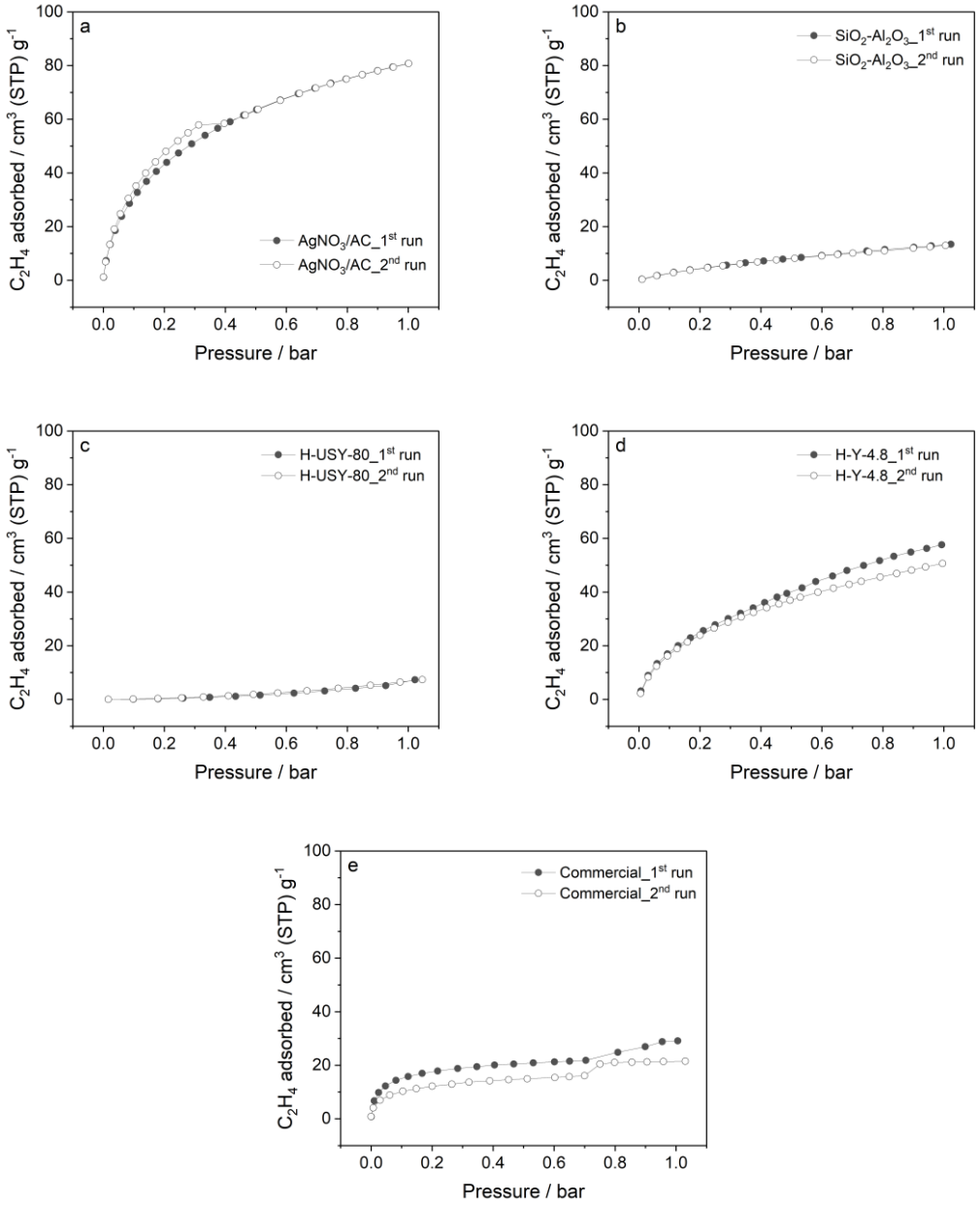

Figure 3-8. Adsorption isotherms of C_2H_4 for (a) $AgNO_3$/AC, (b) SiO_2-Al_2O_3, (c) H-USY-80, (d) H-Y-4.8 and (e) Commercial ripener. The isotherms were taken at 25 °C.

The C_2H_4 adsorption over different Na^+-zeolites and Ag^+-zeolites were further investigated. **Figures 3-9** and **3-10** show adsorption isotherms of C_2H_4 for A and X type zeolites in Na^+-form and those after Ag^+ introduction, **Figure 3-11** show those for Ag^+-MOR, Ag^+-ZSM-5 and Ag^+-Beta. As shown in **Figures 3-9a** and **3-10a**, the Na^+-form zeolites (Na^+-A and Na^+-X) exhibited similar C_2H_4 adsorption behavior with that exhibited by Na^+-Y, where no chemical adsorption occurred. Chemical adsorption was also confirmed for Ag^+-A and Ag^+-X. Among these A, X and Y type zeolites, compared with the parent Na^+-form zeolites or Ag^+-zeolites with lower Ag^+ contents, the Ag^+-zeolites with larger Ag^+ contents exhibited a more dramatic increase of adsorption amount at relatively low pressures, especially below 0.05 bar. These results indicated that C_2H_4 was strongly interacted with Ag^+-zeolites, presumably the π-complex interaction between C_2H_4 and Ag^+.[14,17] Similar C_2H_4 chemical adsorption behavior was also observed over Ag_{99}-MOR, Ag_{66}-ZSM-5 and Ag_{57}-Beta, as shown in **Figures 3-11a**, **b**, and **c**, respectively. Obviously, all these Ag^+-zeolites exhibited much higher C_2H_4 adsorption amounts than the commercial ripener (**Figure 3-8e**), indicating their potential as a candidate for C_2H_4 release.

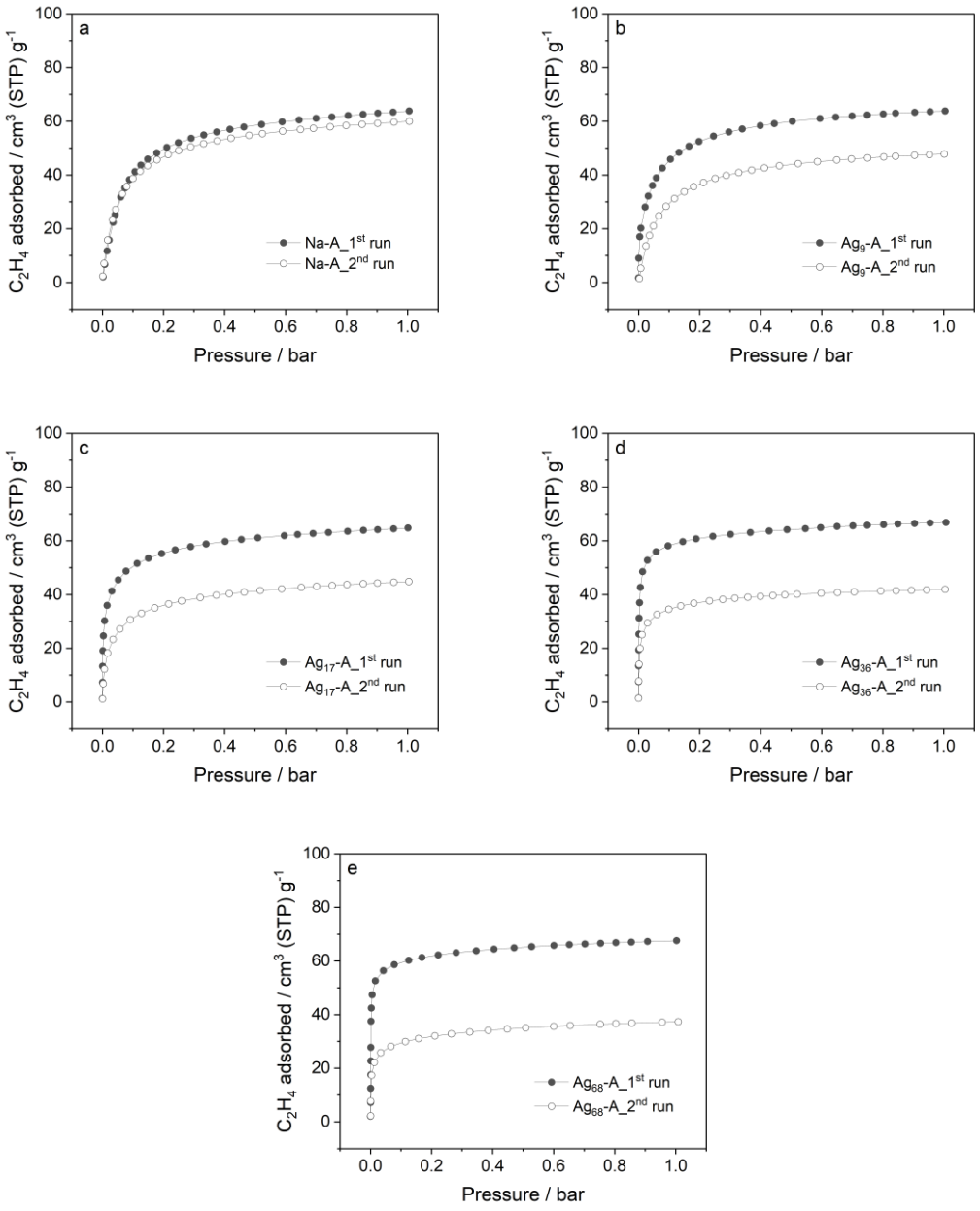

Figure 3-9. Adsorption isotherms of C_2H_4 for Na^+-A and Ag^+-A with different Ag^+ amounts. The isotherms were taken at 25 °C.

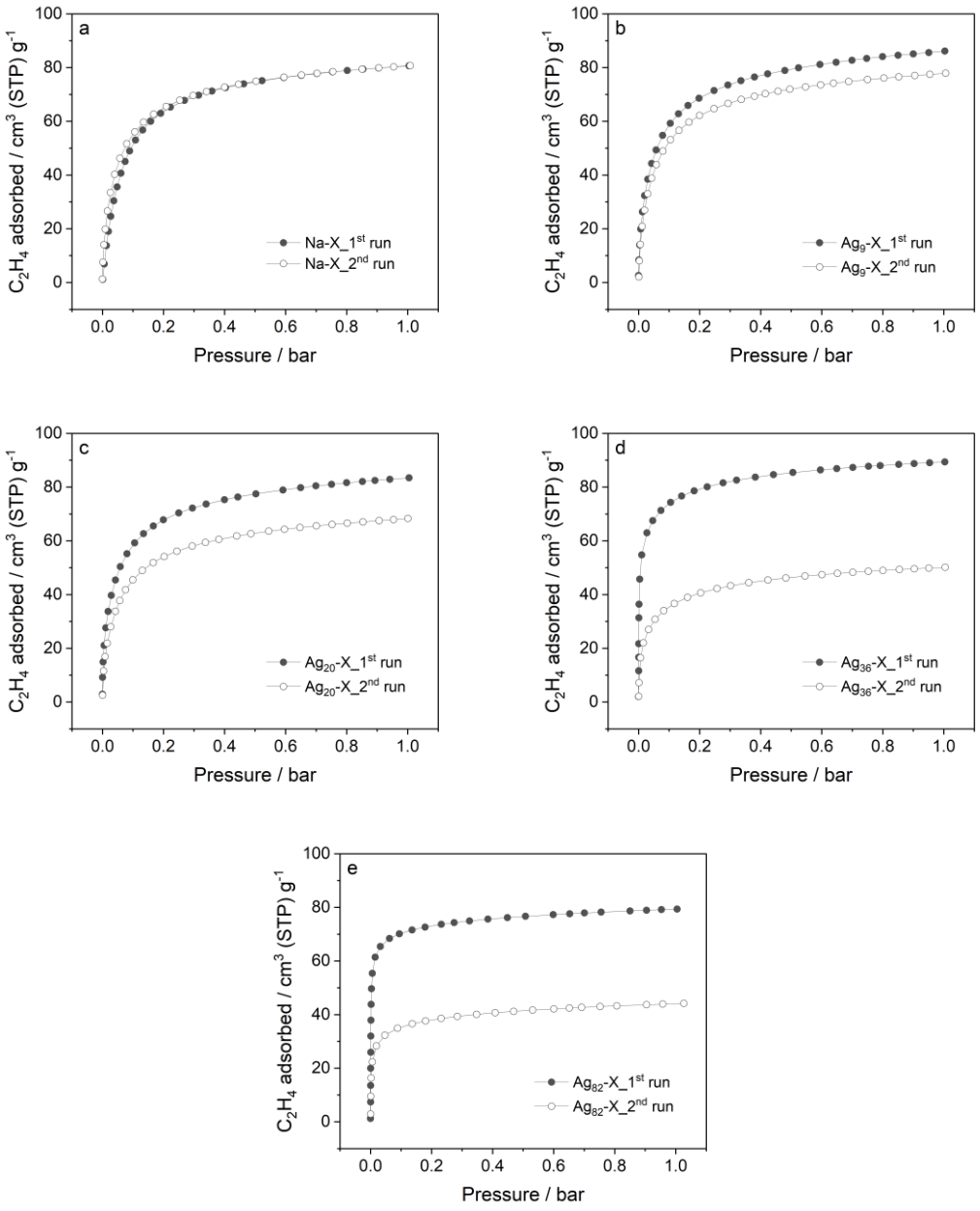

Figure 3-10. Adsorption isotherms of C_2H_4 for Na^+-X and Ag^+-X with different Ag^+ amounts. The isotherms were taken at 25 °C.

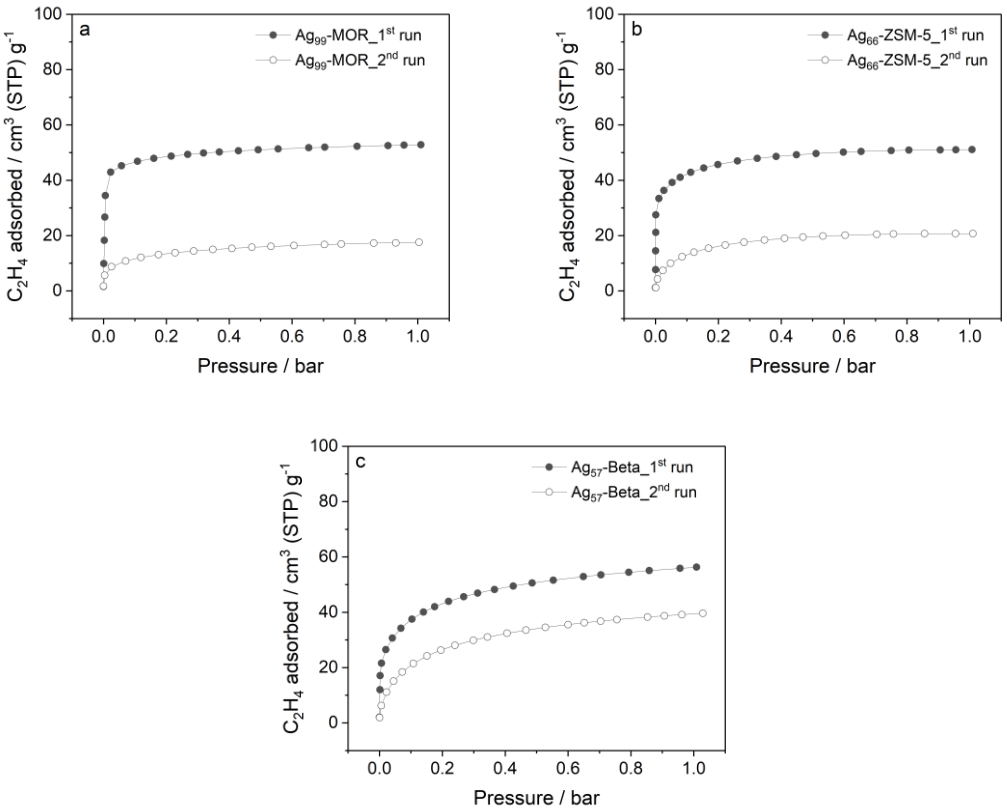

Figure 3-11. Adsorption isotherms of C_2H_4 for (a) Ag_{99}-MOR, (b) Ag_{66}-ZSM-5 and (c) Ag_{57}-Beta, respectively. The isotherms were taken at 25 °C.

The difference adsorption isotherms were subsequently obtained from the two adsorption isotherms obtained in consecutive runs, shown in **Figure 3-12**. It is evident that the chemical adsorption of C_2H_4 reached saturation at relative low pressure (<0.1 bar), as little increase in chemical adsorption amount was observed with the increase in the C_2H_4 pressure from around 0.1 to 1.0 bar. For convenience, hereafter, the difference in the adsorption amount at 1 bar is considered as the chemical adsorption capacity of C_2H_4.

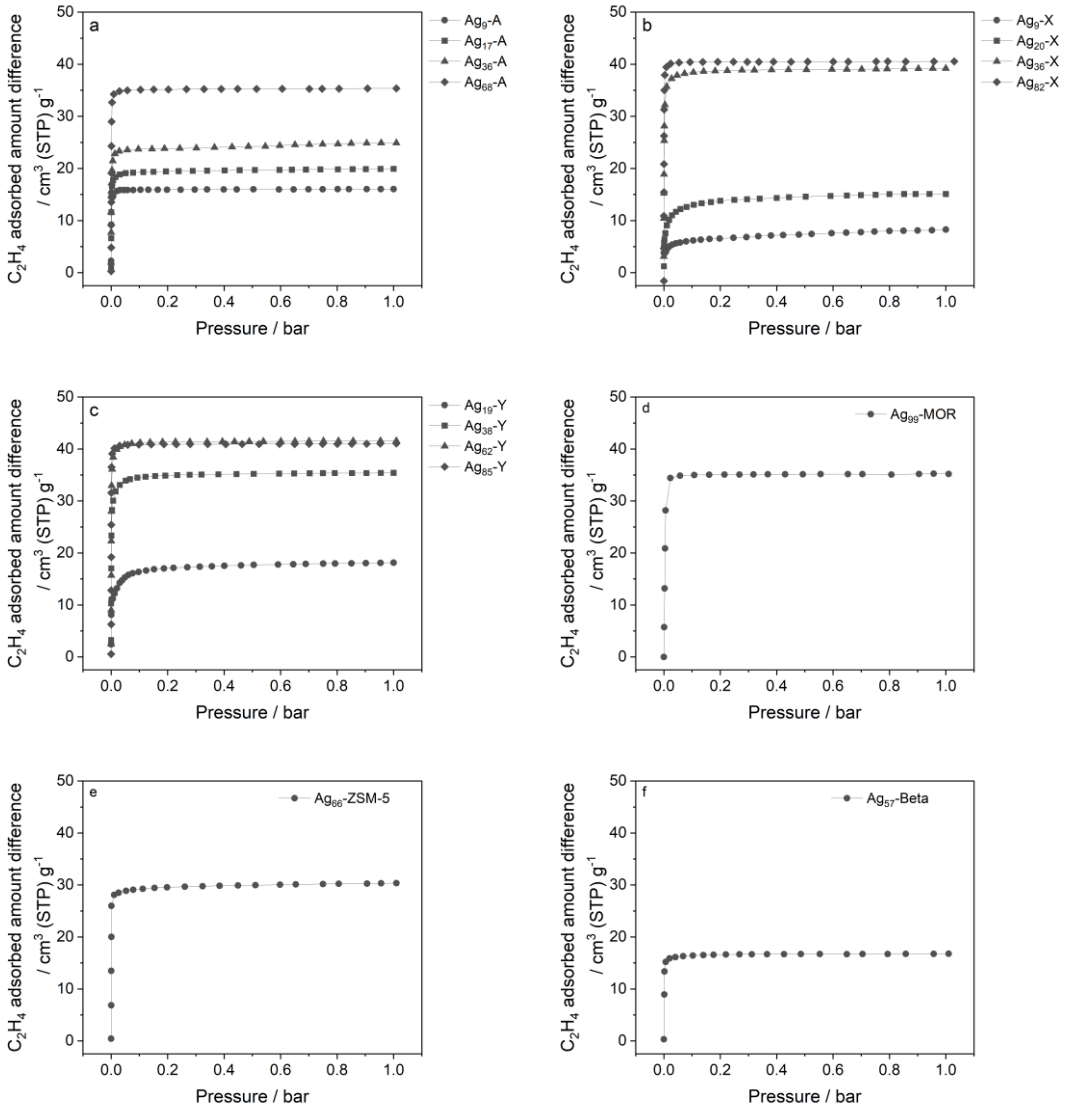

Figure 3-12. Difference adsorption isotherms of C_2H_4 for (a) Ag^+-A, (b) Ag^+-X and (c) Ag^+-Y with different Ag^+ contents, and those for (d) Ag_{99}-MOR, (e) Ag_{66}-ZSM-5, (f) Ag_{57}-Beta.

3.3 Relation between chemical adsorption capacity of C_2H_4 and Ag^+ contents

The relation between chemical adsorption capacity of C_2H_4 for Ag^+-zeolites [$n_{C_2H_4}$, mmol (STP) g^{-1}] and Ag^+ contents (n_{Ag}, mmol g^{-1}, calculated based on ICP-AES results) was investigated. In **Figure 3-13**, $n_{C_2H_4}$ is plotted as a function of n_{Ag} for all the Ag^+-zeolites tested in this study. As the figure shows, a clear trend was observed as $n_{C_2H_4}$ was increased with the increase in n_{Ag} up to around 2 mmol g^{-1}. However, no further increase in $n_{C_2H_4}$was observed even if n_{Ag} was further increased. This observed correlation between $n_{C_2H_4}$ and n_{Ag} is reasonable, if the chemical adsorption of C_2H_4 occurred on Ag^+ through the π-complex interaction between C_2H_4 and Ag^+. The reason why further increase in n_{Ag} did not bring further increase of $n_{C_2H_4}$ could be that the further introduction of Ag^+ formed different species rather than existing solely as isolated Ag^+, which would exhibit different adsorption behavior from that of such Ag^+ species. Additionally, it is also evident that the framework structure of the parent zeolite had an impact on $n_{C_2H_4}$, particularly for A type zeolite, as Ag_{36}-A exhibited much smaller $n_{C_2H_4}$ than Ag_{62}-Y despite they had similar n_{Ag}.

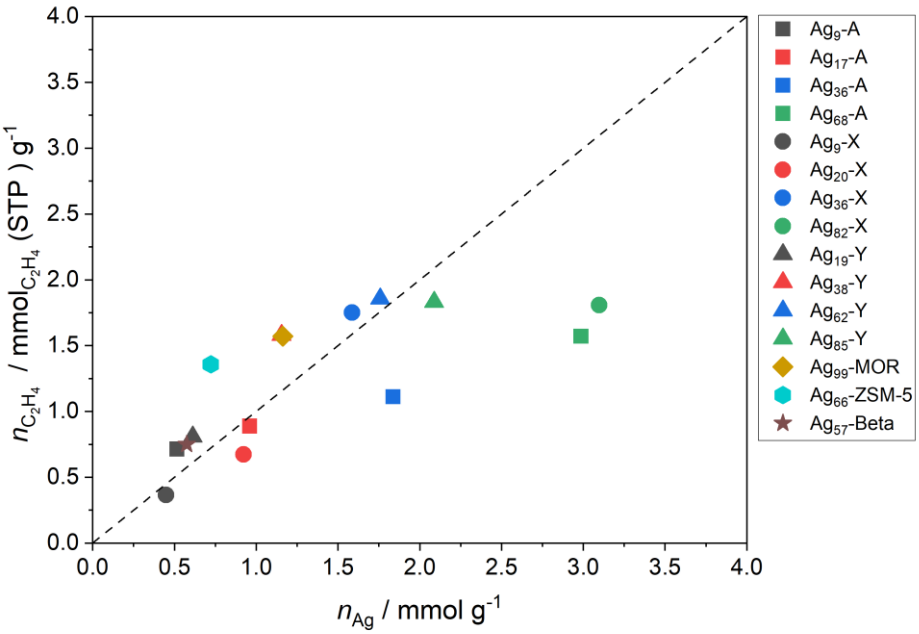

Figure 3-13. Relation between the C_2H_4 chemical adsorption capacity ($n_{C_2H_4}$) and Ag^+ content (n_{Ag}) for different Ag^+-zeolites.

3.4 Nature of Ag species in Ag ion-exchanged zeolites

A high adsorption capacity of C_2H_4 is an important characteristic required for solid materials that being utilized as C_2H_4 releasing materials to induce desired biological effects in a more efficient and cost-effective manner. The results in **Figure 3-13** revealed that Ag^+-exchanged X and Y zeolites with high adsorption capacity of C_2H_4 are promising for ethylene encapsulation. However, as mentioned above, it was observed that further increase in Ag^+ contents to give Ag_{82}-X and Ag_{85}-Y did not lead to increase in the amount of chemically adsorbed C_2H_4 when comparing to Ag^+-zeolites with low Ag content like Ag_{36}-X and Ag_{62}-Y. This observation suggested a complex relation between the Ag species present in Ag^+-zeolites and their role in acting as adsorption sites. Diffuse reflectance UV-vis spectra of the parent zeolites and Ag^+-zeolites were measured to characterize Ag species in Ag^+-zeolites. **Figure 3-14** shows the UV-vis spectra of parent zeolites and Ag^+-zeolites with different Ag contents. As depicted in the figure, Na^+-A and Na^+-X exhibited two absorption bands at around 240 and 320 nm, which can also be observed at around 220 and 300 nm for Na^+-Y, Na^+-MOR, Na^+-ZSM-5 and Na^+-Beta. These two bands are commonly observed for zeolites and attributed to the charge transfer from O^{2-} to Al^{3+} located at specific sites such as defects, corners, or surfaces.[30,31]

After the introduction of Ag^+, a new absorption peak at around 215 nm appeared for all the Ag^+-zeolites, which can be assigned to the electronic transition from $4d^{10}$ to the $4d^95s^1$ of highly dispersed Ag^+ that were coordinated with water molecules and with lattice oxygens.[32,33] Presence of the absorption peak at around 280 and 330 nm indicated the formation of small Ag_x^{n+} clusters ($x \leq 8$).[34–36] Slight differences were noted in the absorption peak at around 215 nm among the Ag zeolites with different framework structures. Typically, Ag^+-exchanged Y, ZSM-5, MOR and Beta, distinctly exhibited one absorption peak at 213 nm. Ag^+-exchanged A and X with low Ag contents also displayed absorption peaks at the same position, while with an increase in Ag contents, a new peak appeared and was located at a longer wavelength (around 230 nm) for Ag^+-exchanged A and X. Similar behavior was observed for Ag^+-A in a previous report. [31] These two absorption peaks (213 and around 230 nm) may represent for Ag^+ in different coordination states, where the absorption peak appeared at a longer wavelength was more plausibly the 8-membered ring coordinated Ag^+ ions, while that at 213 nm corresponds to 6-membered ring coordinated Ag^+ in the case of Ag^+-A.[30,37] An absorption peak around 400 nm was also observed for Ag^+-exchanged A and X, which was attributed the electronic transitions (ligand-to-metal charge-transfer transitions, LMCT) from the lone pairs of the oxygen atoms of the zeolite lattice to the empty 5s orbital of the Ag^+, responsible for the yellow color observed for Ag^+-exchanged A and X.[31] Recent research has assigned the absorption peaks at >400 nm mainly attributed to the large clusters or metallic Ag^0 nanoparticle.[34–36]

It should be pointed out that even though X and Y zeolites shared the same Faujasite topology

of framework structure, the Ag species in the corresponding Ag^+-exchanged zeolites presented in different natures even with similar Ag contents. Basically, the absorption peaks at around 320 and higher than 400 nm exhibited by Ag^+-X were not observed in Ag^+-Y, implying the different natures of Ag species in Ag^+-X and Ag^+-Y.

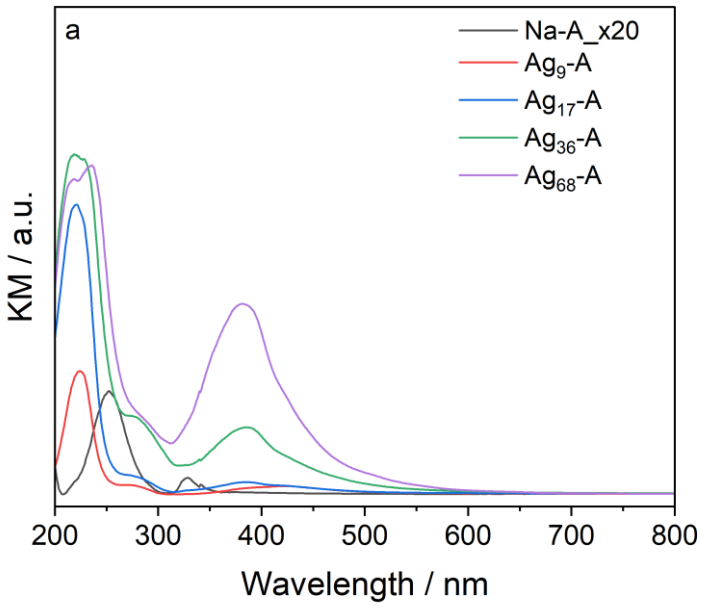

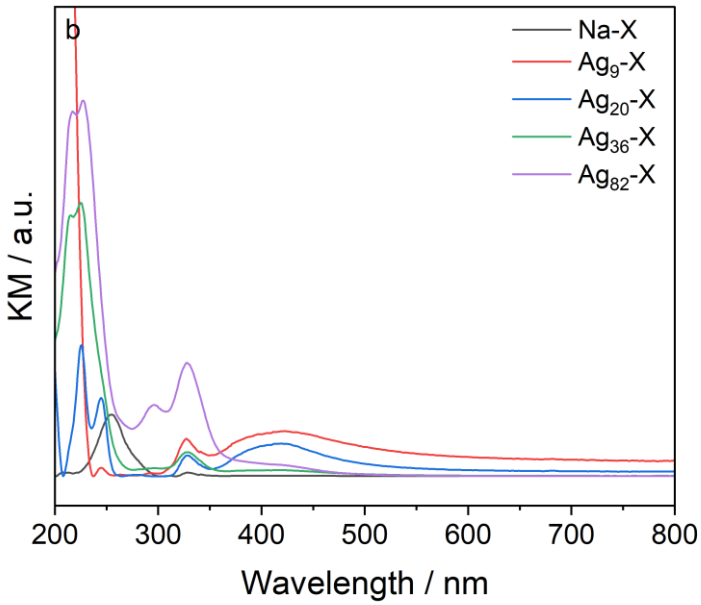

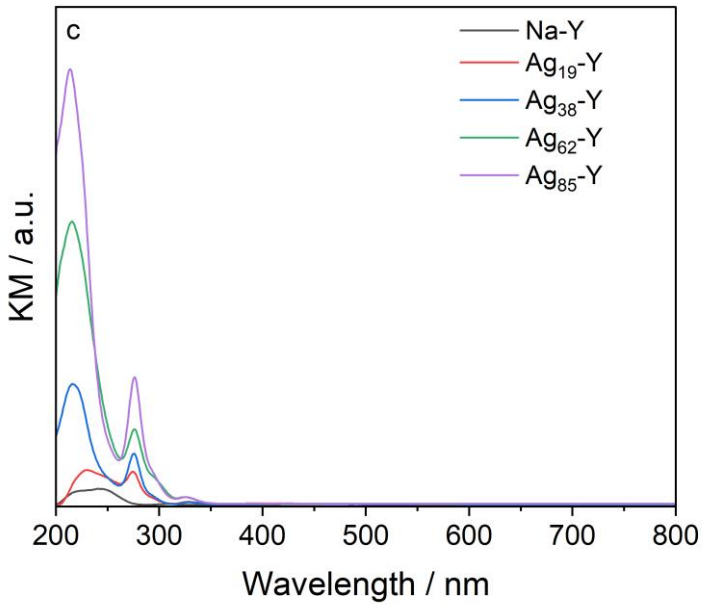
c
Na-Y
Ag19-Y
Ag38-Y
Ag62-Y
Ag85-Y
KM / a.u.
200
300
400
500
600
700
800
Wavelength / nm

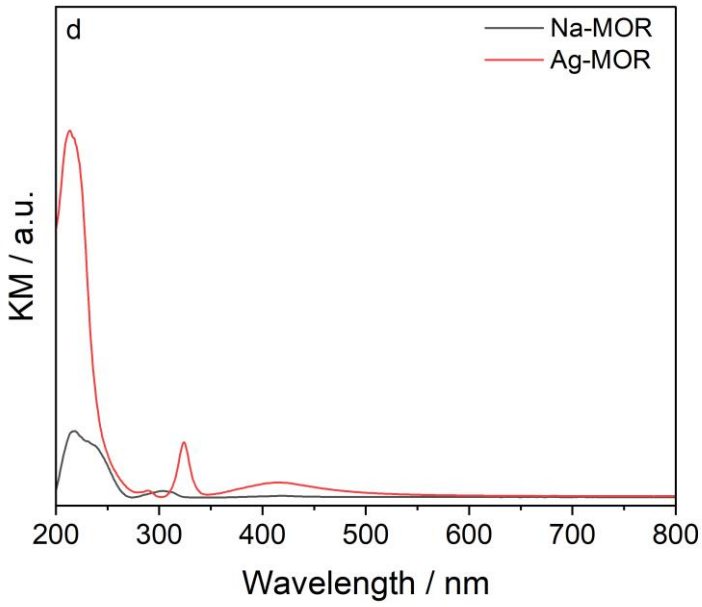
d
Na-MOR
Ag-MOR
KM / a.u.
200
300
400
500
600
700
800
Wavelength / nm

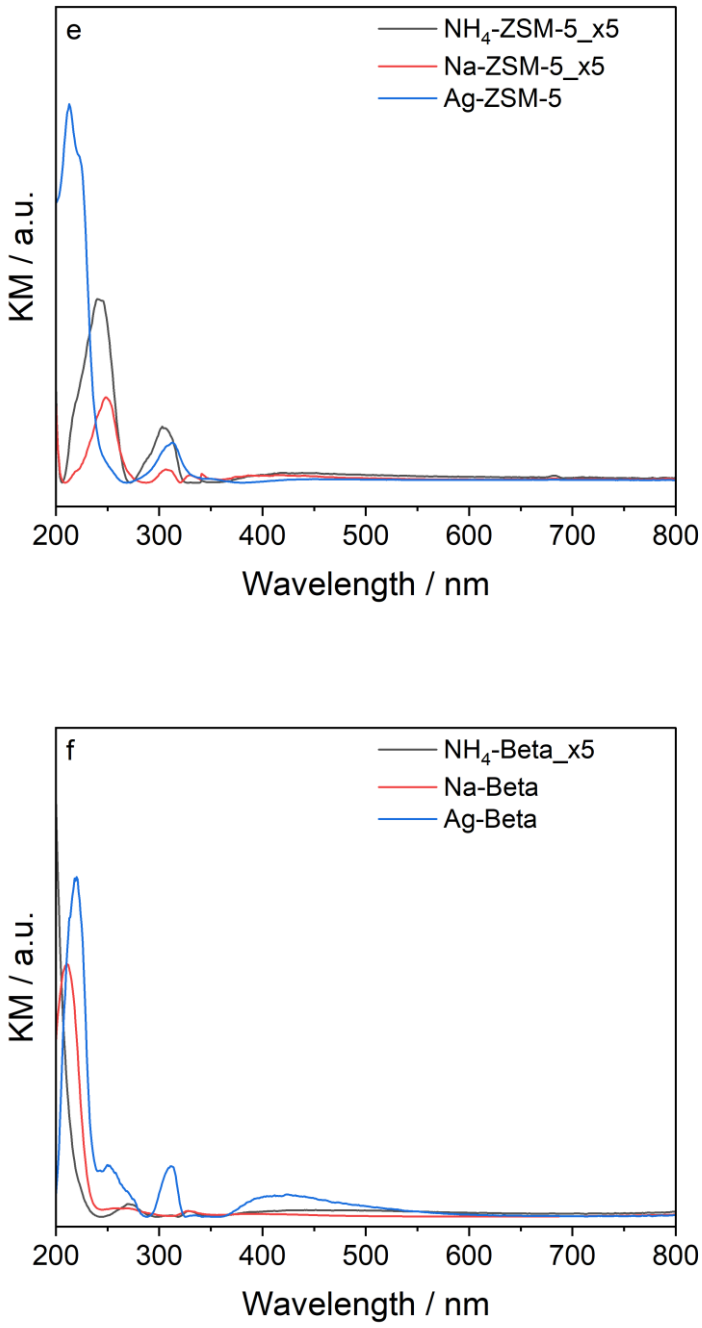

Figure 3-14. Diffuse reflectance UV-vis spectra for different parent zeolites and Ag^+-exchanged zeolites with different Ag^+ contents. All the spectra were collected at ambient atmospheres and 25 °C.

The local structures of Ag species in Ag^+-exchanged A, X and Y were further investigated by XAFS measurements. **Figure 3-15** shows the K-edge XANES and EXAFS transform spectra of Ag in Ag^+-zeolites. The K-edge XANES spectra of Ag in **Figure 3-15a** shows that all Ag^+-zeolites had Ag species with different valence states to Ag foil while very near to Ag in $AgNO_3$, suggesting that the valence states of Ag species in Ag-zeolites were cationic and almost mono valent, namely Ag^+. EXAFS Fourier transform spectra of Ag^+-exchanged zeolites in **Figure 3-15b** showed a distinct peak at 1.8 Å consistent with that of $AgNO_3$, indicating that this peak was contributed to Ag-O shell. An additional peak at around 2.8 Å was observed for Ag_{36}-A and Ag_{36}-X, which was slightly longer than that of Ag-Ag shell at 2.6 Å, displayed by the EXAFS Fourier transform of reference Ag foil. This peak was not observed in Ag_{62}-Y, which only showed one distinct peak at 1.8 Å. This result was correspondent to the UV-vis results that the Ag species present in Ag^+-Y were more homogeneous (mostly isolated Ag^+) than Ag^+-X and Ag^+-A (Ag clusters formation were suggested). Further effort of curve-fitting was performed but failed to elucidate the bond distance and coordination number of these bonds. Nevertheless, the Fourier transform spectra obtained in this study were similar to those in the previous report, suggesting that similar bonds could be present in these zeolites. The short Ag-O shell corresponds to the Ag^+-framework O contact, while the long Ag-O shell could arise from Ag clusters Ag_m^0-framework O bond.[38–41] Anyway, it was rather clear that the nature of Ag species present in Ag^+-Y was different with that in Ag^+-X. The different characters of the framework oxygens resulted from different Si/Al ratio of parent zeolite may affect charge transfer from oxygen to Ag^+, thus changing the nature of Ag species.

Overall, based on the characterization results shown above, it can be concluded that the framework structure as well as different characters of the framework oxygens due to different Si/Al ratios of the parent zeolite had a critical impact on the nature of Ag species in Ag^+-zeolites.

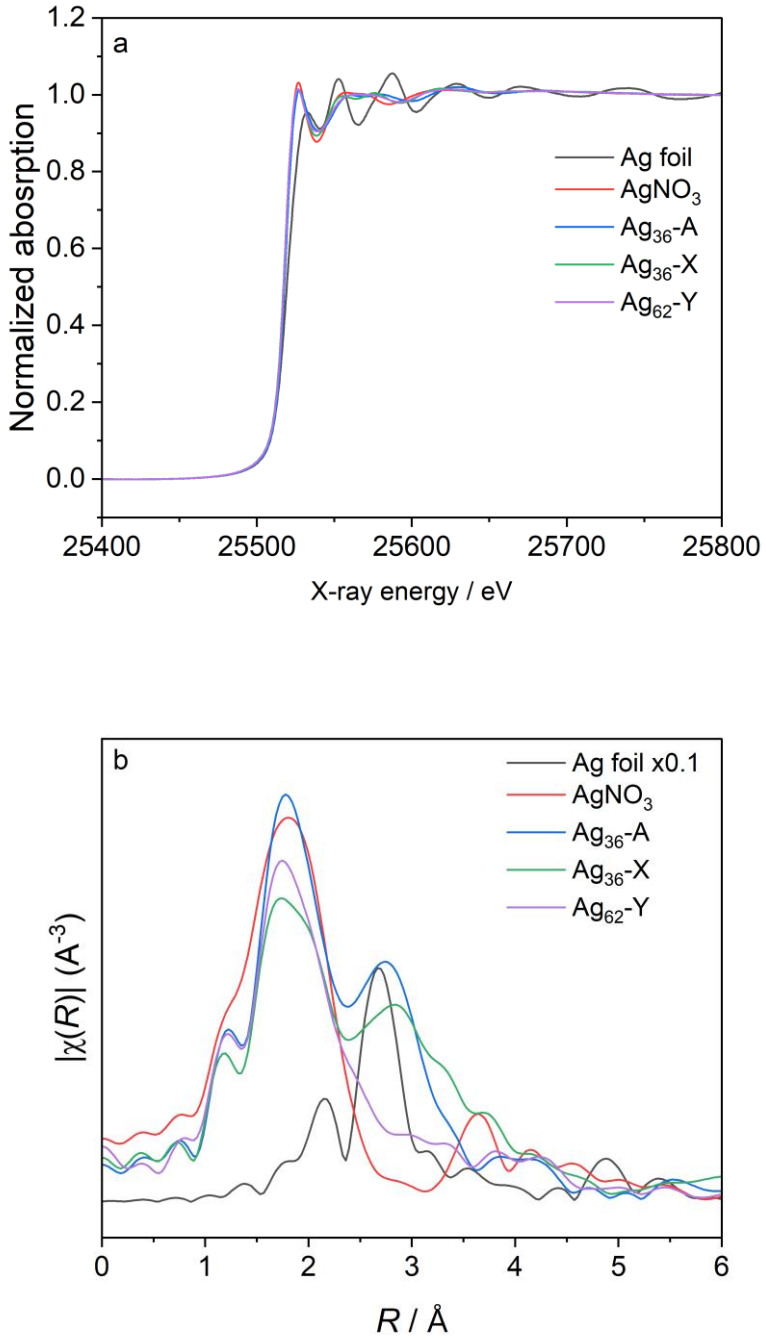

Figure 3-15. Ag K-edge (a) XANES spectra and (b) EXAFS Fourier transforms of Ag_{36}-A, Ag_{36}-X and Ag_{62}-Y, compared with Ag foil and $AgNO_3$ as references.

The effects of different treatments on the nature of Ag species were further investigated. **Figure 3-16** shows the diffuse reflectance UV-vis spectra of different Ag^+-zeolites under different treatments. Upon heating at 200 °C, the formation of Ag clusters was confirmed, as shown by the results depicted in **Figures 3-16a**, **b** and **c**. The treatments under H_2 flow at 50 °C evolved the absorption bands at 400 nm or more, as shown in **Figure 3-16d**, which were attributed to the formation of large Ag clusters or metallic Ag^0 nanoparticles.[34–36] Even mild treatments in H_2 flow, namely at 25 °C, caused the formation of these Ag species.

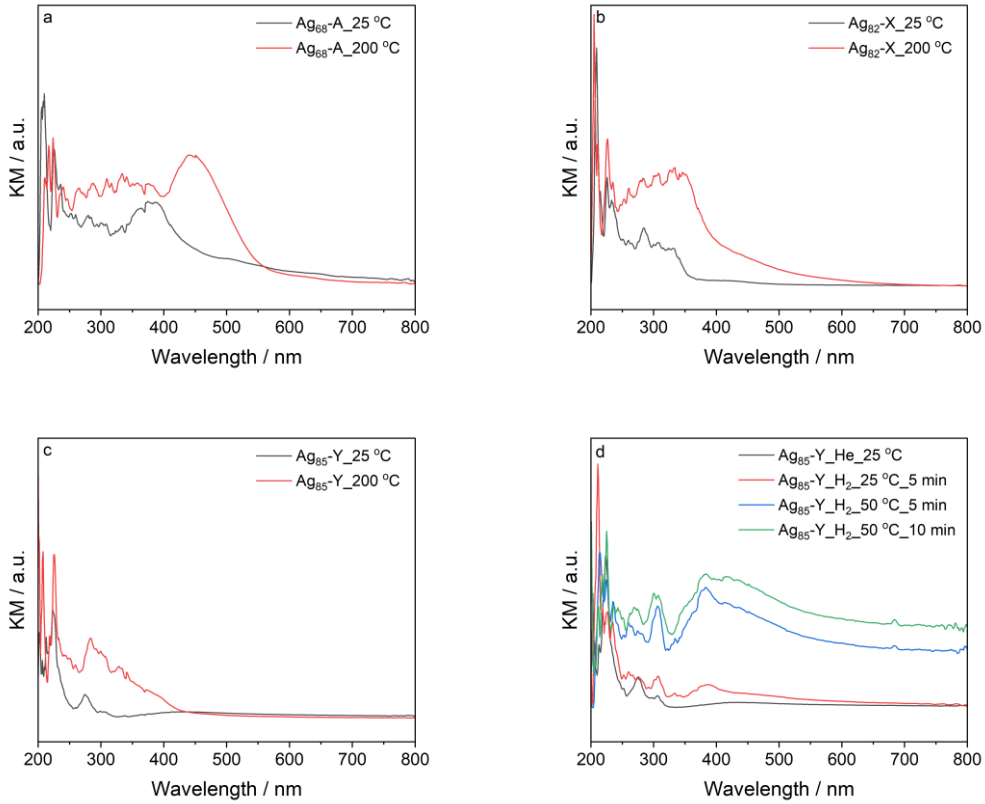

Figure 3-16. Diffuse reflectance UV-vis spectra of (a) Ag_{68}-A, (b) Ag_{82}-X and (c) Ag_{85}-Y at 25 °C and 200 °C under the flow of O_2/He. (d) Diffuse reflectance UV-vis spectra of Ag_{85}-Y collected at different temperatures and gas flows.

The effect of formation of large Ag clusters or metallic Ag^0 nanoparticles on C_2H_4 adsorption behavior was further investigated. Ag-zeolites activated in air flow at 200 °C with or without further reduction in H_2 flow were afforded for C_2H_4 adsorption measurements, and the results are presented in **Figure 3-17**. Decreases in C_2H_4 chemical adsorption amounts were confirmed for the samples treated subsequently in H_2 flow. This result combined with the diffuse reflectance UV-vis spectra depicted in **Figure 3-16d** suggested that the large Ag clusters or metallic Ag^0

nanoparticles did not act as the chemical adsorption sites for C_2H_4. It explains why although Ag_{36}-A had similar Ag contents with Ag_{62}-Y, the C_2H_4 adsorption capacity of the former one was only about the half of the latter one, as the Ag species in Ag_{36}-A dominantly presented as large Ag clusters or metallic Ag^0 nanoparticles.

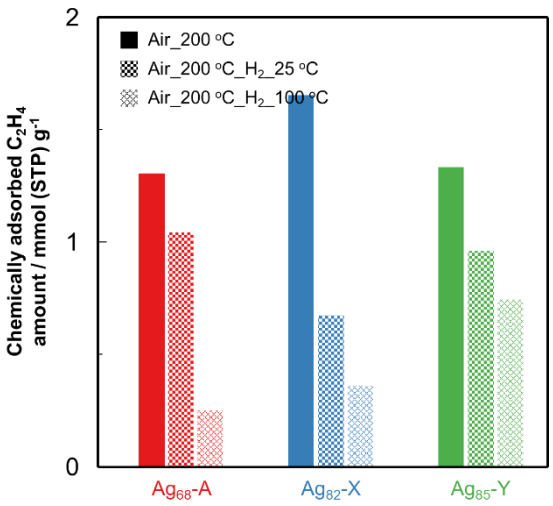

Figure 3-17. Amount of chemically adsorbed C_2H_4 for Ag^+-zeolites activated in air flow with or without subsequent H_2 reduction.

3.5 Adsorption strength evaluation

3.5.1 FTIR study

FTIR measurement is a useful method to investigate the adsorbate-adsorbent interaction strength. Here, FTIR studies were carried out by using C_2H_4 as probe molecules, trying to investigate the difference in adsorption strength between Ag species in different Ag^+-exchanged zeolites and adsorbed C_2H_4.

Figure 3-18 shows the spectra of adsorbed C_2H_4 over different Ag^+-zeolites. The intense absorption band at ca. 1650 cm^{-1} exhibited by Ag_{36}-A, Ag_{62}-X and Ag_{65}-Y was attributed to the H-O-H bending vibration band in water molecules. During heat treatment, the intensity of this band diminished significantly, while the intensity increased again during the cooling process, indicating the re-adsorption of water molecules and incomplete dehydration. After C_2H_4 adsorption followed by evacuation, the parent zeolites showed almost no difference with those after pretreatment, indicating that C_2H_4 was barely adsorbed on the parent zeolites after the evacuation. Differently, as shown in **Figure 3-18**, the absorption bands of C_2H_4 remained even after the evacuation for the Ag^+-exchanged zeolites, proving that C_2H_4 was strongly adsorbed on these samples, although the intensities of these bands were quite low. An absorption band at around 1580 cm^{-1} was observed, which was assigned to the ν_2 (C=C stretching) band.[17,42] The shift to lower frequency of wavenumber compared to gaseous C_2H_4 (1623 cm^{-1}), arises from the coordination bond between Ag^+ and C_2H_4. The shift of this C=C band provides valuable information that the strength of the coordination bond of C_2H_4 can be revealed by this shift, where the absorption band shifted to lower frequency of wavenumber indicated the stronger interaction strength.[17,42] The amount of shift decreased in order as Ag_{62}-Y (43 cm^{-1})> Ag_{66}-ZSM-5 (41 cm^{-1}) > Ag_{99}-MOR (38 cm^{-1}), thus, the overall strength of the interaction between C_2H_4 and Ag^+-zeolites were as Ag_{62}-Y > Ag_{66}-ZSM-5 > Ag_{99}-MOR. In addition to the band at 1580 cm^{-1}, an additional absorption band at 1571 cm^{-1} was also observed for Ag_{36}-X. The presence of two bands for Ag_{36}-X reveals that there were two different adsorption sites for C_2H_4. It was reported by Tarach et al. that in dehydrated Ag^+-X, two bands at 2184 and 2170 cm^{-1} were observed and assigned to CO molecules interacting with the Ag^+ cations in SII and SIII sites, respectively.[43] **Figure 3-19** shows a schematical illustration of different sites in which cations can be located in FAU zeolites. Correspondingly, the absorption band at 1580 and 1571 cm^{-1} thus were assigned to C_2H_4 adsorbed on Ag^+ cations located at SII and SIII sites, respectively. The absorption band (at 1571 cm^{-1}) demonstrated the strongest adsorption characteristic of C_2H_4 on Ag_{36}-X, comparing to C_2H_4 on other Ag^+-zeolites. Although in previous discussion on C_2H_4 adsorption isotherms, Ag_{36}-A also exhibited chemical adsorption of C_2H_4, it was noted that the absorption band for C=C stretching was not clearly observed in Ag_{36}-A, and the intensities of all the absorption bands exhibited by other Ag^+-zeolites were very low, which might be due to the low sensitivity of TGS detector.

Further confirmation using a MCT detector will be performed.

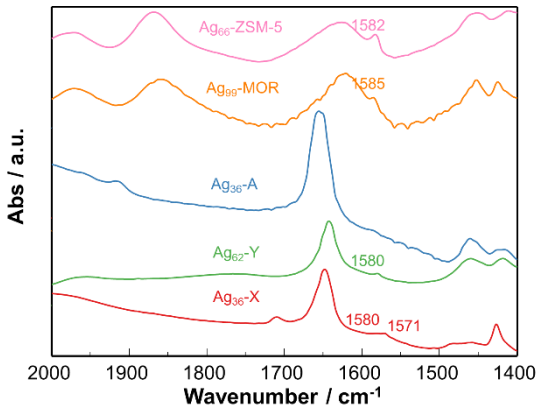

Figure 3-18. FTIR spectra of C_2H_4 adsorbed on Ag_{36}-X, Ag_{62}-Y, Ag_{36}-A, Ag_{99}-MOR and Ag_{56}-ZSM-5 at 25 °C.

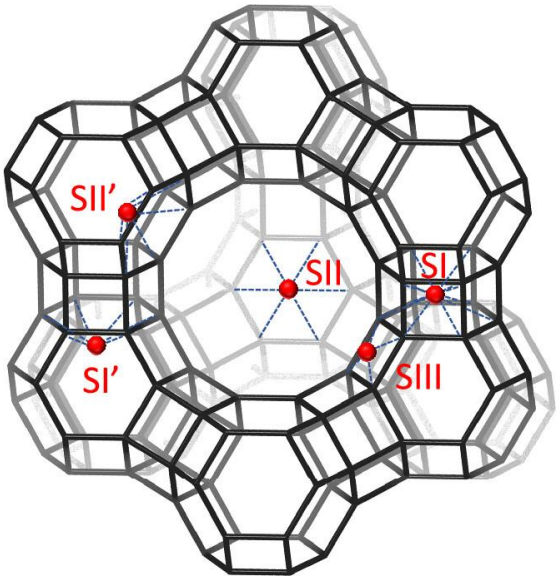

Figure 3-19. Sites of cations can be located in FAU zeolites.[44] SI is located in the center of the double 6 ring (D6R) cage; SI′ is located in the sodalite cage in front of the D6R; SII is located in the supercage in front of the 6MR of the sodalite cage; SII′ is located in the sodalite cage in front of the 6MR leading to the supercage; SIII is located in the supercage in front of one of the 4MRs of the supercage.

4. Conclusions

In this chapter, Ag^+-exchanged zeolites were prepared by a conventional ion-exchange process using zeolites with different topology framework structures and adsorption behavior of C_2H_4 was investigated. By carrying out C_2H_4 adsorption isotherm measurements, it was found that comparing with the Na^+-form zeolites, Ag^+-exchanged zeolites exhibited stronger interactions with C_2H_4, showing a typical Type I isotherm in C_2H_4 adsorption. Chemical adsorption of C_2H_4 that could not be easily removed by vacuum treatment was confirmed for all the Ag^+-exchanged zeolites, of which the amount can be estimated from the adsorption isotherms. The C_2H_4 chemical adsorption capacity basically increased with the increase in Ag^+ contents up to around 2 mmol g^{-1}. However, further increase in Ag^+ contents did not result in higher C_2H_4 chemical adsorption amounts. Spectroscopic investigation on the nature of Ag species in Ag-zeolites demonstrated that large clusters that did not act as adsorption sites for C_2H_4 were formed and became predominant when the Ag^+ contents exceeded 2 mmol g^{-1}. The framework structure as well as the Si/Al ratio of the zeolites had a critical impact on the nature of Ag species. Ag_{36}-X exhibited high adsorption capacity and strong adsorption strength of C_2H_4, making it promising C_2H_4 release materials.

5. References

(1) Saltveit, M. E. Effect of Ethylene on Quality of Fresh Fruits and Vegetables. *Postharvest Biol. Technol.* **1999**, *15* (3), 279–292. https://doi.org/10.1016/S0925-5214(98)00091-X.

(2) Barry, C. S.; Giovannoni, J. J. Ethylene and Fruit Ripening. *J. Plant Growth Regul*. **2007**, *26* (2), 143–159. https://doi.org/10.1007/s00344-007-9002-y.

(3) Keller, N.; Ducamp, M. N.; Robert, D.; Keller, V. Ethylene Removal and Fresh Product Storage: A Challenge at the Frontiers of Chemistry. Toward an Approach by Photocatalytic Oxidation. *Chem. Rev*. **2013**, *113* (7), 5029–5070. https://doi.org/10.1021/cr900398v.

(4) Wei, H.; Seidi, F.; Zhang, T.; Jin, Y.; Xiao, H. Ethylene Scavengers for the Preservation of Fruits and Vegetables: A Review. *Food Chem.* **2021**, *337*, 127750. https://doi.org/10.1016/J.FOODCHEM.2020.127750.

(5) Armitage, A. M. Promotion of Fruit Ripening of Ornamental Peppers by Ethephon. *HortScience* **1989**, *24* (6), 962-964. https://doi.org/10.21273/HORTSCI.24.6.962.

(6) El-Kereamy, A.; Chervin, C.; Roustan, J. P.; Cheynier, V.; Souquet, J. M.; Moutounet, M.; Raynal, J.; Ford, C.; Latché, A.; Pech, J. C.; Bouzayen, M. Exogenous Ethylene Stimulates the Long-Term Expression of Genes Related to Anthocyanin Biosynthesis in Grape Berries. *Physiol. Plant.* **2003**, *119* (2), 175–182. https://doi.org/10.1034/j.1399-3054.2003.00165.x.

(7) Ho, B. T.; Joyce, D. C.; Bhandari, B. R. Encapsulation of Ethylene Gas into α-Cyclodextrin and Characterisation of the Inclusion Complexes. *Food Chem.* **2011**, *127* (2), 572–580. https://doi.org/10.1016/J.FOODCHEM.2011.01.043.

(8) Ho, B. T.; Bhandari, B. R. Novel Solid Encapsulation of Ethylene Gas Using Amorphous α-Cyclodextrin and the Release Characteristics. *J. Agric. Food Chem.* **2016**, *64* (17), 3318–3323. https://doi.org/10.1021/acs.jafc.5b06037.

(9) Bazzano, M.; Barolo, C.; Buscaino, R.; D'Agostino, G.; Ferri, A.; Sangermano, M.; Pisano, R. Controlled Atmosphere in Food Packaging Using Ethylene-α-Cyclodextrin Inclusion Complexes Dispersed in Photocured Acrylic Films. *Ind. Eng. Chem. Res.* **2016**, *55* (3), 579–585. https://doi.org/10.1021/acs.iecr.5b03980.

(10) Shi, L.; Fu, X.; Tan, C. P.; Huang, Q.; Zhang, B. Encapsulation of Ethylene Gas into Granular Cold-Water-Soluble Starch: Structure and Release Kinetics. *J. Agric. Food Chem.* **2017**, *65* (10), 2189–2197. https://doi.org/10.1021/acs.jafc.6b05749.

(11) Ho, T. M.; Howes, T.; Bhandari, B. R. Encapsulation of CO_2 into Amorphous and Crystalline α-Cyclodextrin Powders and the Characterization of the Complexes Formed. *Food Chem.* **2015**, *187*, 407–415. https://doi.org/10.1016/J.FOODCHEM.2015.04.094.

(12) Zhou, J.; Zhang, Y.; Guo, X.; Zhang, A.; Fei, X. Removal of C_2H_4 from a CO_2 Stream by Using $AgNO_3$-Modified Y-Zeolites. *Ind. Eng. Chem. Res.* **2006**, *45* (18), 6236–6242.

https://doi.org/10.1021/ie0605478.

(13) Sarshar, Z.; Zahedi-Niaki, M. H.; Huang, Q.; Eić, M.; Kaliaguine, S. MTW Zeolites for Reducing Cold-Start Emissions of Automotive Exhaust. *Appl. Catal. B* **2009**, *87* (1–2), 37–45. https://doi.org/10.1016/j.apcatb.2008.08.025.

(14) Sue-aok, N.; Srithanratana, T.; Rangsriwatananon, K.; Hengrasmee, S. Study of Ethylene Adsorption on Zeolite NaY Modified with Group I Metal Ions. *Appl. Surf. Sci.* **2010**, *256* (12), 3997–4002. https://doi.org/10.1016/j.apsusc.2010.01.065.

(15) Aguado, S.; Bergeret, G.; Daniel, C.; Farrusseng, D. Absolute Molecular Sieve Separation of Ethylene/Ethane Mixtures with Silver Zeolite A. *J. Am. Chem. Soc.* **2012**, *134* (36), 14635–14637. https://doi.org/10.1021/ja305663k.

(16) Monzón, J. D.; Pereyra, A. M.; Gonzalez, M. R.; Legnoverde, M. S.; Moreno, M. S.; Gargiulo, N.; Peluso, A.; Aprea, P.; Caputo, D.; Basaldella, E. I. Ethylene Adsorption onto Thermally Treated AgA-Zeolite. *Appl. Surf. Sci.* **2021**, *542, 148748*. https://doi.org/10.1016/j.apsusc.2020.148748.

(17) Carter, J.L.; Yates, D. J. C.; Lucchesi, P. J.; Elliott, J. J.; Kevorkian, V. The Adsorption of Ethylene on a Series of Near-Faujasite Zeolites Studied by Infrared Spectroscopy and Calorimetry. *J. Phys.Chem*. **1965**, 70 (4), 1126-1136. https://doi.org/10.1021/j100876a026.

(18) Cisneros, L.; Gao, F.; Corma, A. Silver Nanocluster in Zeolites. ADSORPTION of ETHYLENE Traces for Fruit Preservation. *Microporous Mesoporous Mater.* **2019**, *283*, 25–30. https://doi.org/10.1016/j.micromeso.2019.03.032.

(19) Bereciartua, P. J.; Cantín, Á.; Corma, A.; Jordá, J. L.; Palomino, M.; Rey, F.; Valencia, S.; Corcoran, E. W.; Kortunov, P.; Ravikovitch, P. I.; Burton, A.; Yoon, C.; Wang, Y.; Paur, C.; Guzman, J.; Bishop, A. R.; Casty, G. L. Control of Zeolite Framework Flexibility and Pore Topology for Separation of Ethane and Ethylene. *Science* **2017**, 358 (6366), 1068-1071. https://doi.org 10.1126/science.aao0092.

(20) Ferreira, R.; Lopes, H.; Lourenço, J. P.; Silva, J. M.; João, I. M.; Ribeiro, M. F.; Fernandes, A. Ethylene Removal by Ag-Based ZSM-5 Adsorbents for the Preservation of Climacteric Fruits. *Microporous Mesoporous Mater.* **2024**, *370*, 113055. https://doi.org/10.1016/j.micromeso.2024.113055.

(21) Liu, C.; Xin, M.; Wang, C.; Zhao, W.; Xiang, Y.; Zhang, X.; Qiu, L.; Xu, G. Ag_2O Nanoparticles Encapsulated in Ag-Exchanged LTA Zeolites for Highly Selective Separation of Ethylene/Ethane. *ACS Appl. Nano Mater.* **2023**, *6* (7), 5374–5383. https://doi.org/10.1021/acsanm.2c05296.

(22) Treacy, M. M. and Newsam, J. M. Two New Three-Dimensional Twelve-Ring Zeolite Frameworks of Which Zeolite Beta is a Disordered Intergrowth. *Nature* **1988**, *332* (17), 249-251. https://doi.org/10.1038/332249a0.

(23) Cantín, Á.; Corma, A.; Díaz-Cabañas, M. J.; Jordá, J. L.; Moliner, M.; Rey, F. Synthesis and Characterization of the All-Silica Pure Polymorph C and an Enriched Polymorph B Intergrowth of Zeolite Beta. *Angew. Chem. Int. Ed.* **2006**, *45* (47), 8013–8015. https://doi.org/10.1002/anie.200603027.

(24) Lu, T.; Yan, W.; Xu, R. Chiral Zeolite Beta: Structure, Synthesis, and Application. *Inorg. Chem. Front*. **2019**, 6, 1938–1951. https://doi.org/10.1039/c9qi00574a.

(25) Fonseca, A. M.; Neves, I. C. Study of Silver Species Stabilized in Different Microporous Zeolites. *Microporous Mesoporous Mater.* **2013**, *181*, 83–87. https://doi.org/10.1016/J.MICROMESO.2013.07.018.

(26) Yu, J.; Ye, S.; Shi, Y.; Liao, H.; Wang, D. Thermally Formation and Luminescent Performance of Silver Nanoclusters Confined within LTA Zeolites. *J. Alloys Compd.* **2021**, *857*, 157614. https://doi.org/10.1016/J.JALLCOM.2020.157614.

(27) Sakai, M.; Sasaki, Y.; Tomono, T.; Seshimo, M.; Matsukata, M. Olefin Selective Ag-Exchanged X-Type Zeolite Membrane for Propylene/Propane and Ethylene/Ethane Separation. *ACS Appl. Mater. Interfaces* **2019**, *11* (4), 4145–4151. https://doi.org/10.1021/acsami.8b20151.

(28) Pires, J.; Carvalho, M. B. de; Ribeiro, F. R.; Derouane, E. G. Textural Characteristics of Y and ZSM-20 Zeolites Determined by Nitrogen Adsorptions. *Zeolites* **1991**, *11* (4), 345–348. https://doi.org/10.1016/0144-2449(91)80298-E.

(29) Chen, N. Y. Hydrophobic Properties of Zeolites. *J. Phys. Chem*. **1976**, *80*, 60-63. https://doi.org/10.1021/j100542a013.

(30) Garbowski1, E. D.; Mirodatos, C. Investigation of Structural Charge Transfer in Zeolites by Ultraviolet Spectroscopy. *J. Phys. Chem*. **1982**, *86*, 97-102. https://doi.org/10.1021/j100390a019.

(31) Seifert, R.; Kunzmann, A.; Calzaferri, G. The Yellow Color of Silver-Containing Zeolite A. *Angew. Chem. Int. Ed.* **1998**, *37* (11), 1521–1524. https://doi.org/10.1002/(sici)1521-3773(19980619)37:11<1521::aid-anie1521>3.0.co;2-v.

(32) Texter, J.; Hastrelter, J. J.; Hall, J. L. Spectroscopic Confirmation of the Tetrahedral Geometry of $Ag(H_2O)_4^+$. *J. Phys. Chem*. **1983**, *87*, 4690-4693. https://doi.org/10.1021/j100246a029.

(33) Bethke, K. A.; Kung, H. H. Supported Ag Catalysts for the Lean Reduction of NO with C_3H_6. *J. Catal.* **1997**, *172* (1), 93–102. https://doi.org/10.1006/JCAT.1997.1794.

(34) Shibata, J.; Takada, Y.; Shichi, A.; Satokawa, S.; Satsuma, A.; Hattori, T. Ag Cluster as Active Species for SCR of NO by Propane in the Presence of Hydrogen over Ag-MFI. *J. Catal.* **2004**, *222* (2), 368–376. https://doi.org/10.1016/J.JCAT.2003.11.007.

(35) Wichterlová, B.; Sazama, P.; Breen, J. P.; Burch, R.; Hill, C. J.; Čapek, L.; Sobalík, Z. An in situ UV–Vis and FTIR Spectroscopy Study of the Effect of H_2 and CO during the Selective Catalytic Reduction of Nitrogen Oxides over a Silver Alumina Catalyst. *J. Catal.* **2005**, *235* (1), 195–200. https://doi.org/10.1016/J.JCAT.2005.08.006.

(36) Shimizu, K. I.; Sugino, K.; Kato, K.; Yokota, S.; Okumura, K.; Satsuma, A. Formation and Redispersion of Silver Clusters in Ag-MFI Zeolite as Investigated by Time-Resolved QXAFS and UV-Vis. *J. Phy. Chem. C* **2007**, *111* (4), 1683–1688. https://doi.org/10.1021/jp066995a.

(37) Gellens, L. R.; Smith, J. V; Pluth, J. J. Crystal Structure of Vacuum-Dehydrated Silver Hydrogen

Zeolite A. *J. Am. Chem. Soc.* **1983**, *105* (1), 51-55. https://pubs.acs.org/sharingguidelines.

(38) Miyanaga, T.; Hoshino, H.; Endo, H. Local Structure of Silver Clusters in the Channels of Zeolite 4A. *J. Synchrotron Rad*. **2001**, *8*, 557-559. https://doi.org/10.1107/S0909049500012668.

(39) Suzuki, Y.; Matsumoto, N.; Ainai, T.; Miyanaga, T.; Hoshino, H. In Situ Infrared and EXAFS Studies of an Ag Cluster in Zeolite X. *Polyhedron* **2005**, *24* (5), 685–691. https://doi.org/10.1016/j.poly.2005.01.009.

(40) Suzuki, Y.; Miyanaga, T.; Hoshino, H.; Matsumoto, N.; Ainai, T. In-Situ XAFS Study of Ag Clusters in Zeolite 4A. *Phys. Scr.* **2005**, *115*, 765-768. https://doi.org/10.1238/Physica.Topical.115a00765.

(41) Miyanaga, T.; Suzuki, Y.; Matsumoto, N.; Narita, S.; Ainai, T.; Hoshino, H. Formation of Ag Clusters in Zeolite X Studied by in Situ EXAFS and Infrared Spectroscopy. *Microporous Mesoporous Mater.* **2013**, *168*, 213–220. https://doi.org/10.1016/j.micromeso.2012.09.013.

(42) Huang, Y.-Y. Ethylene Complexes in Copper(l) and Silver (I) Y Zeolites. *J. Catal*. **1980**, *61* (2), 461-476. https://doi.org/10.1016/0021-9517(80)90393-0.

(43) Tarach, K.; Góra-Marek, K.; Chrzan, M.; Walas, S. Quantification of Silver Sites in Zeolites: Carbon Monoxide Sorption Monitored by IR Spectroscopy. *J. Phys. Chem. C* **2014**, *118* (41), 23751–23760. https://doi.org/10.1021/jp506820v.

(44) Boer, D. G.; Langerak, J.; Pescarmona, P. P. Zeolites as Selective Adsorbents for CO_2 Separation. *ACS Appl. Energy Mater*. **2023**, *6* (5) 2634–2656. https://doi.org/10.1021/acsaem.2c03605.

Chapter 4

Evaluation of ethylene release over Ag^{+}-exchanged zeolite

1. Introduction

As mentioned in Chapter 3, C_2H_4 is often detrimental to the fruits and vegetables in the postharvest process,[1,2] thus the development of solid materials on C_2H_4 focuses more on the adsorptive removal and catalytic combustion of C_2H_4 from the space. However, C_2H_4 also has beneficial effects on triggering ripening as well as color development for fruits and vegetables.[3,4] The encapsulation of C_2H_4 into solid matrix enables easier handling for the subsequent application.

Apart from the adsorption characteristics, the subsequent release characteristics of C_2H_4 from the solid matrix are also vital for the real application. Controlled release is important in developing technology of release material, where the encapsulated actives (also called as active ingredients, which are compounds have certain functions) are expected to release at appropriate time with knowing or desired releasing rate in given environment. The controlled release of encapsulated actives has been extensively investigated in food and pharmaceutical industry. It can be realized with exogenous factors such as the physicochemical properties of the encapsulated actives and their carriers, as well as exogenous stimuli including pH or temperature change, humidity, and light. The controlled release of the actives can be immediate, delayed, prolonged or in a modified way.

Although Ag^+-exchanged zeolites have been widely studied for C_2H_4 adsorption, the releasing characteristics have been rarely investigated, which are considered to play an important role in application as C_2H_4 release material. In Chapter 3, the adsorption behavior of C_2H_4 over different parent and Ag^+-exchanged zeolites has been comprehensively investigated. As a result, it was found that Ag-X exhibited rather high C_2H_4 encapsulation capacity as well as strong interaction with C_2H_4, making it good candidate as C_2H_4 release material. The releasing characteristics of C_2H_4 over this Ag-zeolite compared with others were further investigated in this chapter to give guideline for development of high performance C_2H_4 release materials. Thereafter, the release behavior of C_2H_4 from the selected Ag^+-zeolite and the effect of released C_2H_4 on potato sprouting were investigated.

2. Experiment

2.1 Materials

The materials used in this chapter were the same as those in Chapter 3.

2.2 C_2H_4-TPD measurement

Temperature-programmed desorption of C_2H_4 (C_2H_4-TPD) was carried out on a home-made device with helium as a carrier gas. The gas at the outlet of the reactor was continuously monitored by a quadrupole mass spectrometer (Q-MS, M-QA100F, Canon Anelva Corp.). Typically, ca. 100 mg of sample was placed in a glass reactor, and it was heated to and maintained at 200 °C in He flow (25 mL min^{-1}) for 1 h. After that, the reactor was cooled down to 25 °C, and the gas was changed to C_2H_4 (10 mL min^{-1}) and was steadily flown for 1 h for adsorption of C_2H_4. After the adsorption, the reactor was purged with He (50 mL min^{-1}) for 30 min to remove the gas phase and physically adsorbed C_2H_4, while the outlet gas was monitored using the Q-MS. After confirming that the signal due to C_2H_4 (m/z = 27) became steady, the reactor was heated to 400 °C at a heating rate of 10 °C min^{-1} in He flow, while the outlet gas was continuously monitored by the Q-MS.

2.3 Dynamic C_2H_4 release

The dynamic release of C_2H_4 from zeolites was investigated under N_2 flow with an apparatus shown in **Figure 4-1**. Basically, in each experiment, ca. 100 mg of the sample was placed into a glass tube and was pretreated at 200 °C in N_2 flow (25 mL min^{-1}) for 1 h. After cooling down to 25 °C, the gas was switched to C_2H_4 (10 mL min^{-1}) and left it for 30 min, allowing for equilibrium C_2H_4 adsorption. Subsequently, the C_2H_4 flow was switched to N_2 (10 min^{-1}), and release of C_2H_4 from the sample was monitored by a gas chromatograph equipped with a frame ionization detector (GC-FID, Shimazu).

The dynamic release experiment in the presence of water vapor was also performed. N_2 was flown into a container containing liquid H_2O, and N_2 with saturated H_2O vapor was then fed into the glass tube for release experiment. Different relative humidities (RH) were controlled by mixing dry N_2 flow with that containing H_2O vapor, while the total N_2 flow rate was fixed at 10 mL min^{-1}.

A blank test was also conducted without zeolites in the tube to eliminate the effect of quantification of C_2H_4 release amount that caused by the residual C_2H_4 in dead volume of the glass tube and gas line. The procedure was the same as those described above but without zeolites.

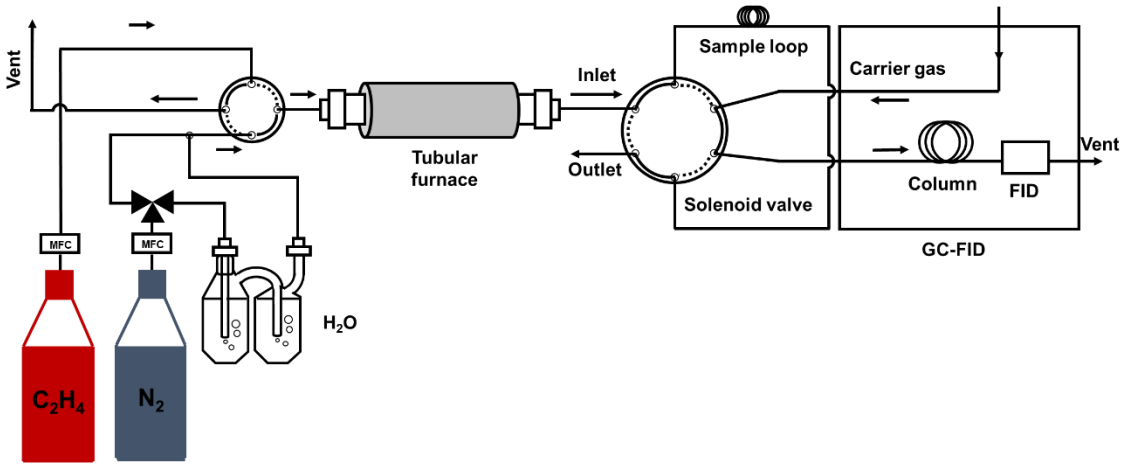

Figure 4-1. Experimental setup for dynamic ethylene release.

Kinetic analysis was performed using the results of dynamic C_2H_4 release measurements. According to the quantified concentration of released C_2H_4, the ratio of C_2H_4 release (X) was defined as eq. (1),

$$X = q_t / q_e \qquad \text{eq. (1)}$$

where, q_t, and q_e represent the C_2H_4 release amount from the sample at time t, and the C_2H_4 adsorption capacity, respectively.

An Avrami equation developed from Avrami's kinetic model was applied to describe the C_2H_4 release as follows,

$$X = 1 - \exp(-kt^n) \qquad \text{eq. (2)}$$

where, k and n represent the release constant and the Avrami exponent, respectively. The Avrami model was initially proposed to describe the kinetics of phase transition and crystallization,[5] but it has also been proposed to describe the gas release from inclusion complex as well as the sorption of CO_2 on amine-functionalized adsorbents with excellent results.[6–14] These results make the model attractive for the kinetic analysis in this work. The Avrami exponent reflects the complexity of release mechanism, including diffusion through the solid matrix or desorption from the solid surface via physical or/and chemical desorption.[8–10] An eq. (3) thus can be derived from eq. (2),

$$\ln[-\ln(1 - X)] = \ln k + n\ln t \qquad \text{eq. (3)}$$

Accordingly, a linear plot of $\ln[-\ln(1-X)]$ versus $\ln t$ allows to determine the release constant k and the Avrami exponent n from the intercept and slope, respectively.

For comparison, a pseudo-first-order kinetic model was also applied for data fitting using eq. (4),

$$q_t = q_e(1-\exp(-kt) \qquad \text{eq. (4)}$$

2.4 C_2H_4 release and effect on potato sprouting

Ag_{36}-X (2 g) was added into a glass tube, where glass wool and $CaCl_2$ (1 g) were further added on the top of Ag_{36}-X. $CaCl_2$ was added in order to capture water molecules to extend the release time of C_2H_4. The glass tube was evacuated and heated to 200 °C for 1 h as the pretreatment. After cooling down to room temperature, C_2H_4 was flown into the glass tube for adsorption. After adsorption equilibrium, the glass tube was evacuated for 2 min to remove the C_2H_4 in the gas phase. Thereafter, the glass tube was placed into a film package (P-Plus®) with 6 potatoes and sealed. The potatoes were pre-stored in dark room at 4 °C until use for the test. The film package was then placed in a dark room under constant temperature (18 °C). Gas sample of 1 mL was taken using a gas tight syringe for GC-FID analysis to measure the concentration of C_2H_4 in the package. The sprouting of potatoes was also recorded by photographs. Potatoes without Ag^+-zeolite and potatoes with gaseous C_2H_4 (80 mL) addition were also prepared in other film packages for comparison.

3. Results and discussion

3.1 C_2H_4-TPD measurement

Temperature programmed desorption (TPD) is a technique used to observe the desorption process of molecules that adsorbed on solid materials. Basically, a TPD profile provides valuable information about adsorbed species and adsorption sites. The strength of chemical bonds can be obtained from the desorption temperature, and the number of adsorption site from the desorption amount. The number of adsorption sites can be obtained from the desorption temperature and the desorption volume. Here, C_2H_4-TPD was conducted to get the information of the adsorption sites present on Ag^+-exchanged zeolites, the results are shown in **Figure 4-2**. As depicted in **Figure 4-2a**, the increase in the signal intensity (m/z = 27) corresponding to C_2H_4 desorption was observed just after the temperature increase from 25 °C. A large desorption peak was observed for Ag_{68}-A and Ag_{82}-X at low temperature. The ability to release C_2H_4 at lower temperatures, ideally near room temperature, is advantageous as it facilitates easier handling of C_2H_4 release materials.

An exceptional desorption peak at high temperature was observed for Ag_{19}-Beta that prepared from a NH_4^+-form Beta. This unusual desorption peak at high temperature raised concerns about potential oligomerization of C_2H_4 occurring over this material. The C_2H_4-TPD profiles of the parent NH_4^+-form Beta, as shown in **Figure 4-2b**, confirmed the presence of signal of m/z = 43 and 56, attributed to the fragments of propene and butene, respectively. Surprisingly, these desorption peaks were observed even without the C_2H_4 adsorption process (**Figure 4-2c**), indicating that some organic compounds remaining in the parent NH_4-Beta, possibly template reagents used during the synthesis of parent NH_4^+-Beta.

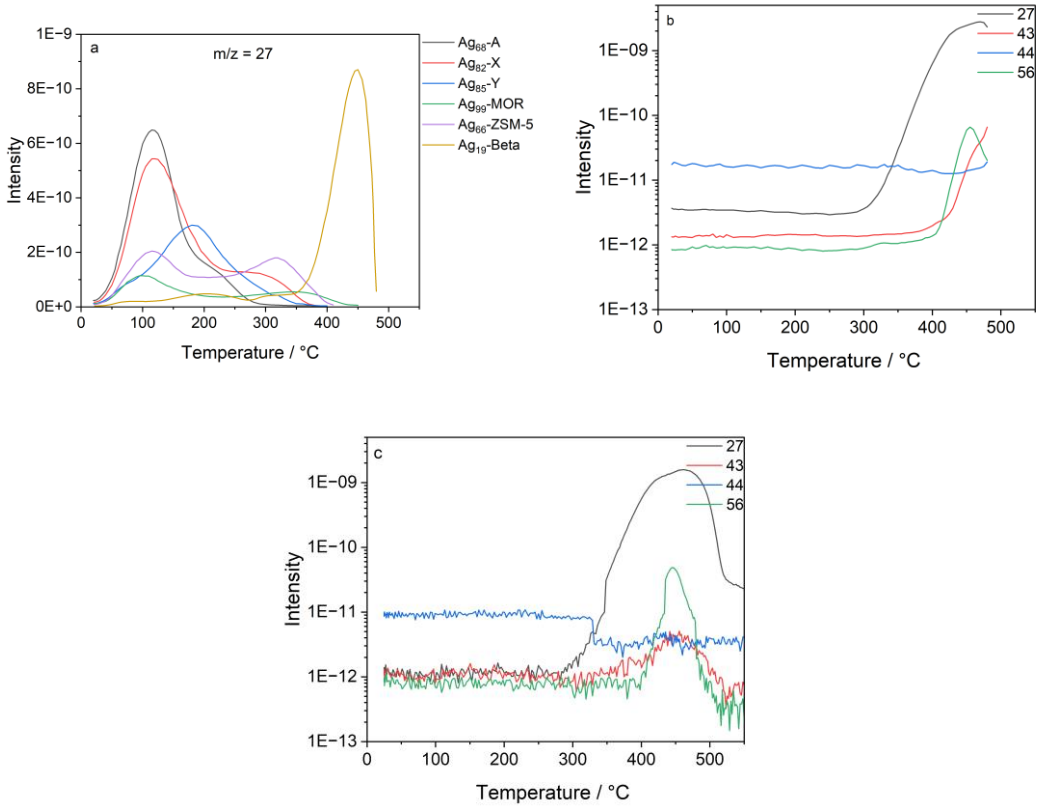

Figure 4-2. C_2H_4-TPD profiles for (a) different Ag^+-zeolites and (b) NH_4^+-Beta. After C_2H_4 adsorption, He flow was introduced to remove the gaseous C_2H_4 and weakly adsorbed C_2H_4, thereafter the samples were heated in He flow for TPD profiles collection. (c) TPD profiles for NH_4^+-Beta without C_2H_4 adsorption.

Subsequently, NH_4-Beta was calcined at 550 °C in air to transform it into the corresponding H^+-form zeolite. C_2H_4 was then adsorbed on this H^+-Beta sample, and a C_2H_4-TPD profile was measured. **Figure 4-3** shows TPD profiles for different H^+-zeolites. As shown in **Figure 4-3a**, it was found that the large desorption peak at temperatures higher than 400 °C observed for NH_4^+-Beta disappeared for H^+-Beta sample. Instead, two new peaks appeared at around 200 and 300 °C. Similar peaks were also observed in H^+-ZSM-5 and H^+-Y zeolites, as shown in **Figure 4-3b** and **c**. Oligomerization of C_2H_4 has been reported to proceed over the Brønsted acid sites of zeolites. It was reported that surface alkylation and polymerization of C_2H_4 occurred over H^+-ZSM-5 even around or below room temperature.[15,16] Based on these results, it was concluded that NH_4^+-Beta and the H^+-form zeolites were unsuitable as a C_2H_4 release material and thus no further study was made for these samples.

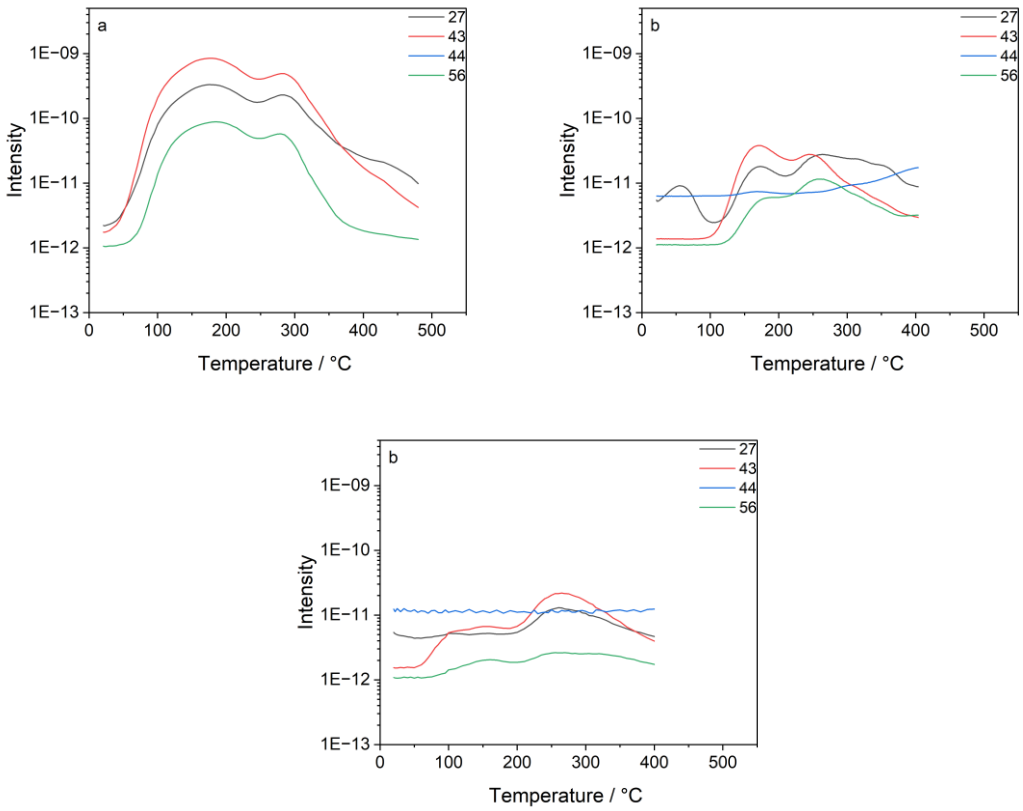

Figure 4-3. C_2H_4-TPD profiles for (a) H^+-Beta, (b) H^+-ZSM-5 and (c) H^+-Y.

To minimize (ideally eliminate) the influence of protons in the zeolites on the adsorption and desorption of C_2H_4, Na-form zeolites were used for Ag^+-exchange reaction, and those after Ag^+-exchange reaction were provided for C_2H_4-TPD measurements. **Figure 4-4** shows the TPD profiles for different Na^+-form zeolites. The Q-MS signals corresponding to propene or butene desorption were not observed for the Na^+-form zeolites during the C_2H_4-TPD measurements. However, peaks indicating C_2H_4 desorption were observed for Na^+-A and Na^+-X zeolites. It is noteworthy that these peaks may not correspond to chemically adsorbed C_2H_4, as no chemical adsorption of C_2H_4 was observed for Na^+-form zeolites, suggested by the results of C_2H_4 adsorption isotherm measurements presented in Chapter 3.

Indeed, during purging with He after C_2H_4 adsorption and before the C_2H_4-TPD measurements, the Q-MS signal of C_2H_4 decreased continuously throughout the time in purge process and did not become a stable value for several hours, especially for Na^+-A. This indicated that weakly adsorbed C_2H_4 was continuously desorbed from Na^+-A.

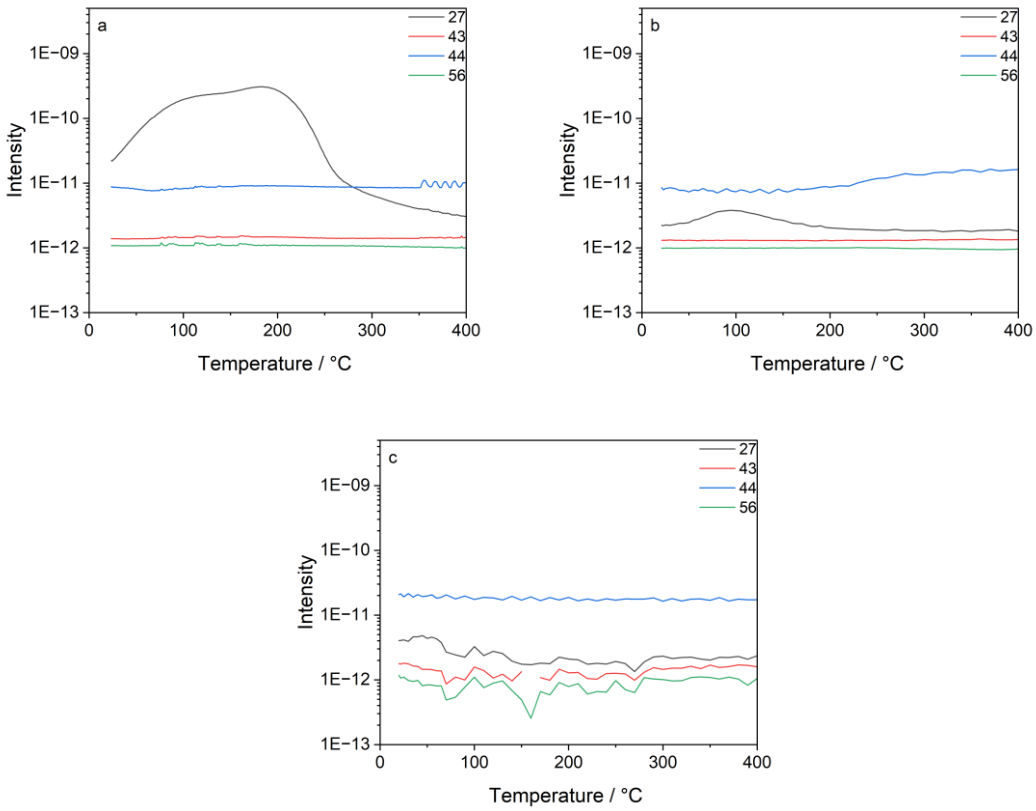

Figure 4-4. C_2H_4-TPD profiles for (a) Na^+-A, (b) Na^+-X and (c) Na^+-Y.

Figure 4-5 shows the TPD profiles for different Ag^+-zeolites. Similar to Na^+-form zeolites, there was also no signal corresponding to desorption of propene or butene observed for Ag_{68}-A, Ag_{82}-X and Ag_{85}-Y. However, desorption of C_2H_4 was confirmed, suggesting that oligomerization of the adsorbed C_2H_4 did not occur in these Ag^+-zeolites, and C_2H_4 desorbed at relatively low temperatures from these Ag^+-zeolites.

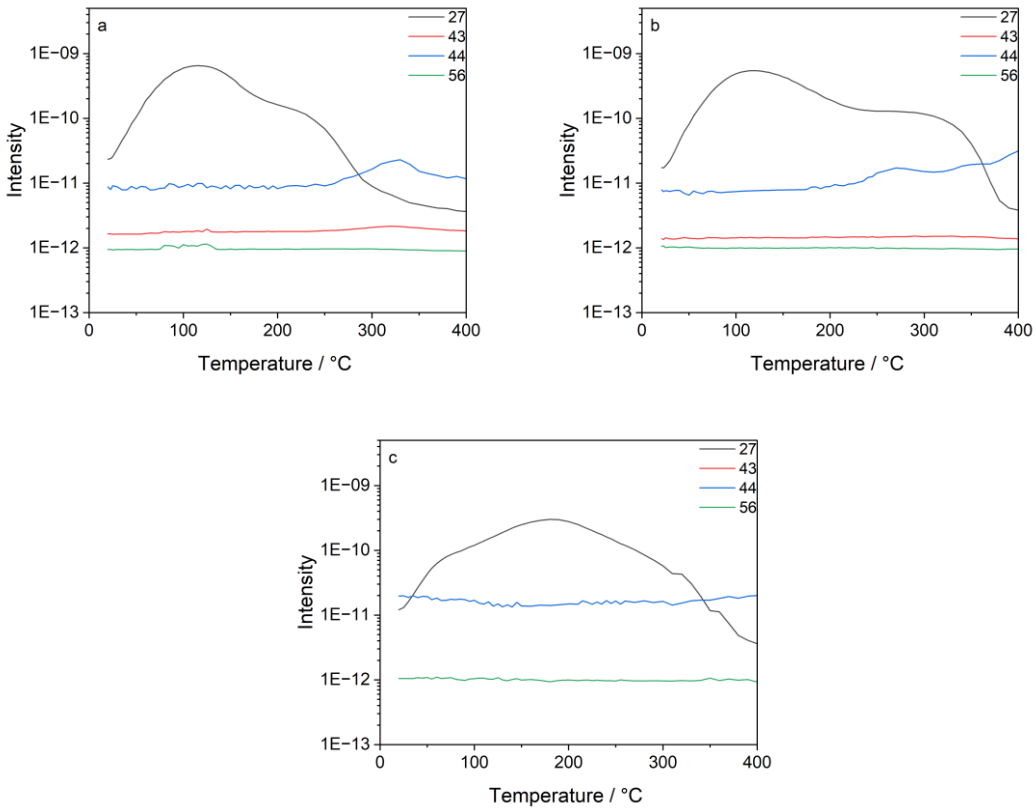

Figure 4-5. C_2H_4-TPD profiles for (a) Ag_{68}-A, (b) Ag_{82}-X and (c) Ag_{85}-Y.

The C_2H_4-TPD profiles for Ag_{36}-A, Ag_{36}-X and Ag_{62}-Y shown in **Figure 4-6** revealed the presence of C_2H_4 adsorption sites with different adsorption strength in these Ag^+-zeolites. They all exhibited two desorption peaks at around 70 and 160 °C. Given that the diffuse reflectance UV-vis spectra for Ag_{62}-Y revealed that two kinds of Ag species, i.e., Ag^+ and small Ag_x^{n+} clusters ($0<x\leq4$), these two desorption peaks were attributed to the C_2H_4 adsorbed on these two different Ag species. Compared to Ag_{62}-Y, Ag_{36}-X and Ag_{36}-A exhibited larger fraction of C_2H_4 desorption with weak interaction (i.e. larger fraction of peak area to total peak areas for the peak at ca. 70 °C). Ag_{36}-X exhibited another desorption peak at higher temperature of 270 °C, which demonstrated the strong interaction between the adsorbed C_2H_4 and the Ag species. It was attributed to the C_2H_4 strongly adsorbed on the Ag^+ located at SIII sites. It is consistent with the FTIR results that an absorption band with a large shift was observed for Ag_{36}-X.

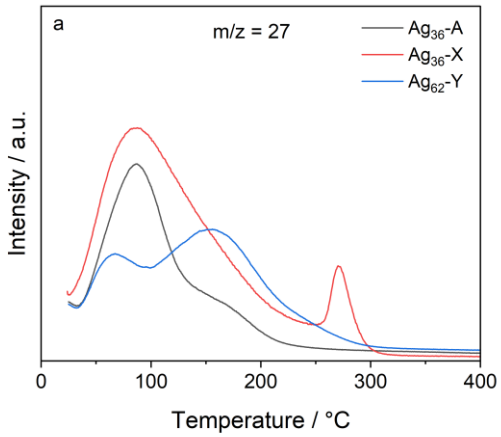

Figure 4-6. C_2H_4-TPD profiles for Ag_{36}-A, Ag_{36}-X and Ag_{62}-Y.

3.2 Dynamic C_2H_4 release and kinetic analysis

The time courses of C_2H_4 release from different Ag^+-zeolites at 25 °C in N_2 flow are shown in **Figure 4-7**. As **Figure 4-7a** shows, the concentration of C_2H_4 in the gas outlet declined quickly with time increase for N_2 flow at the initial serval hours. The concentration of released C_2H_4 over Ag_{36}-A became less than 10 ppm and continued declining after release for 24 h, while the release of C_2H_4 continued and was quite stable over Ag_{36}-X and Ag_{62}-Y for longer time. The sustained release characteristic exhibited by Ag_{36}-X and Ag_{62}-Y was firstly due to the higher adsorption capacity of C_2H_4. The time courses of C_2H_4 release ratio shown in **Figure 4-7b** indicated different C_2H_4 release behavior between Ag_{36}-A, Ag_{36}-X and Ag_{62}-Y. A slightly faster release of C_2H_4 over Ag_{62}-Y was observed at the initial several hours than those over Ag_{36}-X and Ag_{36}-A, while Ag_{36}-A exhibited the slowest release characteristic. Given that the release measurement was conducted right after C_2H_4 adsorption on Ag^+-zeolites, the physically adsorbed C_2H_4 was also released during the evaluation. According to the adsorption isotherm results in Chapter 3, the amount of physically adsorbed C_2H_4 account for ca. 63, 56 and 50 % of those of overall amount for Ag_{36}-A, Ag_{36}-X and Ag_{62}-Y, respectively, at pressure of 1 bar. Thus, the drastic increase in C_2H_4 release ratio at the initial several hours was predominantly due to the release of physically adsorbed C_2H_4. Chemically adsorbed C_2H_4 may be released simultaneously, but it occupied only a small fraction of the total released amounts. After the physically adsorbed C_2H_4 was released (i.e., the C_2H_4 release ratio reached to 50~60 %), the release of chemically adsorbed C_2H_4 became predominant. A slightly faster release characteristic was observed for Ag_{62}-Y, which was due to the slightly weaker binding of C_2H_4, as suggested by C_2H_4-TPD result (desorption peak at 70 °C, which was at lower temperature than Ag_{36}-X and Ag_{36}-A in **Figure 4-6**). While the fraction of this chemically adsorbed C_2H_4 with weaker binding (TPD peak at 70 °C) was small for Ag_{62}-Y, the release of

chemically adsorbed C_2H_4 with stronger binding (TPD peak at 160 °C) became predominant then and accounted for the C_2H_4 release till fully released (from release time of ca. 12 h). The release of chemically adsorbed C_2H_4 with weaker binding for Ag_{36}-X and Ag_{36}-A continued for longer time (up to ca. 48 h) when comparing with Ag_{62}-Y due to the slightly stronger binding and larger fraction.

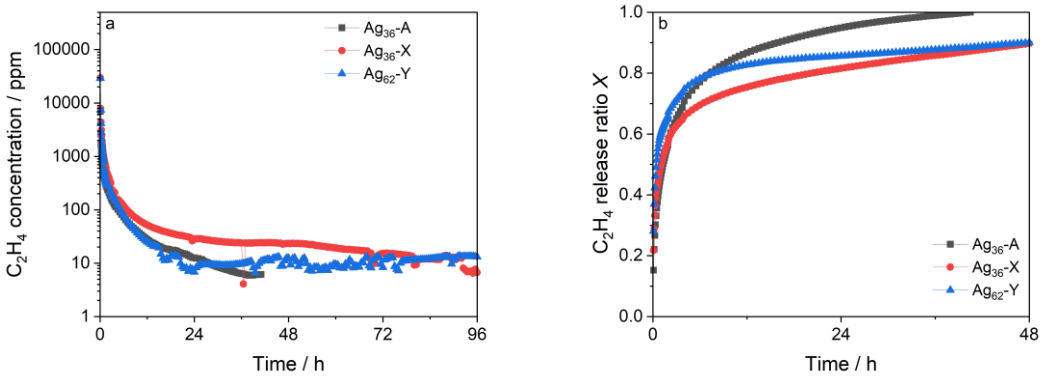

Figure 4-7. Time courses of (a) C_2H_4 concentration in the gas outlet and (b) C_2H_4 release ratio for Ag_{36}-A, Ag_{36}-X and Ag_{62}-Y. The dynamic release experiment was conducted at 25 °C under continuous flow of N_2 (10 mL min^{-1}).

Kinetic analysis was further performed for the results of the release experiments shown in **Figure 4-7**. Both a pseudo-first-order kinetic model and an Avrami equation were used for data fitting. As shown in **Figure 4-8**, the Avrami equation fitted much better to the experimental results than the pseudo-first-order kinetic model over the time. Thus hereafter, the Avrami equation was applied for further kinetic evaluation.

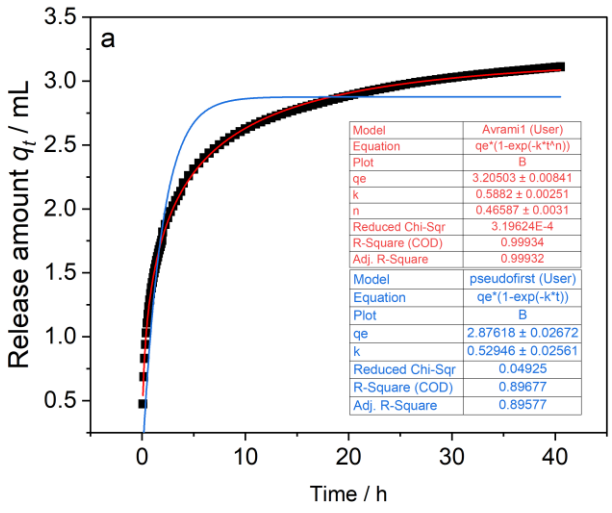

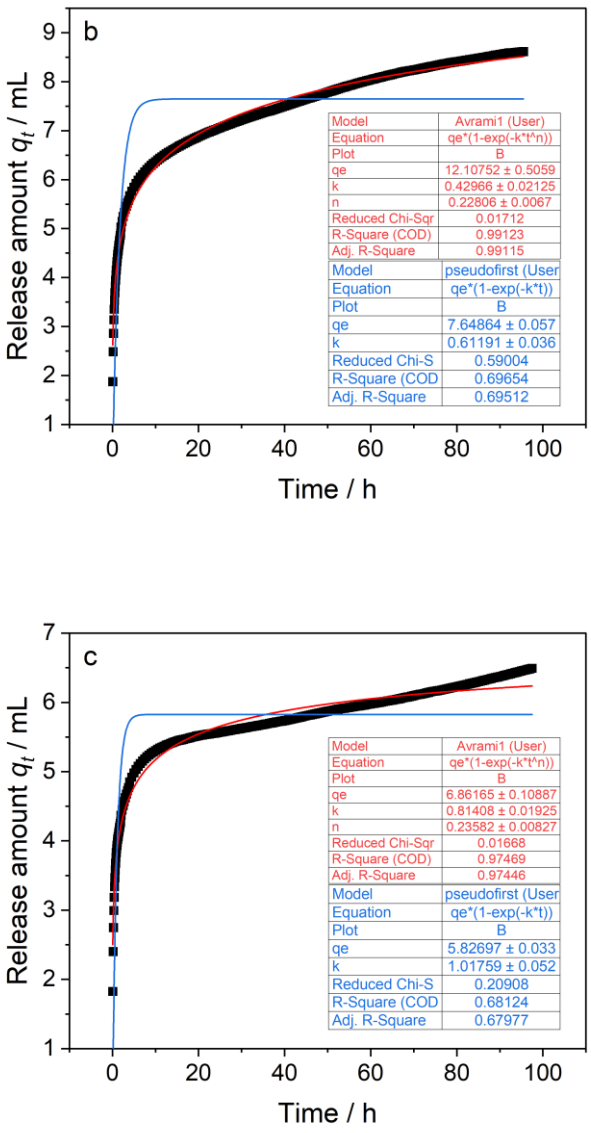

Figure 4-8. Experimental results and curve fitting for the C_2H_4 release over (a) Ag_{36}-A, (b) Ag_{36}-X and (c) Ag_{62}-Y. The dynamic release experiment was conducted under continuous flow of N_2 (10 mL min^{-1}). Avrami (red line) and Pseudo-first-order (blue line) kinetic model were used for curve fitting.

The overall release constant (k) as well as Avrami exponent (n) of the fitting results are summarized in **Table 4-1**. Ag_{36}-X exhibited the slowest release constant k of 0.430, implying its slow-release characteristic throughout the time. Ag_{36}-X exhibited a Avrami exponent (n) of 0.228, which was similar to that of Ag_{62}-Y, indicating the similar release mechanism, plausibly the chemical desorption process. While Ag_{36}-A exhibited a slightly larger Avrami exponent (n) of ca.

0.5, implying that other mechanism (possibly diffusion through the solid matrix) also contributed to controlling the release kinetics.[9,10] Although Ag_{36}-X had the same framework structure with Ag_{62}-Y, meaning that the diffusion of C_2H_4 from pores to the outer surface is similar, slower C_2H_4 release was observed for Ag_{36}-X than Ag_{62}-Y. The stronger interaction between C_2H_4 and Ag_{36}-X contributed to the slower C_2H_4 release over Ag_{36}-X.

Table 4-1. Release constant (*k*) and Avrami exponent (*n*) estimated from derivation of Avrami's kinetic model for C_2H_4 release from zeolites.

Sample	k (h^{-1})	n
Ag_{36}-A	0.588	0.466
Ag_{36}-X	0.430	0.228
Ag_{62}-Y	0.814	0.236
Ag_{36}-A_H_2O	0.785*	0.597*
Ag_{36}-X_H_2O	0.962*	0.590*
Ag_{62}-Y_H_2O	0.776*	0.506*
Na-A	0.819	0.633
Na-X	8.344	0.956
Na-Y	4.854	1.141

* Calculated based on the release data in the initial 2 h.

Given the presence of water vapor in the space for handling C_2H_4 release in the real application, the C_2H_4 release behavior of the Ag^+-zeolites in the presence of water vapor was further investigated. As shown in **Figure 4-9a**, when a relative humidity (RH) was near to 100 %, the Ag^+-zeolites released the adsorbed C_2H_4 very quickly, compared to that under dry conditions. This indicated that H_2O interacted more strongly with Ag^+-zeolites than C_2H_4. After the beginning of release measurement, the concentration of C_2H_4 in the gas outlet declined to a certain value and then became rather steady. Afterwards, it decreased dramatically and only a few of C_2H_4 was continuously released since then. This trend can be more clearly confirmed, as shown in **Figure 4-9b**, which were quite different with those shown in **Figure 4-7b** under dry conditions.

The release constant as well as Avrami exponent were also calculated and are shown in **Figure 4-10** and **Table 4-1**. Although Avrami equation had limitation in fitting the data over the time, it fitted well to the release in the initial 2 h. Increase of the rate constant was observed for Ag_{36}-A and Ag_{36}-X in the presence of water vapor, while water vapor had more prominent effect on C_2H_4 release over Ag_{36}-X, compared to that over Ag_{36}-A. Overall, Ag_{36}-A exhibited a slower release rate than Ag_{36}-X and Ag_{62}-Y did regardless of the presence or absence of water vapor. This slower release character for C_2H_4 over Ag_{36}-A was presumably due to the small pore size of the

framework of parent zeolite, limiting the diffusion of both C_2H_4 and water vapor. This speculation was suggested by the kinetic analyses for C_2H_4 desorption over Na^+-A, Na^+-X and Na^+-Y (**Table 4-1**), where Na-A exhibited much slower release.

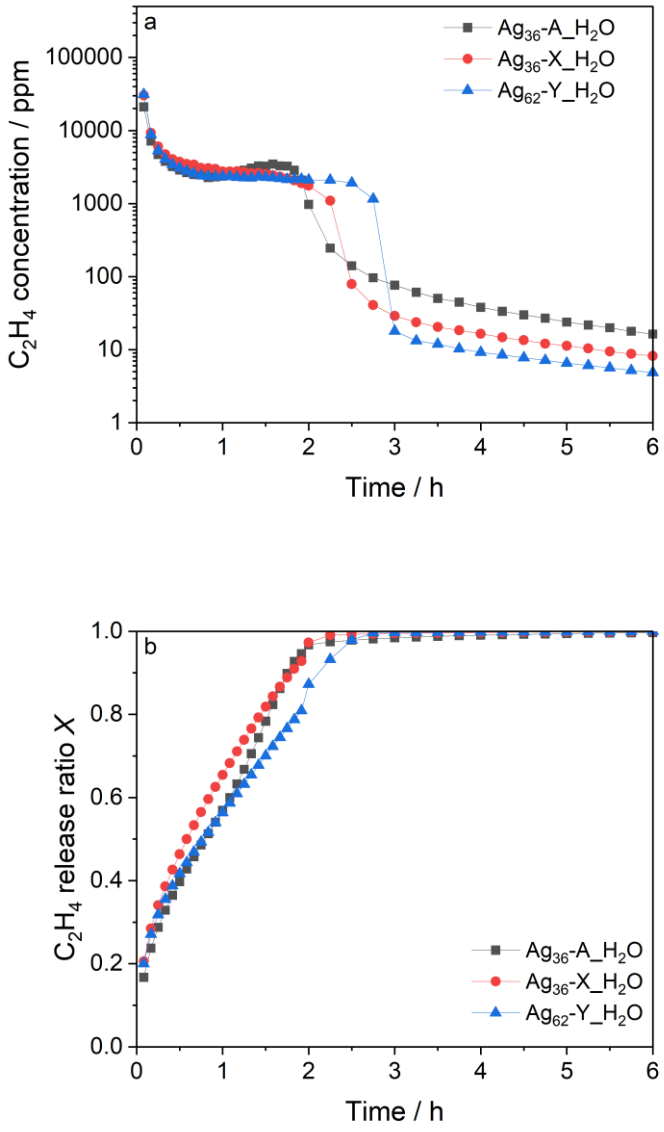

Figure 4-9. Time courses of (a) C_2H_4 concentration in the gas outlet and (b) C_2H_4 release ratio for Ag_{36}-A, Ag_{36}-X and Ag_{62}-Y. The dynamic release experiment was conducted under continuous flow of N_2 (10 mL min^{-1}) with water vapor.

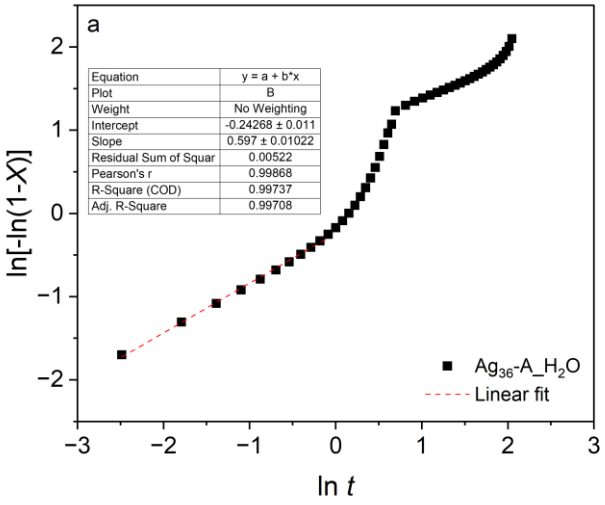
a
Equation | y = a + b*x
Plot | B
Weight | No Weighting
Intercept | -0.24268 ± 0.011
Slope | 0.597 ± 0.01022
Residual Sum of Squar | 0.00522
Pearson's r | 0.99868
R-Square (COD) | 0.99737
Adj. R-Square | 0.99708
ln[-ln(1-X)]
ln t
Ag36-A_H2O
Linear fit

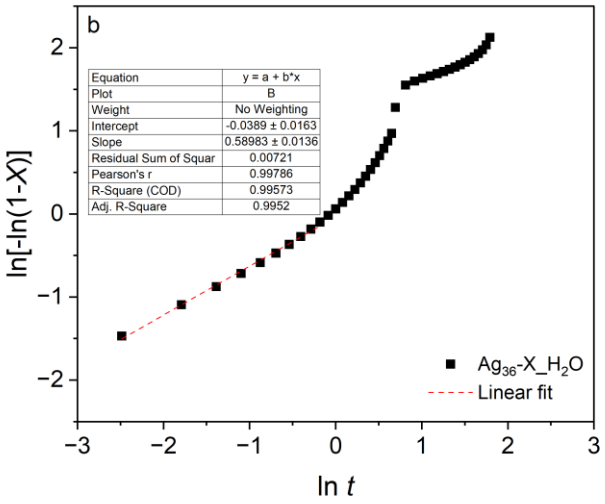
b
Equation | y = a + b*x
Plot | B
Weight | No Weighting
Intercept | -0.0389 ± 0.0163
Slope | 0.58983 ± 0.0136
Residual Sum of Squar | 0.00721
Pearson's r | 0.99786
R-Square (COD) | 0.99573
Adj. R-Square | 0.9952
ln[-ln(1-X)]
ln t
Ag36-X_H2O
Linear fit

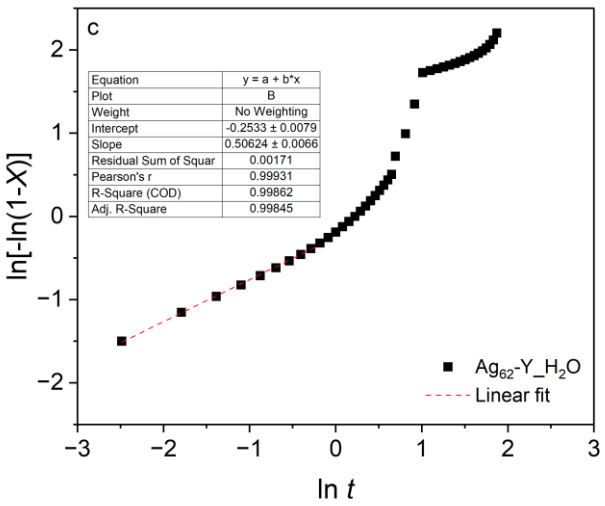

Figure 4-11. ln[-ln(1-*X*)] plotted versus ln *t* for C_2H_4 release with water vapor over (a) Ag_{36}-A, (b) Ag_{36}-X and (c) Ag_{62}-Y according to the derivation from Avrami's kinetic model. Linear fitting was conducted in the range of ln *t* from -2.5 to 0.69.

3.3 C_2H_4 release and effect on potato sprouting

The conditions for the practical application of Ag^+-zeolites as C_2H_4 release materials may differ from those applied in thermal desorption measurement or dynamic evaluation described above. Here, Ag^+-zeolites with pre-adsorbed C_2H_4 were placed with potatoes in a film package and stored in a dark room at a constant temperature. It was observed that the C_2H_4 concentration in the package decreased quickly and no more C_2H_4 was detected after 4 days. This was attributed the presence of water by the respiration of potatoes boosted the release of C_2H_4 from Ag^+-zeolites. This short release time was not enough to confirm the effect of C_2H_4 on sprouting and no sprouting was observed for the potatoes with or without the presence of exogeneous C_2H_4 in this case. To extend the release duration of C_2H_4, $CaCl_2$ was added to capture the water molecules. The time courses of the concentration of C_2H_4 in the film packages are shown in **Figure 4-12**. No significant amount of C_2H_4 was detected in the film package with only potatoes and no exogenous C_2H_4 addition (square data). The C_2H_4 concentration decreased quickly and no more C_2H_4 higher than the detection limit was detected after 4 days in the film package with gaseous C_2H_4 addition, which was due to the diffusion of C_2H_4 molecules through the film package. Surprisingly, the release of C_2H_4 over Ag_{36}-X lasted for near 30 days under the storage conditions.

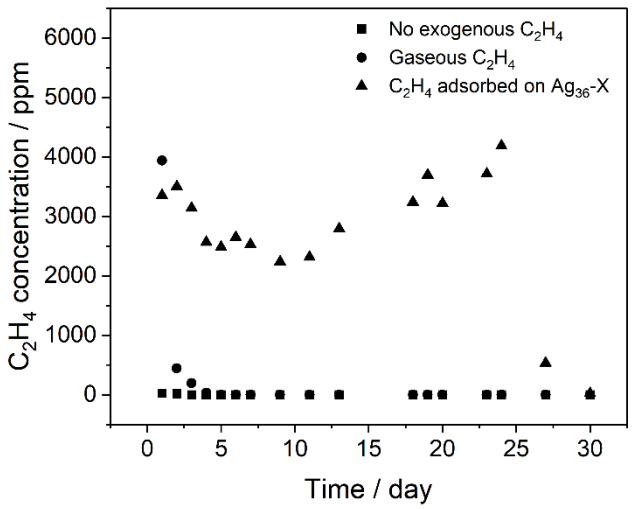

Figure 4-12. Time courses of C_2H_4 concentration in film packages with or without exogenous C_2H_4 addition.

The sprouting of potatoes was also recorded and some of the photographs are shown in **Figure 4-13**. **Figures 4-13 a, b** and **c** show the sprouting conditions of potatoes before the experiment. Only very small buds were observed, plausibly due to the long-time storage before the experiment. After two weeks, more pronounced sprouting occurred in potatoes packed without exogenous C_2H_4 addition or with gaseous C_2H_4 addition. In contrast, sprouting was inhibited in potatoes placed with Ag_{36}-X pre-adsorbed with C_2H_4. These results demonstrated the sustained release behavior of C_2H_4 over Ag_{36}-X and the potential application of Ag_{36}-X as C_2H_4 release material.

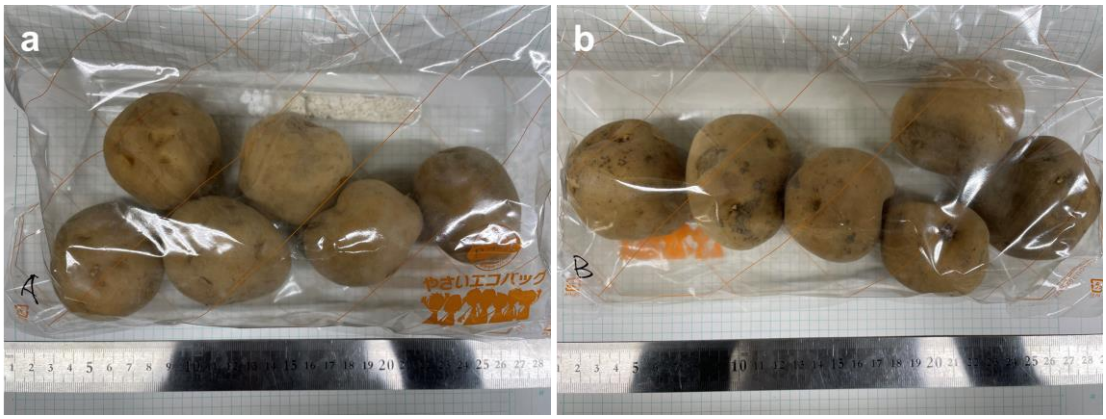

Figure 4-13. Potato sprouting recorded at the 1st day for (a) with C_2H_4 adsorbed on Ag_{36}-X, (b) gaseous C_2H_4 addition and (c) no exogenous C_2H_4 addition; recorded at two weeks later for (d) with C_2H_4 adsorbed on Ag_{36}-X, (e) gaseous C_2H_4 addition and (f) no exogenous C_2H_4 addition.

4. Conclusions

In this chapter, the release behavior of C_2H_4 from various Ag^+-exchanged zeolites was systematically investigated. The C_2H_4-TPD confirmed that C_2H_4 can be released at low temperature near room temperature from the Ag^+-exchanged zeolites, making them advantageous as release materials. In addition, TPD results revealed the presence of C_2H_4 adsorption sites with varying strengths within these materials. Further analysis using a pseudo-first-order kinetic model and Avrami equation on the dynamic release measurement demonstrated that the Avrami equation provided a superior fit to the experimental data compared to the pseudo-first-order model. The fitting results demonstrated that Ag_{36}-A, Ag_{36}-X, and Ag_{62}-Y exhibited distinct release characteristics, with Ag_{36}-X showing the slowest release characteristic throughout the time. Notably, despite possessing the same framework structure, Ag_{36}-X exhibited slower C_2H_4 release compared to Ag_{62}-Y, which was due to the stronger binding strength of C_2H_4 on Ag_{36}-X. The presence of water vapor had significant impact on the C_2H_4 release behavior from Ag^+-zeolites, particularly for Ag_{36}-X. Slower release rate was observed for Ag_{36}-A compared to Ag_{36}-X and Ag_{62}-Y in the presence of water vapor. The pore size had great impact on diffusion kinetics. Overall, given that Ag_{36}-X exhibited a high C_2H_4 adsorption capacity (discussed in Chapter 3) and a comparably slow-release characteristic, it is promising as a C_2H_4 controlled-release material. The potato sprouting experiment further validated the potential application of Ag_{36}-X as a C_2H_4 release material.

5. References

(1) Saltveit, M. E. Effect of Ethylene on Quality of Fresh Fruits and Vegetables. *Postharvest Biol. Technol.* **1999**, *15* (3), 279–292. https://doi.org/10.1016/S0925-5214(98)00091-X.

(2) Barry, C. S.; Giovannoni, J. J. Ethylene and Fruit Ripening. *J. Plant Growth Regul*. **2007**, *26* (2), 143–159. https://doi.org/10.1007/s00344-007-9002-y.

(3) Armitage, A. M. Promotion of Fruit Ripening of Ornamental Peppers by Ethephon. *HortScience* **1989**, *24* (6), 962-964. https://doi.org/10.21273/HORTSCI.24.6.962.

(4) El-Kereamy, A.; Chervin, C.; Roustan, J. P.; Cheynier, V.; Souquet, J. M.; Moutounet, M.; Raynal, J.; Ford, C.; Latché, A.; Pech, J. C.; Bouzayen, M. Exogenous Ethylene Stimulates the Long-Term Expression of Genes Related to Anthocyanin Biosynthesis in Grape Berries. *Physiol. Plant.* **2003**, *119* (2), 175–182. https://doi.org/10.1034/j.1399-3054.2003.00165.x.

(5) Avrami, M. Kinetics of Phase Change. I: General Theory. *J. Chem. Phys.* **1939**, *7* (12), 1103–1112. https://doi.org/10.1063/1.1750380.

(6) Kinefuchi, I.; Yamaguchi, H.; Sakiyama, Y.; Takagi, S.; Matsumoto, Y. Inhomogeneous Decomposition of Ultrathin Oxide Films on Si(100): Application of Avrami Kinetics to Thermal Desorption Spectra. *J. Chem. Phys.* **2008**, *128* (16). https://doi.org/10.1063/1.2905209.

(7) Serna-Guerrero, R.; Belmabkhout, Y.; Sayari, A. Modeling CO_2 Adsorption on Amine-Functionalized Mesoporous Silica: 1. A Semi-Empirical Equilibrium Model. *Chem. Eng. J.* **2010**, *161* (1–2), 173–181. https://doi.org/10.1016/j.cej.2010.04.024.

(8) Serna-Guerrero, R.; Sayari, A. Modeling Adsorption of CO_2 on Amine-Functionalized Mesoporous Silica. 2: Kinetics and Breakthrough Curves. *Chem. Eng. J.* **2010**, *161* (1–2), 182–190. https://doi.org/10.1016/j.cej.2010.04.042.

(9) Liu, Q.; Shi, J.; Zheng, S.; Tao, M.; He, Y.; Shi, Y. Kinetics Studies of CO_2 Adsorption/Desorption on Amine-Functionalized Multiwalled Carbon Nanotubes. *Ind. Eng. Chem. Res.* **2014**, *53* (29), 11677–11683. https://doi.org/10.1021/ie502009n.

(10) Teng, Y.; Liu, Z.; Xu, G.; Zhang, K. Desorption Kinetics and Mechanisms of CO_2 on Amine-Based Mesoporous Silica Materials. *Energies (Basel)* **2017**, *10* (1). https://doi.org/10.3390/en10010115.

(11) Ho, B. T.; Bhandari, B. R. Novel Solid Encapsulation of Ethylene Gas Using Amorphous α-Cyclodextrin and the Release Characteristics. *J. Agric. Food Chem.* **2016**, *64* (17), 3318–3323. https://doi.org/10.1021/acs.jafc.5b06037.

(12) Shi, L.; Fu, X.; Tan, C. P.; Huang, Q.; Zhang, B. Encapsulation of Ethylene Gas into Granular Cold-Water-Soluble Starch: Structure and Release Kinetics. *J. Agric. Food Chem.* **2017**, *65* (10), 2189–2197. https://doi.org/10.1021/acs.jafc.6b05749.

(13) Bazzano, M.; Barolo, C.; Buscaino, R.; D'Agostino, G.; Ferri, A.; Sangermano, M.; Pisano, R. Controlled Atmosphere in Food Packaging Using Ethylene-α-Cyclodextrin Inclusion Complexes

Dispersed in Photocured Acrylic Films. *Ind. Eng. Chem. Res.* **2016**, *55* (3), 579–585. https://doi.org/10.1021/acs.iecr.5b03980.

(14) Liu, Z.; Wang, S.; Tan, C. P.; Zhang, B.; Fu, X.; Huang, Q. Effect of Lipids Complexes on Controlling Ethylene Gas Release from V-Type Starch. *Carbohydr. Polym.* **2022**, *291*. https://doi.org/10.1016/j.carbpol.2022.119556.

(15) Al Jarallah, A. M.; Anabtawi, J. A.; Siddiqui, M. A. B.; Aittani, A. M.; Al Sa'doun, A. W. Ethylene Dimerization and Oligomerization to Butene-1 and α-olefins: A Review of Catalytic Systems and Processes. *Catal. Today* **1992**, *14* (1), 1-121. https://doi.org/10.1016/0920-5861(92)80128-A

(16) Spoto, G.; Bordiga, S.; Ricchiardi, G.; Scarano, D.; Zecchina, A.; Borello, E. IR Study of Ethene and Propene Oligomerization on H-ZSM-5: Hydrogen-Bonded Precursor Formation, Initiation and Propagation Mechanisms and Structure of the Entrapped Oligomers. *J. Chem. Soc. Faraday Trans.* **1994**, *90* (18), 2827-2835. https://doi.org/10.1039/FT9949002827

Chapter 5

Summary, General Conclusions and Prospect

In this thesis, the present author anticipated that the pore walls of crystalline porous materials are of great importance in the application of porous materials. Effective utilization of the functional groups on pore walls can lead to enhanced performance in catalysis and sorption. Given this, two kinds of microporous materials that possess pore walls with regular structures, MOF and zeolite, were applied as solid matrixes to introduce active metal species.

In Chapter 2, NH_2-MIL-53 was applied as a support for introducing Pd particles and the catalytic performance of the resulting catalysts were evaluated with NO_2^- reduction in water. The amino functional group in NH_2-MIL-53 played a critical role in introducing Pd. The combination of using NH_2-MIL-53 and the equilibrium adsorption method facilitated uniform dispersion of Pd nanoparticles with high Pd loadings. Pd(111) facets on Pd@NH_2-MIL-53 exhibited high activity for NO_2^- reduction in water. Moreover, the high electron density owing to the electron donation from the amino functional group promoted NO_2^- reduction in water.

In Chapter 3, Ag^+-exchanged zeolites were prepared by a conventional ion-exchange process using zeolites with different topology framework structures. C_2H_4 adsorption characteristics over Ag^+-exchanged zeolites were systematically investigated. Ag^+-exchanged zeolites exhibited stronger interactions with C_2H_4 than Na^+-zeolites, where chemical adsorption occurred over Ag^+-exchanged zeolites. The framework structure as well as the Si/Al ratio of the zeolites played critical role in affecting the nature of Ag species, and further on the adsorption amount and strength of C_2H_4. The large Ag clusters or metallic Ag^0 nanoparticle species presented in zeolite with low Si/Al ratio did not act as bind site for C_2H_4. C_2H_4 adsorption on Ag_{36}-X was stronger than Ag_{62}-Y despite they had same framework topology, which was presumably due to the Ag species located in different sites, thus different natures of Ag species were presented.

In Chapter 4, the release behavior of C_2H_4 from various Ag^+-exchanged zeolites was systematically investigated. Despite possessing the same framework topology, kinetic analysis revealed that Ag_{36}-X exhibited slower C_2H_4 release compared to Ag_{62}-Y, which was attributed to the stronger adsorption of C_2H_4 over Ag_{36}-X. The pore size of zeolite also had great impact on release performance, as slower release rate was observed for Ag_{36}-A. The potato sprouting experiment demonstrated that Ag_{36}-X is a good candidate for application as C_2H_4 release material.

From these results, the present author demonstrated that the functional groups on the pore walls of microporous MOF and zeolite were critical for tuning the nature of introduced active metal species, which further altered the catalysis and adsorption as well as desorption performance. The methodology is quite general but effective and can be appliable for different kinds of porous materials. Porous materials (especially with small pores to introduce the size confinement effect) are desirable when the introduced active metal species are encapsulated, as a large fraction of the surface of active metal species can be intact with the functional groups on pore walls. However, the porosity might not be necessary if the formation of a large number of

regularly aligned functional groups and the introduction of active metal species with small sizes can be realized. Enhanced performance can also be expected with the effective utilization of these functional groups on these materials even without porosity.